



HAL
open science

Effects of continuous and intermittent hypergravity on skeleton

Vasily Gnyubkin

► **To cite this version:**

Vasily Gnyubkin. Effects of continuous and intermittent hypergravity on skeleton. Tissues and Organs [q-bio.TO]. Université Jean Monnet - Saint-Etienne, 2015. English. NNT: 2015STET002T . tel-01539024

HAL Id: tel-01539024

<https://theses.hal.science/tel-01539024v1>

Submitted on 14 Jun 2017

HAL is a multi-disciplinary open access archive for the deposit and dissemination of scientific research documents, whether they are published or not. The documents may come from teaching and research institutions in France or abroad, or from public or private research centers.

L'archive ouverte pluridisciplinaire **HAL**, est destinée au dépôt et à la diffusion de documents scientifiques de niveau recherche, publiés ou non, émanant des établissements d'enseignement et de recherche français ou étrangers, des laboratoires publics ou privés.

THESE DE DOCTORAT

Université Jean Monnet

Spécialité: BIOLOGIE

Présentée par Vasily GNYUBKIN

Devant l'Université Jean Monnet, Saint-Etienne

En vue de l'obtention du diplôme de DOCTORAT

***Effects of Continuous and Intermittent
Hypergravity on Skeleton***

Soutenue publiquement le 22 Septembre 2015

Composition du Jury:

Rapporteur : Jean Pol Fripiat (Vandoeuvre-lès-Nancy)

Rapporteur : Georges Boivin (Lyon)

Examineur : Carole Bougault (Lyon)

Examineur : Alain Guignandon (St-Etienne)

Directrice de thèse : Laurence Vico (St-Etienne)

Présidente : Valérie Geoffroy (Paris)

Content

List of abbreviations	6
1. INTRODUCTION	7
1.1 Bone physiology	7
1.1.1 Bone turnover.....	7
1.1.2 Remodeling control by osteocytes, mechanotransduction.....	10
1.2 Bone adaptation to altered gravity: space flights and countermeasures	16
1.2.1 Microgravity	16
1.2.2 Countermeasures on ISS	17
1.2.3 Artificial gravity.....	18
1.2.4 Whole body vibration	19
2. Objectives of the current research project	22
2.1 Biological objectives.....	23
2.2 Technical objectives.....	23
3. Results.....	24
3.1 Skeleton adaptation to chronic hypergravity	24
3.1.1 Introduction to the paper	24
3.1.2 Paper #1: “Effects of chronic hypergravity: from adaptive to deleterious responses in growing mouse skeleton”	24
Abstract.....	25
Introduction.....	26
Materials and Methods.....	28
Results.....	33
Discussion	39
Conclusion	43
Acknowledgments.....	43
Grants.....	43
Author contributions	44
References.....	44
Supporting information	49
Conclusion/perspectives	50
3.2 Skeleton adaptation to intermittent hypergravity.....	51
3.2.1 Introduction to the paper	51

3.2.2 Paper #2: “High-acceleration Whole Body Vibration stimulates cortical bone accrual and increases bone mineral content in growing mice”	51
Abstract	52
Introduction.....	52
Materials and Methods.....	54
Results.....	60
Discussion	66
Acknowledgments.....	68
Ethical approval	68
Conflict of Interest	68
References.....	68
Not published data (0.5g, 0.5-2g)	73
3.3 Immunohistochemical detection of osteocyte proteins.....	76
3.3.1 Paper #3: “Osteocyte protein expression in mouse and human biopsies: optimized methods for detection and quantification”	84
Abstract	85
Introduction.....	85
Materials and Methods.....	87
Results.....	98
Discussion	102
Conclusion	104
References.....	104
Supplementary materials.....	107
Detailed protocol of immunohistochemistry	108
Mouse bones	108
Autofluorescence: a useful feature for lacunae-canalicular morphology assessment?.....	119
3D assessment of osteocyte proteins.....	123
4. Conclusion and perspectives.....	126
5. References.....	128
6. Annexes.....	135
Technical data	135
Fluorescent immunohistochemistry protocol for double staining: 3 days sequential protocol	135
Immunohistochemistry protocol for the enzymatic detection	135

Immunohistochemistry protocol for the enzymatic detection: double staining, 3 days sequential protocol	136
Protocol of 3D immunohistochemistry adapted from Clarity technique	137
Supplementary videos	139
Papers published/submitted	140
Author's CV	140
Book chapter "Animals: Unloading, casting"	143

List of figures

Figure 1. Remodeling compartment in human iliac crest biopsy..	9
Figure 2. Possible coupling mechanisms between bone resorption and formation..	10
Figure 3. Osteocyte biological environment.	11

Figure 4. Lacunar-canalicular system. around a Haversian canal.	11
Figure 5. Osteocyte regulation of bone remodeling.....	12
Figure 6. Different scales of mechanical loading perception and reaction on it.....	13
Figure 7. Triggering of the Wnt/ β -catenin pathway in osteocytes in response to load.	14
Figure 8. Role of Sclerostin in pathological conditions.....	15
Figure 9. Bone mineral density (BMD) and body composition.....	18
Figure 10. Non-linear relationship between mechanical loading magnitude, number of loading events and bone adaptation..	20
Figure 11. Effects of whole body vibration at different accelerations on cortical bone mass-structural parameters.....	73
Figure 12. Effects of whole body vibration at different accelerations on trabecular bone structural parameters.	74
Figure 13. Effects of whole body vibration at different accelerations on trabecular bone structural parameters.....	75
Figure 14. Immunohistochemistry with enzymatic detection of osteocyte proteins in mouse femoral bones.....	77
Figure 15. Sclerostin labeling. Fluorescent immunohistochemistry on paraffin embedded mouse femoral cortex.....	78
Figure 16. Fluorescent immunohistochemistry, paraffin embedded mouse femoral cortex....	79
Figure 17. Fluorescent immunohistochemistry, paraffin embedded mouse femoral cortex....	79
Figure 18. Fluorescent immunohistochemistry, paraffin embedded mouse femoral cortex....	80
Figure 19. Fluorescent immunohistochemistry, paraffin embedded mouse femoral cortex....	82
Figure 20. Fluorescent immunohistochemistry on methyl methacrylate embedded human iliac crest biopsy.	82
Figure 21. Fluorescent immunohistochemistry on methyl methacrylate embedded human iliac crest biopsy.	83
Figure 22. Fluorescent immunohistochemistry on methyl methacrylate embedded human iliac crest biopsy.	84
Figure 23. Confocal imaging of autofluorescence of lacunar-canalicular network from a paraffin embedded mouse femoral cortex.....	120
Figure 24. Confocal imaging of autofluorescence of lacunar-canalicular network from a paraffin embedded mouse femoral cortex.....	121
Figure 25. Confocal imaging of autofluorescence of lacunar-canalicular network and a vessel with two erythrocytes inside	122
Figure 26. Confocal imaging of autofluorescence of lacunar-canalicular network and two vessels	123
Figure 27. Confocal imaging of DMP1 and autofluorescence	124
Figure 28. Fluorescent immunohistochemistry of Sclerostin on 10 μ m thick section of mouse femoral cortex.	125

List of abbreviations

BRC – bone remodeling compartment

LCN – lacunar-canalicular network

DMP1 - Dentin matrix acidic phosphoprotein 1

WBV – whole body vibration

IHC – immunohistochemistry

μ CT – micro computed tomography

Ct.Th – cortical thickness

Ct.Ar – cortical area

Tb.Th – trabecular thickness

Tb.N – trabecular number

BV/TV – bone volume

Conn.D – connectivity density

MAR – mineral apposition rate

dLS/BS – double labeled surface over bone surface

BFR/BS – bone formation rate over bone surface

Oc.S/BS – osteoclast surface over bone surface

OS/BS – osteoid surface over bone surface

ROI – region of interest

1. INTRODUCTION

Bone is a mineralized connective tissue that together with cartilage forms the skeleton. It aims to play three important roles in the body: 1) providing the rigid structure that is needed for locomotion; 2) protecting vital organs; 3) maintaining serum homeostasis of ions, in particular calcium and phosphate. In order to timely respond to changing skeletal loading conditions, maintain a stable level of ions in blood, and provide bone integrity, there are three basic cell types – the osteoblast, osteoclast and osteocyte, which operate within a complex regulatory network.

The skeleton has a remarkable ability to adapt to external mechanical forces. Numerous skeletal properties can be modulated, including metabolism, bone mass, structure, and consequently strength. Such adaptation responses require changes in patterns of bone cellular activities, and skeletal strength generally is regulated by a dynamic balance between bone formation and resorption. For the field of bone biology now a current challenge is to understand the contribution of the wide variety of mechanical loading regimens to bone adaptation and identify the most beneficial one.

After a brief recall of basic bone physiology, we will focus on the known effects of altered gravity on skeleton, encountered during spaceflight (microgravity), centrifuged habitat (chronic hypergravity) or whole body vibration (intermittent hypergravity).

1.1 Bone physiology

1.1.1 Bone turnover

Bone is a metabolically highly active organ whose structure and architecture undergo lifelong reorganization with the processes of modeling, and remodeling. Modeling is a new bone construction on one site and a break down on a different site. Thus bone's shape and size are changing, whereas remodeling occurs at the same site. Both ensure skeleton architecture adaptation to mechanical loading and serve as a part of calcium homeostasis system [1]. Over recent years number of cellular contributors responsible for remodeling has expanded and now includes osteoblasts, osteoclasts, T-cells, macrophages, osteoclasts and osteoblasts precursors, and osteocytes [2–4].

Osteoblasts and osteoclasts still are two major players, providing removal and replacement of old or damaged bone by new tissue. Osteoblasts share the origin with adipocytes, chondrocytes, and endothelial cells. The fate of stem cells is determined by intracellular proteins called transcription factors. Several of them proved to be important. The most crucial transcription factors for osteoblast differentiation and late mineralization are core-binding factor Runx2, Dlx5 (Runx-2 activator) and Osterix, acting via Wnt10b signaling via frizzled and lipoprotein receptor-related protein 5 (LRP-5). Osteoblasts are forming a one-cell layer covering all bone surfaces. They synthesize an extracellular matrix (consisting of type I collagen fibers and other proteins), and subsequently mineralize this matrix into bone [5–7].

Osteoclasts originate from hematopoietic stem cells of the myeloid lineage. Osteoblasts or stromal cells in bone marrow produce the cytokine macrophage colony-stimulating factor (M-CSF), which enhances proliferation and survival of progenitors, and upregulates the receptor activator of nuclear factor kappa B (RANK). RANK regulates osteoclasts proliferation, differentiation and fusion via activation of several transcription factors such as NFkB and AP-1. RANK is activated by RANK ligand (RANKL), a key osteoclastogenic cytokine produced by osteoblasts, bone marrow stromal cells, and osteocytes [8]. In turn, RANKL is inhibited by osteoprotegerin (OPG) which is a decoy receptor with large homologies to RANK [6].

To maintain bone mass, the bone formed within bone remodeling compartments (BRC) must replace the amount of bone resorbed within that BRC. The BRC are shaped by a cellular canopy separating the bone remodeling events on the bone surface from the bone marrow [9,10]. Such stimulation of osteoblast activity in response to resorption is called coupling and complexity of its regulation is thoroughly described in the recent review of Sims et al [11]. Resorption and formation cells do not appear on the bone surface at the same time and a BRC could exist at the same location for months in humans [12] and days in rodents [13] (Fig.1). Importantly, between phases of resorption and formation there is a reversal phase

[13,14], which means that mediators of coupling must overcome this time delay [11].

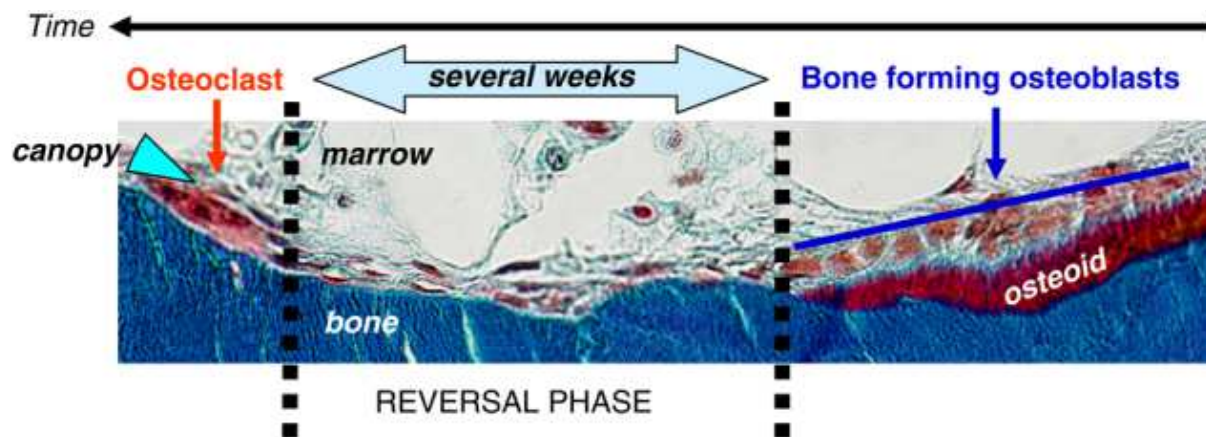


Figure 1 Remodeling compartment in human iliac crest biopsy. A period of several weeks (reversal phase) separates osteoclasts from osteoblasts. The canopy of elongated cells covers the bone-remodeling site. From [14].

The main classes of coupling factors are the following: matrix-derived factors, osteoclasts-secreted factors, and osteoclast membrane-bound factors. The main influence of these factors is to stimulate differentiated osteoblasts, osteoblasts progenitors recruitment, migration, and differentiation [11]. It has been hypothesized that another target for coupling factors is reversal cells, which cover 80% of eroded surface [14] and may provide a connection between osteoclasts and osteoblasts precursors on a bone surface [11,15] (Fig. 2). The remodeling canopy formed by bone-lining cells might provide a space for controlled factors exchange between contributing cells, and keep local concentration of coupling factors during the reversal phase high enough to stimulate bone formation [11]. Also, mesenchymal cells that form an envelope surrounding the red bone marrow and appear as canopy covering nearly all the osteoclasts in human trabecular bone [14], is another target for coupling factors (Fig. 1 and 2).

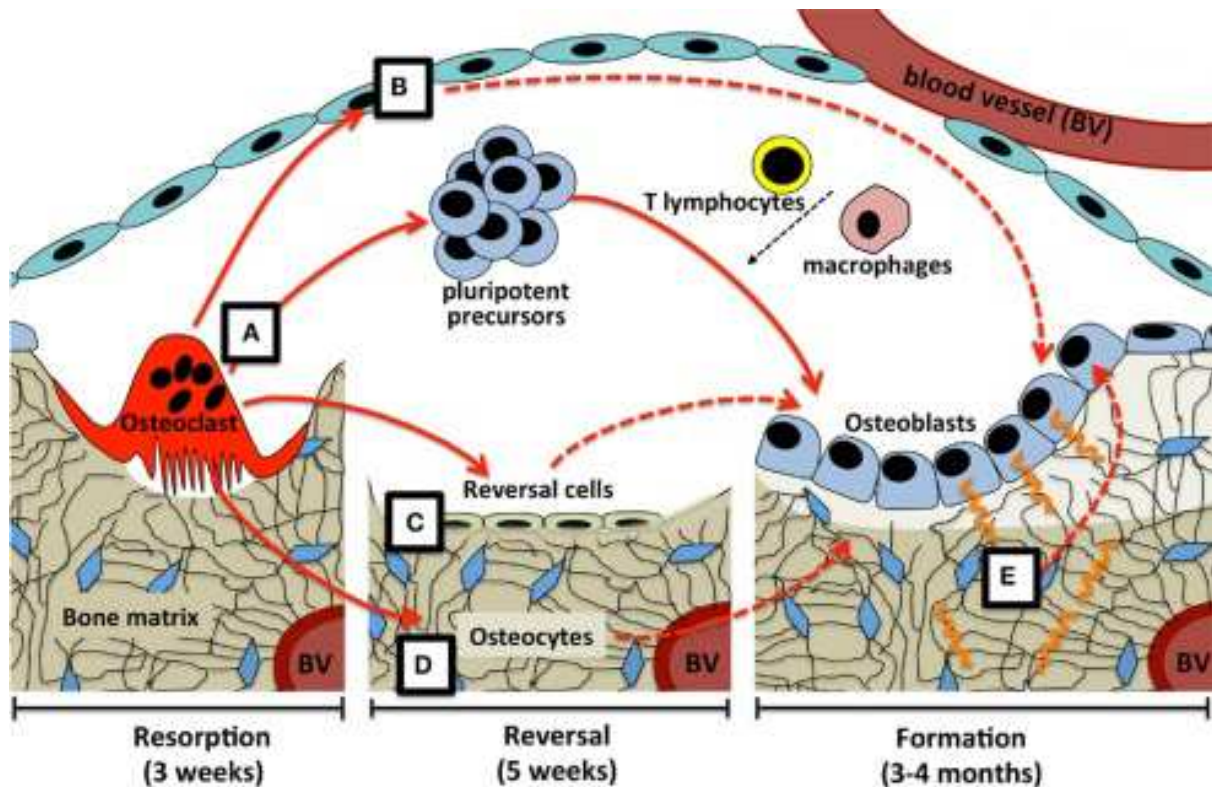


Figure 2. Possible coupling mechanisms between bone resorption and formation. (A) Osteoclast-derived factors, which may act directly on cells that would transmit further signals (dashed lines): (B) osteoblast-lineage cells in the remodeling canopy, (C) reversal cells, and (D) osteocytes. Additionally, (E) physical changes, including the resorptive pit itself, and mechanical strain detected by the osteocyte network might provide signals for correct matrix production. Periods of time are based on adult human iliac crest biopsies. From [9].

1.1.2 Remodeling control by osteocytes, mechanotransduction

While most of the bone turnover occurs on the surface, where it interfaces with bone marrow (endosteal surface), calcified bone matrix is not inert as an extensive network of interconnected osteocytes lies within it. Osteocytes are the most abundant bone cells (20000 – 30000 cells per mm^3 [16]), they originate from osteoblasts when some become buried in their own matrix, and then undergo a dramatic transformation from polygonal cells to cells extending dendrites towards bone surface, vessels, and other osteocytes (Fig. 3) [17]. Osteocytes and their dendrite-like processes contained within fluid-filled micro-canals form lacunar-canalicular network (LCN), which penetrates the entire skeleton (Fig. 4) [5]. On average, each osteocyte has 89 dendritic processes and in human body osteocytes form about 23 trillion connections with total dendritic processes length of 175 km [16]. The total LCN area is 215 m^2 , which is almost twice bigger than lungs surface (118 m^2) [16].

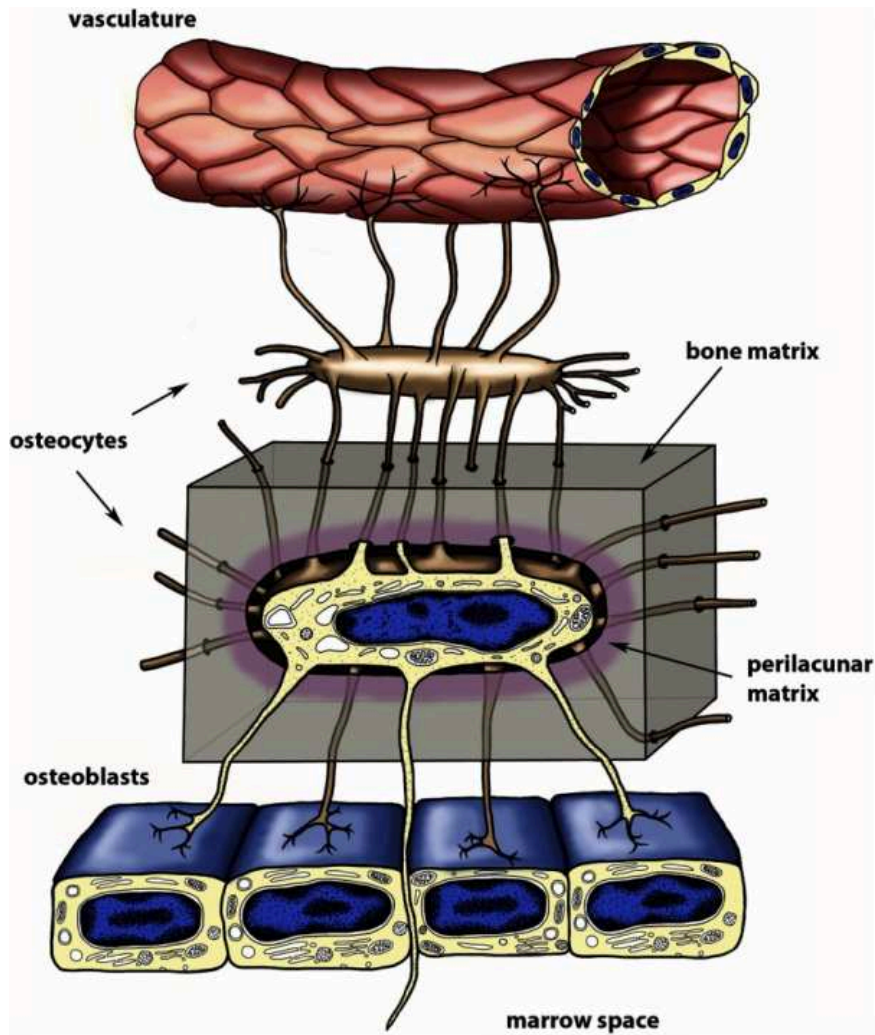


Figure 3 Osteocyte biological environment. From [18]

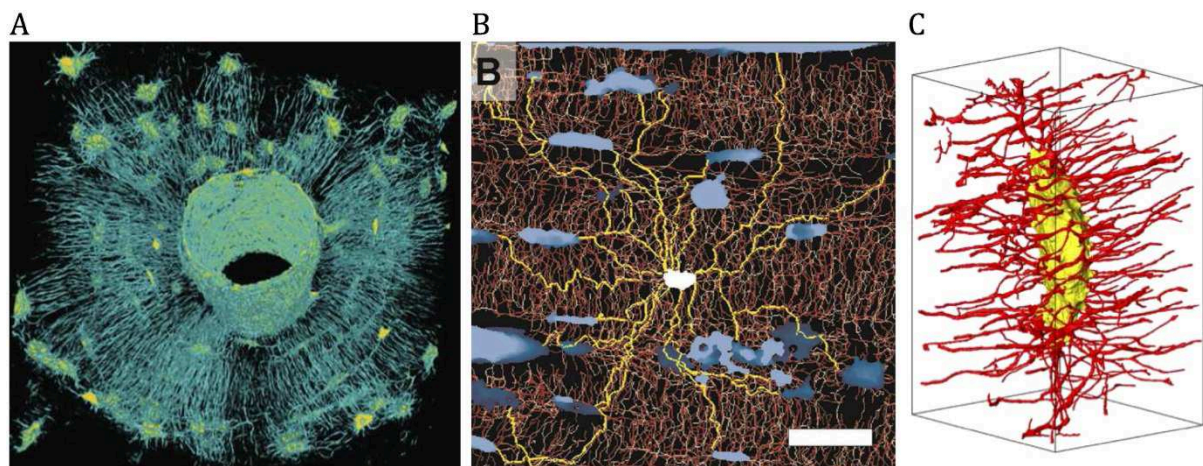


Figure 4. Lacunar-canalicular system. A: lacunar-canalicular network around a Haversian canal. B: Direct canalicular paths between a single osteocyte (white) and nearby osteocytes (blue) or the vascular pore (top) C: An osteocyte lacuna (yellow) with 86 emanating canaliculi (red). From [16].

Osteocytes via their massive network are able to orchestrate bone's exclusively controlled regulatory system [5,6]. This cellular network is understood to release and receive signals that control the processes of bone matrix production via Sclerostin [19] and Dickkopf (Dkk) proteins, particularly Dkk-1 and Dkk-2 [20,21], mineralization via Dentin Matrix Phosphoprotein 1 (DMP1) [22], and resorption via RANKL [8,23,24]. A scheme of bone remodeling under osteocytes' control is presented on Fig. 5.

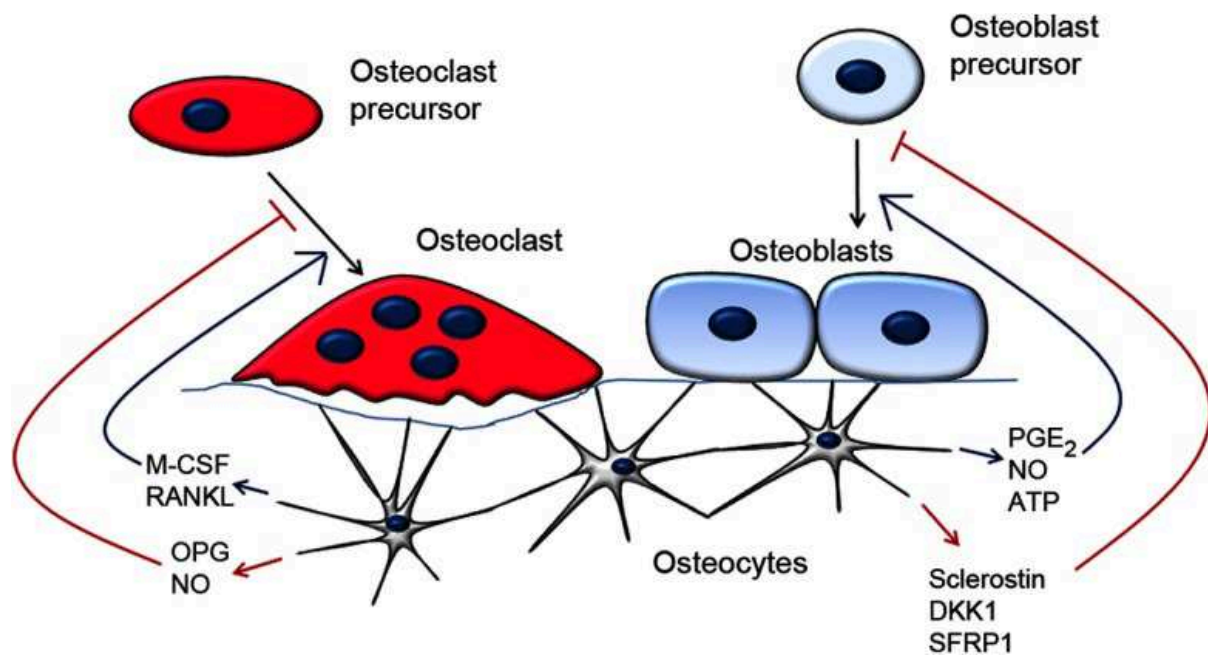


Figure 5. Osteocyte regulation of bone remodeling. Osteocytes express RANKL and macrophage-colony stimulating factor (M-CSF) to promote, and OPG and NO to inhibit, osteoclast formation and activity. PGE₂, NO, and ATP act to activate Wnt signaling. Sclerostin, DKK1, and SFRP1 inhibit Wnt signaling. From [18].

Bone is a unique tissue in relation to its abilities to adaptively remodel itself in response to mechanical loading applied [25]. Because of the distribution of osteocytes throughout the bone matrix and their complex network, it was hypothesized that osteocytes are responsible for sensing mechanical loading. By targeted deletion of osteocytes in mice expressing the diphtheria toxin receptor specifically in osteocytes, it was demonstrated that these mice were resistant to unloading-induced bone loss [26].

There are several possible stimuli that could be detected by an osteocyte: physical deformation of the bone matrix, direct cellular deformation, or the load-induced flow of canalicular fluid (fluid flow shear stress) (Fig. 6).

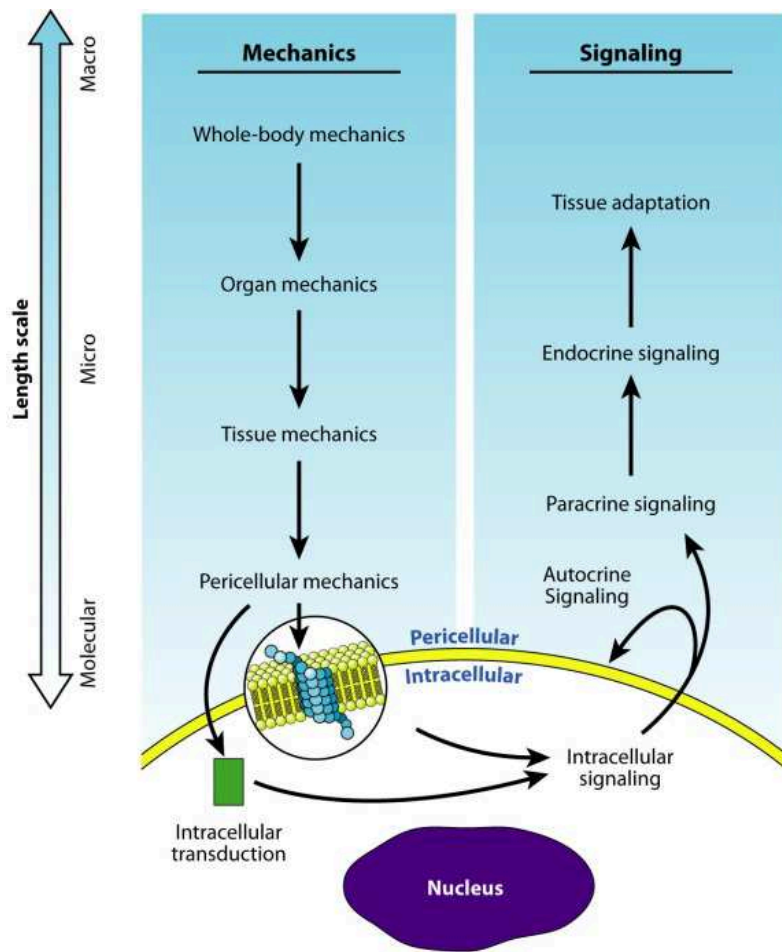


Figure 6 Different scales of mechanical loading perception and reaction on it. From [27]

The exact mechanism of mechanotransduction remains unclear. There are three major players: the cell body, cell processes, and cilia (primary cilium, a single hair-like projection), which can separately or in conjunction sense and transmit mechanical stimuli [27]. Recently, studies with cells loaded by fluid flow shear stress on their dendrites or cell bodies shown that the glycocalyx on the surface of dendritic processes plays a greater role in mechanotransduction, then the cell body [28].

It has been proposed that the fluid flow shear stress is perceived by integrins, which are acting as a linker between the osteocyte processes and canalicular walls, and received signal is likely to be transmitted between the osteocyte cell body and dendrites through the hemichannels [29,30]. It was found that integrin $\alpha 5\beta 1$ directly interacts with Cx43 hemichannel expressed on a membrane surfaces to mediate its opening [29]. It leads to release of the important bone anabolic molecules such as prostaglandins (PGE_2) and ATP into the lacunar-canalicular fluid where it can act in an autocrine and/or paracrine fashion.

As the current work is focused on aspects of bone adaptation to gravity, mechanosensitive osteocyte proteins (expression of these proteins is regulated by mechanical loading) controlling bone remodeling (Sclerostin) and/or mineralization (DMP1) are our primary interest. Sclerostin is a protein selectively produced by osteocytes, product of *SOST* gene, which negatively regulates bone formation and loss of it causes high bone mass disorders [31,32]. It binds to Lrp 5 Wnt coreceptors on osteoblast cell membrane, antagonizes Wnt/ β -catenin pathway, and, therefore inhibits osteoblasts differentiation, activity, and survival [33]. It has been demonstrated that Lrp5 (cell surface receptor, low-density lipoprotein receptor-related protein 5) [34] and the Wnt/ β -catenin signaling pathway [35] are required for bone formation in response to mechanical loading. Wnt proteins are secreted glycoproteins, and they bind extracellular cysteine-rich domain of Frizzled transmembrane proteins. The interaction of Wnt and Frizzled receptors is moderated by co-receptor Lrp5. The key points of the pathway are a glycogen synthase kinase (GSK)3 suppression, inactivation of β -catenin destruction complex, accumulation and translocation of β -catenin to the nucleus, binds to transcription factors and activates Wnt target gene expression [36] (Fig. 7).

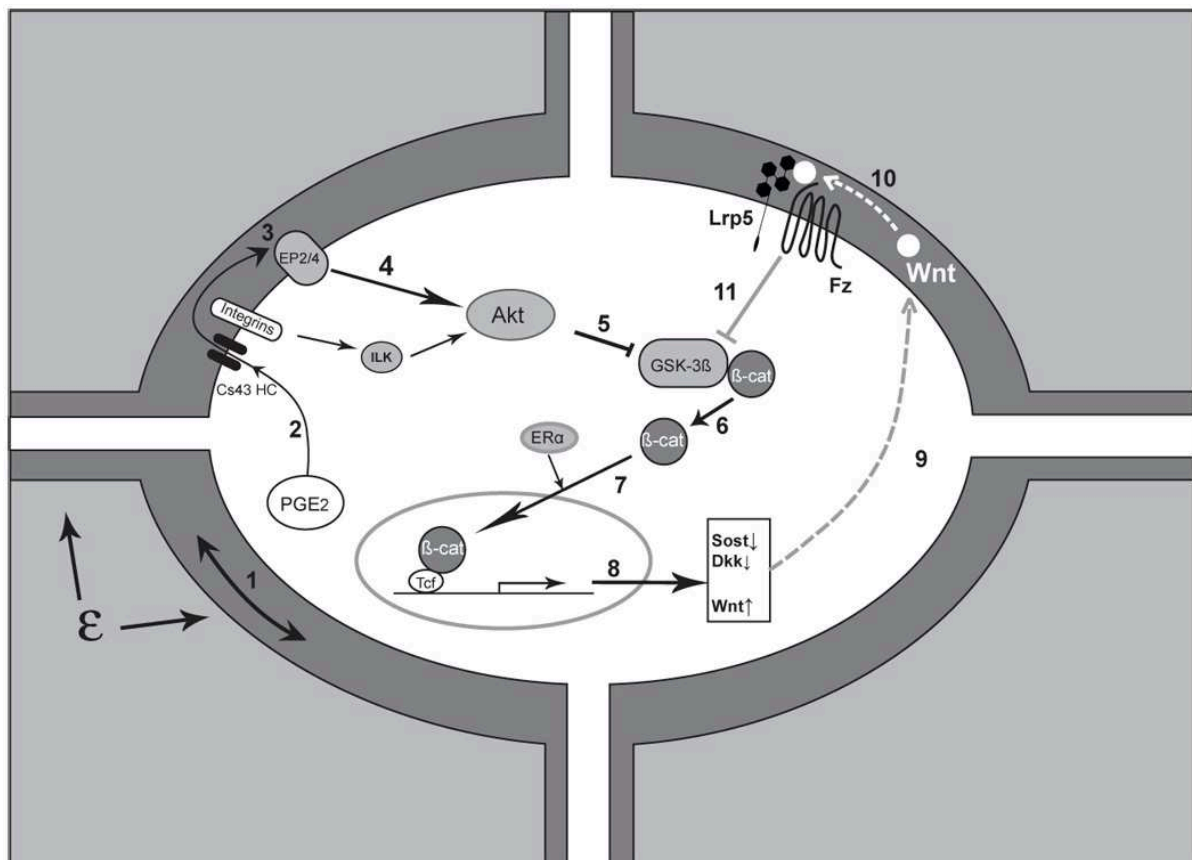


Figure 7. Triggering of the Wnt/ β -catenin pathway in osteocytes in response to load. 1) Mechanical loading perception. 2) Release of PGE₂ is triggered. 3) PGE₂ binds to its EP2/4 receptor. 4) Akt (serine/threonine kinase) - mediated downstream inhibition (5) of glycogen synthase GSK-3 β . 6)

Accumulation of the free intracellular β -catenin. (Integrin activation can also lead to Akt activation and GSK-3 β inhibition). 7) Nuclear translocation of β -catenin, which leads to changes in the expression of a number of key target genes. 8) The consequence is the reduction in Sclerostin. 9) Increase of Wnt expression. 10) Creation of a favorable environment for the Wnt binding to Lrp5-Frizzled. 11) Amplification of the load signal. From [30].

Sclerostin is the potent paracrine regulator of osteoblastic activity whose osteocyte expression has been found to be directly proportional to mechanical strain in bone [37]. Also it has been showed that *SOST* downregulation is required for bone osteogenic response to loading [38]. Contrary to mechanical stimulation, unloading (during a bed rest or chronic spinal cord injuries) results in bone loss together with the increase of circulating Sclerostin levels [39,40]. Significant role of Sclerostin in orthopedic disorders (Fig. 8) makes it an important target for therapies, especially with a recently invented antibody against Sclerostin [41].

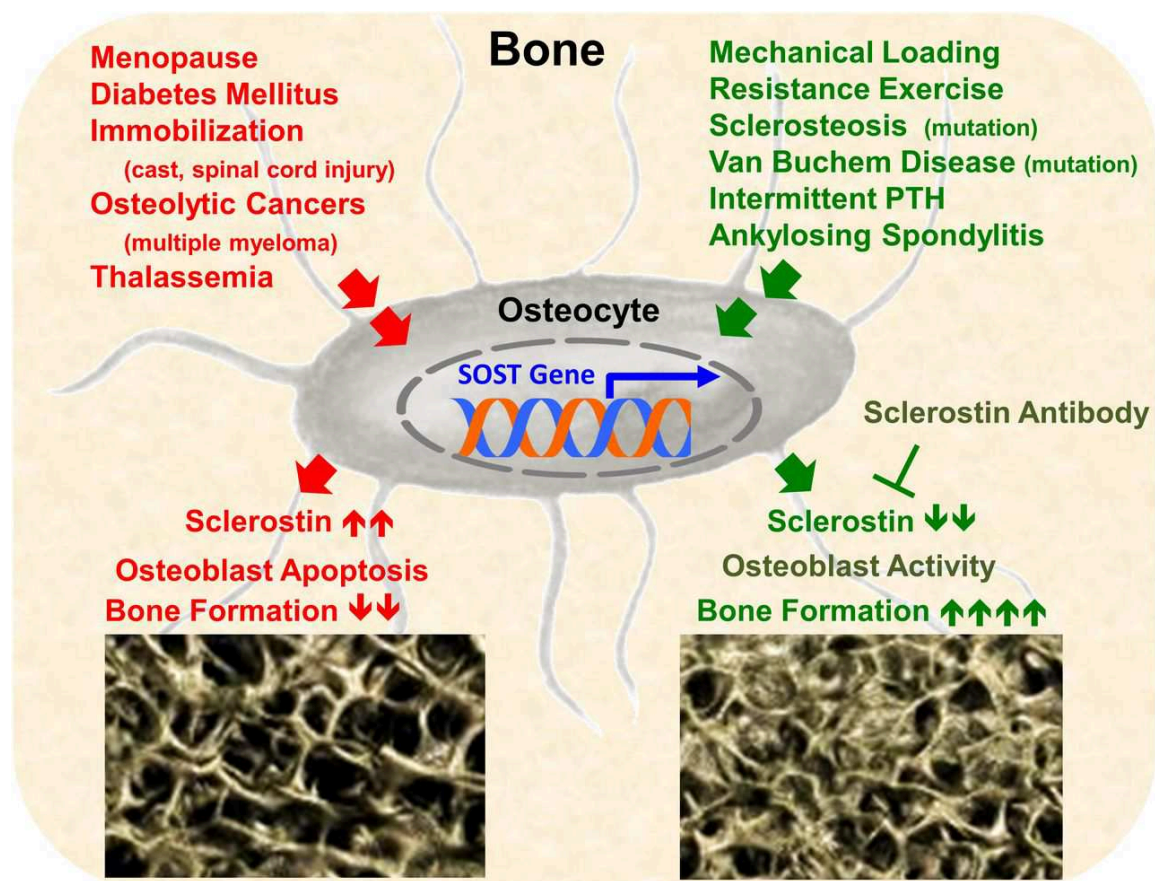


Figure 8. Role of Sclerostin in pathological conditions. From [41].

Another osteocyte protein that is of interest to us is DMP1. It is a member of SIBLING (small, integrin-binding ligand, N-linked glycoprotein) family [42], and its main function is regulation of mineralization [43]. Thus, *Dmp1*-null mice have a severe impairment in mineralization resulting in an osteomalacia, together with hypophosphatemia and highly elevated levels of FGF23 [22]. Interestingly, osteocytes of these mice preserved their expression of type I collagen, alkaline phosphatase, and Osterix, but failed to express mature osteocyte markers, such as Sclerostin [22], indicating that osteocyte differentiation was arrested at an early stage. It has been shown that the defects in mineralization and in osteocyte maturation can be reverted by restoration of normal phosphate homeostasis [44]. Therefore, the role of DMP1 in these processes might be linked to its role in the regulation of phosphate homeostasis. In addition, DMP1 expression is upregulated by mechanical loading [45,46], which makes it an interesting subject of analysis for the current research project.

1.2 Bone adaptation to altered gravity: space flights and countermeasures

1.2.1 Microgravity

As humanity has been evolving under constant gravitational conditions, microgravity is a severe challenge for all organ systems. In space, apart from microgravity other factors contribute toward hostile environment of a spaceflight: altered energy balance and biorhythms, high CO₂ level, confinement, space motion sickness, physiological effects and immune dysregulation [47,48]. For example, exposure to weightlessness results in substantial loss of muscle mass and function [49], cardiovascular and vestibular systems function [50,51], and bone mass [52]. As it was discussed above, bones are constantly adapting to mechanical load, and osteocytes are able to perceive mechanical strain and transfer it into bio-chemical activity, and thus orchestrate modeling and remodeling processes. More than 50 years of Space exploration reveal a detrimental effect of microgravity on bones and emphasize role of gravity as the major provider of mechanical load on skeleton. The absence of gravity leads to losses in the static loading and ground reaction forces. However, they are not the only loading forces that become lost. When the gravity is no longer present, it could have impact on the skeleton through marked reduction in muscle tension forces needed to move the weightless limbs in addition to a loss of ground reaction forces. First reports of bone loss in Space are from Gemini missions (1962-1966), where significant bone loss was

observed in the finger phalanges and calcaneus [53]. The application of DXA imaging techniques in 1989 allowed researchers to measure regional bone loss in astronauts who had flown from 126 to 438 days. The analysis showed a pattern of lower-extremity bone loss and upper-extremities preservation during spaceflights. Regional losses were from 1.06% to 1.56% per month in spine, trochanter and pelvis, but there were no significant changes in arms [54,55]. More recent data from the International Space Station (ISS) missions confirmed previous observations. It has been detected that bone mineral density (BMD) was lost at rates 0.9% in spine and 1.5% in hip, with primarily loss of trabecular bone [56]. However, it could be assumed that bone mass loss is not linear.

In addition, there is another important concern: bone loss occurs within the first month at microgravity, whereas bone recovery at normal gravity on Earth was very slow. Thus, astronauts were unable to recover pre-flight BMD values within six months after landing [52] and mathematical modeling predicts a recovery period of up to three years after a six months space mission [57].

1.2.2 Countermeasures on ISS

It must be noted that a substantial bone loss is taking place despite countermeasures based on physical exercises. Before the ISS was constructed, only aerobic (treadmill, cycling) and muscle training devices were available at Mir and Skylab stations, including treadmill, ergometer, and resistance exercise devices, as well as bungees and expanders. However, the equipment cannot be used permanently and thus it is not able to provide constant bone loading, which is intermittent instead. The measurements of ground reaction forces during the use of treadmill demonstrate that the impact forces that crew members experienced on Earth are higher than those in weightlessness [58]. The same level of forces generated during the treadmill activities on the ground cannot be reached in space, even though the treadmill used on space station has bungees to keep the crew member in contact with its surface [59]. While aerobic exercises in weightlessness do not provide mechanical loading high enough for bone mass maintaining, resistive exercises have shown promising results as a countermeasure to bed rest-induced bone loss [60,61]. The interim resistive exercise machine (iRED) was installed on the ISS, but unfortunately it has not prevented microgravity-induced bone loss [62]. Even the advanced resistive exercise device (ARED), installed on the ISS in 2008, which provided better protection against the decrease of BMD in comparison to previous systems (absolute loads of ARED is 2675N compare to 1337 of iRED), cannot be claimed to be fully efficient at all times (Fig. 9) [62].

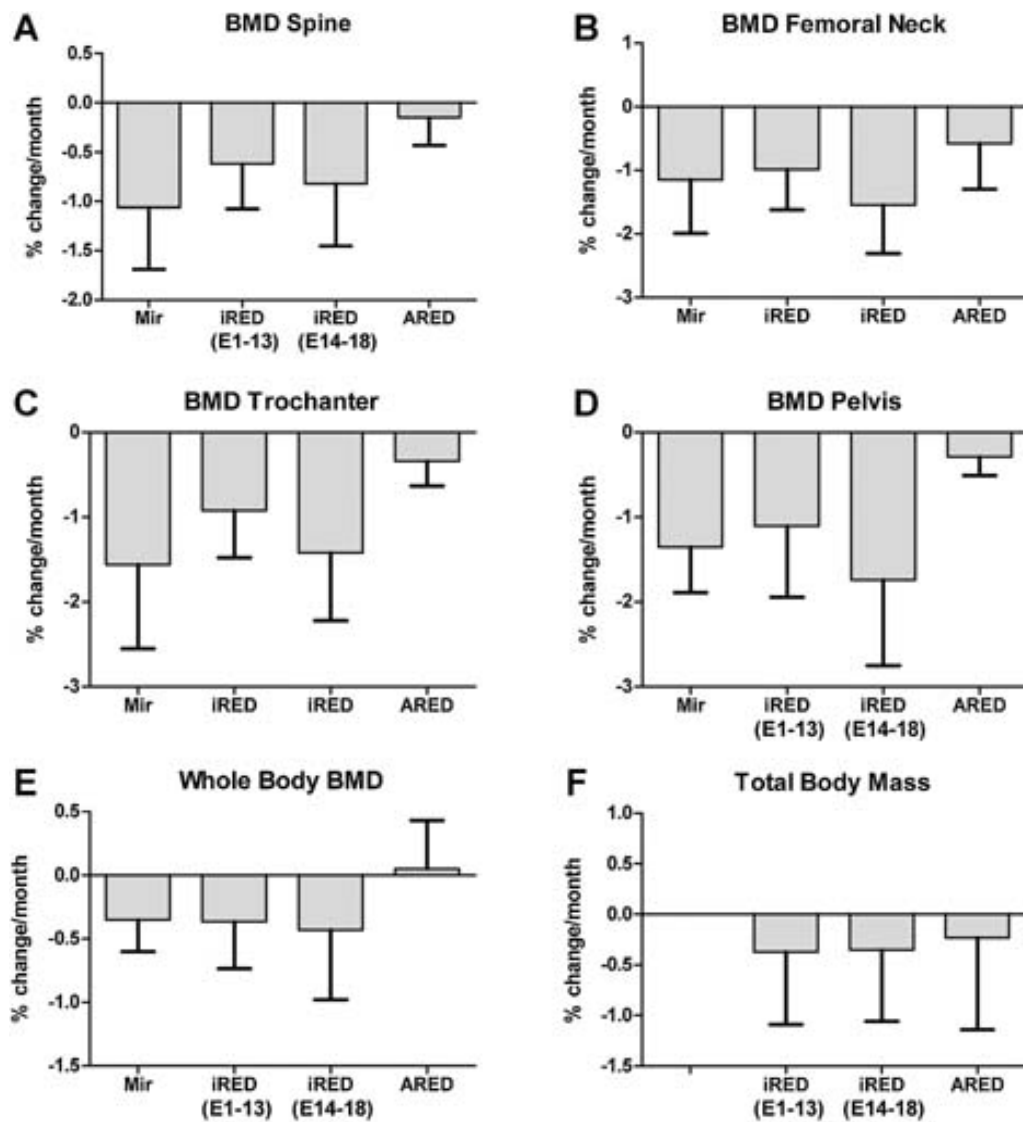


Figure 9. Bone mineral density (BMD) and body composition (expressed as % change per month \pm SD) in crewmembers on the Russian space station Mir, on earlier ISS flights (iRED, Expeditions 1–13), and reported in this work (iRED, Expeditions 14–18, and ARED). Femoral neck, trochanter, and pelvis changes are for the left hip for the iRED and ARED subjects. (A) Spine BMD. (B) Femoral neck BMD. (C) Trochanter BMD. (D) Pelvis BMD. (E) Whole-body BMD. (F) Total body mass. Mir total body mass data were not available. From [62].

1.2.3 Artificial gravity

As humanity considers exploration class space missions, the maintaining of health status and performance has become increasingly important. The goal of a countermeasure is not to keep the pre-flight fitness level, but rather to ensure performance level required to safely perform duties during the mission, and to minimize possible hazardous effects of spaceflight conditions. One of the potential solutions for mitigating the detrimental effects of space flight

is the controlled exposure of the subject to artificial gravity during the spaceflight or to hypergravity after the flight. Rotation of the spacecraft to induce a gravitational field with current technological level is not achievable, however a short-arm centrifuge, which can be used in multiple ways to impose a variety of forces on different physiological systems during a spaceflight seems to be a more realistic option [63].

The centrifugation can be used to reconstruct gravitational loading that could efficiently protect bone, skeletal muscles, cardiovascular system, etc., which makes it possible to prevent the physiological deconditioning, associated with microgravity [64]. However, in the first place, main questions of the gravitational countermeasures should be answered: 1) What is the optimal g-level? 2) How often should it be applied? 3) How long should it be applied for?

Hypergravity experiments are important not only for countermeasures or potential treatment development. Nowadays little is known about fundamental effects of chronically altered gravity on different organ systems, development of organisms, adaptation and safety limits [65], which is particularly important in the light of the recent projects associated with long-term exposure to altered gravity, such as a Mars colonization project. Moreover, gravitational studies may shed light on the mechanotransduction pathways and their regulation, which is the key to the efficient treatment of osteoporotic conditions. Even though bone-related hypergravity experiments started in the 70's and revealed alterations of bone mineral composition, density, structure and growth in rats [66–69] and mice [70,71], at the present moment the experiments with different gravity levels on mammalian skeleton are still not very common. Therefore the current research project focuses on multi-scale assessment of hypergravity effects on bone tissue. Our primary goal was to assess osteogenic or stress effects of continuous hypergravity, and future studies might address such questions as optimal duration and frequency of hypergravity exposure. An information relevant to published studies can be found in the paper “Effects of chronic hypergravity: from adaptive to deleterious responses in mouse skeleton”.

1.2.4 Whole body vibration

As it was described above, one of the major regulators of bone remodeling is mechanical loading. Thus, functional loading is crucial for achieving and maintaining bone quality and quantity, and reduction of loading results in a weakened bone structure. However, moderate physical exercises do not trigger significant increase of bone mass [72], and another

important moment is that in order to be anabolic for bones, mechanical loading must be dynamic, as static loads are known to induce bone loss [73], indicating that bone adaptation to mechanical loading is non-linear. Additionally, bone adaptation depends not only on intensity of loading but also on a number of loading cycles [74]. Thus bone formation can be activated by either low number of high-impact signals or by thousands of low-impact strain events. On the Fig. 10 interrelationship between bone adaptation and mechanical loading is demonstrated based on turkey ulna model, which was challenged by high number (108000) micro-strain events [74].

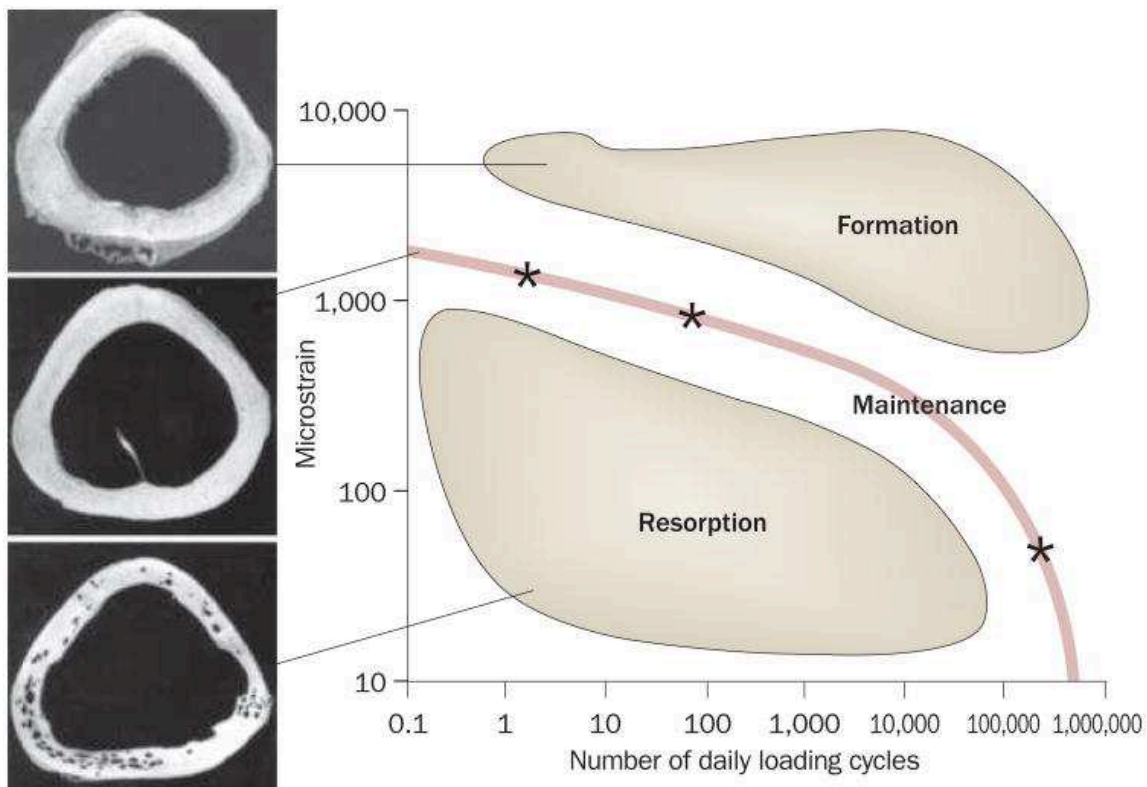


Figure 10. Non-linear relationship between mechanical loading magnitude, number of loading events and bone adaptation. Bone is preserved with either four cycles per day of 2,000 microstrain, 100 cycles per day of 1,000 microstrain, or hundreds of thousands of cycles of signals of well below 10 microstrain (each represented as a star). From [75].

Taking into consideration all the above, there is another approach to preventing disuse, microgravity or age-related bone loss besides hypergravity. It is mechanical stimulation with relatively low-magnitude but high frequency whole body vibration (WBV). Importantly, WBV has benefits compared to traditional physical exercises or centrifugation because in a relatively short period of time it can provide sufficient mechanical stimulation without significant efforts from a recipient, which is critical for individuals with impaired mobility

and attenuated muscle strength. A very first evidence of low-acceleration high-frequency vibration efficiency was provided in a study of Rubin et al. from 2001 where it has been demonstrated that one year of vibration at 0.3g/30Hz led to significant 30% increase of the trabecular bone volume and density, as well as bone strength and stiffness [76]. In the recent 14 years WBV studies on both animals and humans have become very frequent in the bone field. However, despite the large amount of available data, it is difficult to conclude which WBV protocol is the most beneficial for bones. The reason for heterogeneity of results is that WBV protocols are very flexible in relation to vibration parameters: frequency, acceleration, and therefore amplitude are variable [77]. Duration and frequency of exposure to WBV [77], as well as resting periods between WBV sessions have been shown to be important [78], and finally effects of WBV vary from one animal model to another [77]. The majority of research was done with low-acceleration (below 1g) and frequencies from 30 to 50Hz, and while exposure to WBV has been primarily associated with an anabolic skeletal response, several studies have not detected such effects in animal [79,80] or human studies [81].

Analysis of published animal studies reveals a common tendency that low-acceleration WBV has beneficial effects on osteopenic animals (ovariectomized, unloaded or immobilized), but in most cases it fails to stimulate bone formation in control animals. At the same time, effects of high-acceleration (above 1g) WBV are much less investigated, and there are few animal studies exploring it. However, despite the high g-level, WBV at 2g/50Hz and 3g/30Hz appeared osteogenic for ovariectomized animals but not for controls [82,83].

A relevant to WBV studies information can be found in the paper “High-acceleration Whole Body Vibration stimulates cortical bone accrual and increases bone mineral content in growing mice”.

2. Objectives of the current research project

The problem of bone loss caused by the lack of mechanical loading is still not solved. Both centrifugation and whole body vibration might be efficient countermeasures against microgravity- or disuse-induced bone loss; however the most efficient regimes are yet to be identified.

Taking this into consideration, the main objective of our research project was understanding the bone tissue and bone cells behavior under different vectors and modalities of hypergravity: long-term centrifugation and whole body vibration. Particularly, our goal was to find hypergravity conditions which would be osteogenic and not stressful for animals. Such studies of fundamental processes of skeleton adaptation to gravity-induced mechanical loading may shed light on potential countermeasure or treatment strategies.

Apart from biological questions, our research project aimed at developing a new investigation technique. As it was underlined above, Sclerostin and DMP1 are two mechanosensitive osteocyte proteins (their expressions change according to mechanical loading applied), which control bone formation and mineralization. We wanted to have a tool which would allow us to localize these proteins on bone samples and immunohistochemistry (IHC) seemed to be a perfect solution.

Among published papers there are no well-established protocols for IHC detection of osteocyte proteins, thus we had to design our own. Moreover, our aim was not only to perform a high quality IHC but also to quantitatively assess protein expressions. Most of the published papers in the bone field have had no quantitative analysis of IHC data or they used manual quantification of IHC signals without reporting any validation of their protocols. We identified the following issues with presentation of IHC data in bone-related papers: low overall histological or IHC quality; almost no quantification but only demonstration of two caricature images; no justification for selection of particular region of interest (ROI) for IHC analysis; ROI that only includes few cells and might be not representative. Thus, the technical objective was to develop a flexible quantitative IHC technique, which in addition to reproducible labeling of osteocyte proteins would allow us to quantify protein expressions on large areas, while taking into account hundreds of osteocytes in order to detect even slight

alterations. This technique also had to be easy in use and no require expensive software or hardware.

2.1 Biological objectives

The study of skeleton adaptation to chronic exposure to different levels of hypergravity by centrifugation and to intermittent hypergravity by whole body vibration pursued the following objectives: (a) assess alterations of mass-structural parameters of weight-bearing and non-weight-bearing bones; (b) analyze cellular response in relation to bone formation and resorption parameters, (c) assess alterations of osteocyte mechanosensitive proteins production, which control bone remodeling or mineralization.

2.2 Technical objectives

The technical objective was to develop an immunohistochemistry-based technique, which would allow us to identify co-localized osteocyte proteins and assess them quantitatively on human or mice bones in most popular embedding materials: paraffin and methyl methacrylate.

3. Results

3.1 Skeleton adaptation to chronic hypergravity

3.1.1 Introduction to the paper

Hypergravity studies, particularly long-term hypergravity exposure are still very rare in the bone field, and the current research is a pioneering one. Our laboratory has been equipped with an animal centrifuge facility, which allowed us to perform continuous long-term hypergravity studies with acceleration forces up to 5g. Previous studies with this centrifuge addressed effects of hypergravity on muscles in mice. A 21-day hypergravity study with mice of the same type and age revealed that centrifugation acted as endurance training on muscle force until 3g and became deleterious at 4g [84]. Thus, we were interested in investigating the effects of 2g and 3g conditions on skeleton. An “AdapHyp” program of ANR (Agence Nationale de la Recherche) financed the multi-scale hypergravity research, where the effects of chronic 21-day continuous 3g and 2g hypergravity on stress response, vestibular and immune system, muscle functions, cognitive abilities, and skeleton were assessed. Published papers described that although 3g acted as an endurance training on muscles [84], higher corticosterone level and anxiety behavior revealed a stress response after 3g centrifugation but not 2g. Also, after 3g there was a strong decrease of pro-inflammatory chemokines and cytokines, as well as increase of concentration of serum IgG [85]. In addition, both 3g and 2g impaired spatial learning [84].

3.1.2 Paper #1: “Effects of chronic hypergravity: from adaptive to deleterious responses in growing mouse skeleton”

Vasily Gnyubkin^a, Alain Guignandon^a, Norbert Laroche^a, Arnaud Vanden-Bossche^a, Myriam Normand^a, Marie-Hélène Lafage-Proust^a, Laurence Vico^a

^a INSERM U1059, laboratoire de Biologie intégrative du Tissu Osseux, Université de Lyon, Saint-Etienne, France.

Running head: Chronic hypergravity and bone.

Corresponding author: Laurence Vico

Email: vico@univ-st-etienne.fr

Address: 10 rue de la Marandiere, 42270, Saint Priest en Jarez, France

Phone: +33 4 77 42 18 57

Abstract

One of the most important but least studied environmental factors playing a major role in bone physiology is gravity. While the knowledge of deleterious effects of microgravity on the skeleton is expanding, little is known about hypergravity and its osteogenic potential.

Centrifugation was used to assess effects of 21-d continuous 2g or 3g acceleration on femur and L2-vertebra of 7 week-old male C57BL/6 mice.

Under 3g, body mass growth slowed down, and deleterious skeletal effects were found ($p < 0.05$ compared to control): cortical thinning, osteoclasts surface increase (+41% in femur; +20% in vertebra), and bone formation rate decrease (-34% in femur; -38% in vertebra). A 2g centrifugation did not reduce body mass, and improved trabecular volume (+18% in femur; +13% in vertebra) and microarchitecture (+32% connectivity density in femur; +9% trabecular thickness in vertebra, $p < 0.05$ compared to control). 2g also decreased osteoclast surfaces (-36% in femur; -16% in vertebra) and increased the extent of mineralized surfaces (+31% in femur; +48% in vertebra, $p < 0.05$ compare to control). Quantitative immunohistochemistry revealed an increase of dentin matrix acidic phosphoprotein 1 (DMP1) and decrease of Sclerostin (+60% and -35% respectively, $p < 0.001$ compared to control) in the femur cortex of 2g mice. In the distal femur metaphysis the number and volume of blood vessels increased by 22% and 44% respectively ($p < 0.05$ compare to control).

In conclusion, the effects of continuous hypergravity were bone compartment-specific and depended on the gravity level, with a threshold between beneficial 2g and deleterious 3g effects.

Keywords: Osteocytes, Sclerostin, DMP1, μ CT, Immunohistochemistry, Bone vascularization.

Introduction

The evolution of life on Earth has always been determined by variations environmental factors. While some conditions have changed over time, the gravity has remained constant. Alterations of gravity (microgravity or hypergravity) are unique severe challenges for living beings. Spaceflights are an example of such challenge, as weightlessness leads dramatic physiological deconditioning from cellular (8) to organ systems level (64).

In relation to skeleton, spaceflight-related site-specific decrease of bone mass has been observed in astronauts since the 1970s. Importantly, the weight-bearing sites of skeleton are those most affected by microgravity (30, 61). For example, monthly decrease of bone mineral density (BMD) in lumbar spine and hip could reach 1.5% of total bone mass (27, 29). Even though recently developed countermeasures, such as an advanced resistive exercise device on the International Space Station, provide better protection against the decrease of BMD than previous systems, still it is not always fully efficient (49, 51). In addition, bones are unable to rapidly restore their initial BMD after spaceflights (61). Mathematical modeling revealed that most crew members who have participated in 4-6 months space missions would return their BMD to pre-flight level within 3 years (50).

Spaceflights provide a unique opportunity for studying chronic microgravity effect, however such experiments are rare and expensive. Hypergravity based on centrifugation is more accessible. It allows dose-dependent effects of gravity on living beings (5, 62) and adaptation mechanisms to altered gravity (3, 42) to be investigated. What could also be assessed is a capacity of hypergravity as a countermeasure against physiological deconditioning in space (7).

Short-time centrifugation (from minutes to hours) showed limited ability to prevent bone loss associated with unloading. Thus, in humans, daily centrifugation for one hour at 2.5g did not prevent bed-rest induced bone loss (52), even when combined with ergometric exercises (23). In rats, one hour daily centrifugation at 1.5 or 2.6g did not prevent tail-suspension-induced bone loss (67). However, site specific increase of BMD and BMC in the cervical spine was

found in military pilots after repetitive exposure to high head-feet directed acceleration (positive Gz loading) (36, 37).

In contrast to short-time hypergravity, rats centrifuged for 4 days at 2g, showed increase of both bone formation activity and trabecular thickness in the tibia metaphysis (57). Exposure to 2.9g for 28 days was similarly beneficial, and it led to a trabecular bone volume increase in both ovariectomized and sham-operated rats compared to controls (22). Also, site-specific increase of bone mass was observed after three months of chronic exposure to 2.5g in dogs (40).

Centrifugation is still a rare experimental model, and available data assessing the impact of hypergravity on different organ systems are very limited, in particular for vulnerable growing organisms. Therefore, several laboratories decided to perform a comprehensive study designed to assess safety and effects of chronic 21-day continuous 3g and 2g hypergravity on stress response (18), vestibular (3) and immune system (18), muscle functions, and cognitive abilities (3). In the first stage of the program, focused on young mice, our team aimed to analyze skeleton response to hypergravity and to find a g level, which would be osteogenic. While, the skeleton of young animals has been shown to benefit more from mechanical loading than adults (48, 55, 56), the potential impairment of the growth process (45) also had to be assessed.

As we found that 21-day centrifugation at 2g stimulated bone formation, we repeated the experiment to assess effects on bone vascularization and osteocyte proteins expression. Angiogenesis and bone remodeling have proved to be closely linked when mechanical loading is altered (1). Thus, treadmill running increases trabecular bone mass, and stimulates bone formation and angiogenesis (65). Therefore, we hypothesized that chronic centrifugation would alter the bone vascular network, and we assessed vascularization parameters using previously validated quantification technique (47).

Sclerostin and Dentin Matrix acidic Phosphoprotein 1 (DMP1) were selected for immunohistochemistry analysis of osteocyte protein expression (4), as their expression is affected by mechanical loading (15, 20, 46) and because they control bone formation (31, 33) and mineralization (12, 32, 34).

Materials and Methods

Animals

Seven-week-old C57BL/6J male mice (Charles River Laboratories, l'Arbresle, France) were used for all experiments. At the end of each experiment, the mice were euthanized with cervical dislocation; femurs and lumbar vertebrae were dissected out and processed as described below. Protocols and animal procedures followed the European Community standards on the care and use of laboratory animals (Ministère de l'Agriculture, France, Authorization n°42-21-080) and were approved by the local Animal care and use committee (Comité d'Ethique en Expérimentation Animale de la Loire - Université Jean Monnet, CEEAL-UJM).

Material set-up

Mice were housed by four in standard cages (36x20x14cm) with bedding material, in a quiet room with constant temperature (22°C), 50% relative humidity, and a 12/12h light-dark cycle. Food and water were provided ad libitum (Safe diets A04, Augy, France). After a week of habituation, cages were transferred into the centrifuge's gondolas preserving the same environmental conditions. The centrifuge (COMAT Aérospatiale, Flourens, France) made it possible to maintain a permanent level of hypergravity for 21 days. A centrifuge with a radius of 1.4m, had four gondolas hanging on the periphery (S1 video) (24). Each gondola can accommodate up to 3 cages. All gondolas were equipped with a video surveillance system to control animals' condition and food/water stocks. Animals were provided with enough food and water for the whole duration of the experiments, thus the centrifuge was stopped only twice (six and two days before euthanasia) for five minutes each time, to inject animals with tetracycline for dynamic histomorphometry (see below). We performed three experiments lasting 21 days: one at 3g and two at 2g. Control mice were also placed into gondolas to mimic experimental conditions, but were not exposed to centrifugation.

Experimental groups

In the first 3g and 2g experiments, 24 mice were randomly and equally divided in control and experimental groups (n=12 per group). At the end of experiments, animals were processed for microcomputed tomography (μ CT) and histomorphometry. For the second 2g experiment, 30 mice were randomized in two equal groups (control and experimental, n=15 per group). At the end of an experiment, femurs of five animals in each group were isolated and processed for immunohistochemistry (IHC) analysis. Others were analyzed for bone vascular

parameters as described below. In all experiment euthanasia and dissection were performed within 3 hours after the end of centrifugation. Tissue collection was done within 15-20 minutes after euthanasia.

Investigation tests

Microtomography

Formalin-fixed and ethanol-dehydrated femur and L2 vertebral body were scanned with a high-resolution μ CT (Viva CT 40; Scanco Medical, Switzerland) and analyzed as described in David et al (10). Data were acquired at 55keV energy and 145 μ A current for 10 μ m cubic resolution. Right femur trabecular bone was scanned within the metaphysis below the growth plate, and the cortical bone was scanned in the diaphysis; L2 vertebra was scanned entirely (Fig. 1). Three-dimensional reconstructions were generated with the following parameters: Sigma: 1.2, Support: 2, Threshold: 160 (spongiosa) or 280 (cortex). In distal femur metaphysis, the secondary spongiosa was evaluated above the distal primary spongiosa and the cortical bone was evaluated at the level of diaphysis; in L2 vertebral body secondary spongiosa was evaluated between two primaries (Fig. 1). 3D structural parameters were obtained from 60 sections (0.6mm) for both trabecular and cortical bone in femur, and from 180 sections (1.8mm) for trabecular bone in L2 vertebral body. Regions of interest (ROI) were manually defined by an operator (Fig.1).

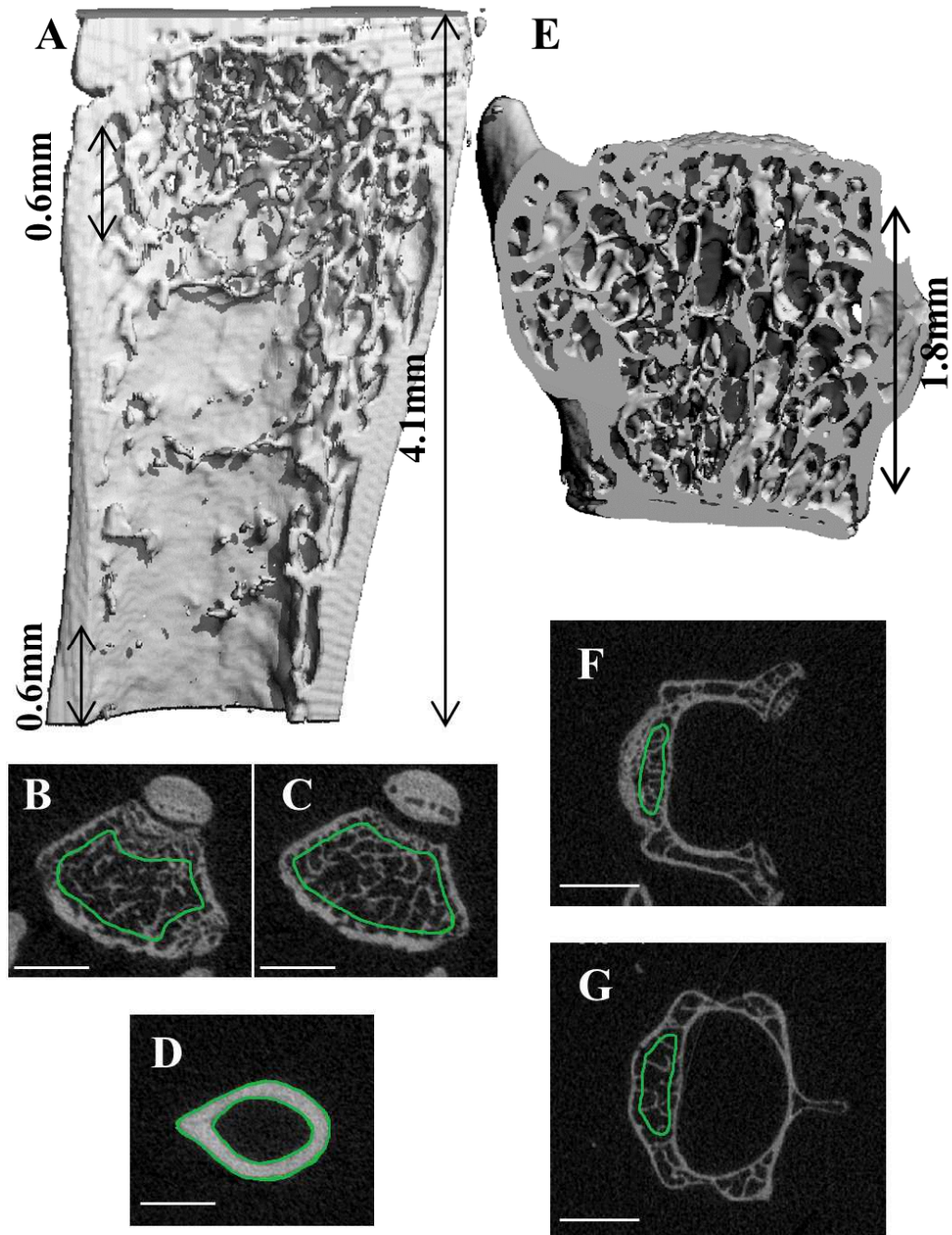


Figure 1. Locations of the Regions Of Interest for μ CT analysis of trabecular and cortical bones. Mice femur, scanned area of 4.1 mm height (A), manual selection of regions for analysis on distal metaphysis (0.6 mm) close to the primary spongiosa (B), in the middle of the secondary spongiosa (C), and in the diaphysis (0.6 mm) (D); L2 vertebral body, scanned area (E), manual selection of regions (1.8 mm) for analysis close to the primary spongiosa (F), and in the middle of the secondary spongiosa (G). Scale bar 1 mm.

For cortical bone, we measured: bone mineral density (BMD, mg/cm^3), cortical thickness (Ct.Th, mm), and cortical area (Ct.Ar, mm^2). For trabecular bone, we measured trabecular thickness (Tb.Th, μm), trabecular number (Tb.N, mm^{-1}), trabecular separation (Tb.Sp, μm),

bone volume (BV/TV, %), connectivity density (Conn.D, mm^{-3}), structural model index (SMI), and degree of anisotropy (DA).

Histomorphometry

Centrifugation was stopped twice for 5 min six and two days before death and mice were injected intraperitoneally with 200 μl of a 0.37% tetracycline solution. Distal femur metaphysis and L2 vertebral body were processed undecalcified for histomorphometry as described (9). Bone cellular parameters were measured semi-automatically with digitizing tablet (Summasketch; Summagraphics, Paris, France) and software designed in our laboratory (9). In brief, we evaluated longitudinal growth rate (LGR, $\mu\text{m}/\text{day}$) by measuring the distance in $\mu\text{m}/\text{day}$ between two fluorochrome labelings (parallel to the growth plate) in the primary spongiosa. In the secondary spongiosa we measured double labeled surfaces (dLS/BS, %) and mineral apposition rate (MAR, $\mu\text{m}/\text{day}$), from which the bone formation rate (BFR/BS, $\mu\text{m}^3/\mu\text{m}^2/\text{day}$) was calculated. Osteoid surfaces (OS/BS, %) were detectable in femurs only. Osteoclasts surfaces (Oc.S/BS, %) were assessed through tartrate-resistant acid phosphatase (TRAP) labeling.

Bone vessel quantification

Vascular assessment was processed as previously described by Roche et al (47). In brief, after intracardiac perfusion of pre-warmed contrasting solution (50% BaSO₄ (Micropaque Guerbet, Paris, France), 1.5% gelatin in PBS) with a peristaltic pump (MasterFlex, L/S, Cole-Parker Instrument, Germany), femoral bones were embedded in medium for frozen sections (Neg50, Thermo Scientific, Ref. 6502) by snap-freezing in liquid nitrogen. Nine μm -thick sections of whole bone were cut with 27 μm increments with a cryotome (Microm HM 525, Thermo Scientific). The secondary spongiosa of the distal femur was selected as ROI (4 fields of 0.26 mm^2), and manually analyzed with a 100-point eyepiece square-grid. Vessels number per marrow area (Ves.N/Mar.Ar, 1/ mm^2), and vessel volume per marrow volume (Ves.V/Mar.V, %) as defined in (47) were assessed.

Circulating Sclerostin immunoassay

Immediately after euthanasia, blood from animals of control group and those exposed to 2g centrifugation was collected. Serum was isolated by 10 min centrifugation at 4400g, aliquoted and stored at -80°C. The Quantikine mouse/rat Sclerostin ELISA kit (R&D systems, MSST00) was used in accordance with the manufacture protocol. As indicated on a manufacture's website (<https://www.rndsystems.com/products/mouse-rat-sost-sclerostin->

quantikine-elisa-kit_msst00), coefficient of variation for this ELISA kit is up to 7.2% and 8% for intra – and inter-assay respectively.

Quantitative analysis of immunohistochemical data

For immunohistochemistry (IHC) femurs were fixed in 10% neutral buffered formalin and then in 70% ethanol. Three mm long sections of the mid-diaphysis (5 and 8 mm from the distal epiphysis) were cut out with a precision diamond wire saw (ESCIL Well, France), decalcified for 24 hours (Immunocal, Decal Chemical Corp., Ref 1440) and embedded in paraffin. Five μm thick transversal sections of the diaphysis were cut from the distal part with 250 μm increment with a microtome (Leica RM2245) and immunolabeled for Sclerostin (Primary antibody: polyclonal, goat, R&D Systems, AF1589, 1:400) and DMP1 (Primary antibody: polyclonal, rabbit, Takara, M176, 1:500). Sclerostin was detected using a biotinylated secondary polyclonal rabbit anti-goat antibody (Dako, E0466) and Streptavidin-Alexa Fluor (Life technologies, S 11225, 1:500). DMP1 was detected using a biotin-free ready-to-use PowerFluor immunofluorescence detection kit (MaxVision Biosciences, PF 21-M). Cell nuclei were visualized with DAPI (Santa Cruz, 28718-90-3).

Quantitative assessment of immunohistochemical data by measuring relative fluorescence has been previously proposed as a method for clinical pathology (14). We also used fluorescent IHC to perform semi-automatic quantitative analysis of proteins expression level in near-lacunar space. Our technique made it possible to conduct an osteocyte by osteocyte analysis. Black and white pictures of the entire cortical area were obtained with an AxioObserver Z1 microscope (Zeiss, Darmstad, Germany), at a magnification of 400 (oil immersed objective), and automatically merged using the Mosaic plugin of Axiovision 4.7 software (Zeiss). Immunolabeling and imaging were done with the same reagents and imaging parameters for all samples to minimize any possible variations. Mosaic images were directly analyzed with ImageJ software (<http://imagej.nih.gov/ij/>) without any brightness or contrast correction. A cortical bone ROI was manually defined. Bone marrow, periosteum, blood vessels, and cutting/staining artifacts were excluded from ROI. A mask of DAPI positive cells within the ROI was merged with Sclerostin or DMP1 staining to restrict the areas of measurements to areas of DAPI staining, providing fluorescence intensity data for individual osteocytes. As a lacunar size exceeds the area of DAPI staining, we applied two successive dilations of the DAPI mask to fit with lacunar area. The dilated DAPI does not entirely match the area of the osteocyte lacuna. Therefore the pixels of surrounding bone matrix having zero gray level

might be included in the ROI. Hence, parameters based on calculations of mean grey level were not appropriate for the analysis of fluorescence. Considering this, we used Raw Integrated Density (RawIntDens) parameter of ImageJ, which represents a sum of all pixels gray level within the ROI. Collagen and osteocytes autofluorescence was defined with the Plot Profile function of ImageJ from a negative control bone section (no primary antibody applied during IHC). The measured gray level of autofluorescence was removed with the Subtract function of ImageJ before evaluating fluorescence of proteins. To calculate intra- and inter-observer coefficients of variation we repeated measurements three times with the same operator and three times with a different operator on five histological sections. Each time every operator had to independently define an ROI and perform related measurements. Variations between measurements were always less than 2% and not statistically significant. To ensure representativity of osteocyte population we analyzed 2 to 3 entire cortical transversal sections per bone sample (approximately 450 osteocytes per section) from five animals per group; average number of analyzed osteocytes per group was 5000.

Statistical analysis

Data analysis was performed with the STATISTICA[®] software (version 8.2; StataCorp, College Station, TX). Data were assessed with the non-parametric Mann-Whitney U-test.

Results

3g Centrifugation

After 21 days at 3g mice displayed 12% ($p \leq 0.001$) loss of body weight with a 22% ($p \leq 0.05$) decrease of LGR as compared to controls (Table 1 and 2). While Ct.Th and Ct.Ar were reduced by 5 and 11% respectively ($p \leq 0.05$), trabecular compartments of femur and L2 vertebral body did not change (Table 2, Fig.2). BFR/BS was reduced (-34%, $p \leq 0.05$) and Oc.S/BS increased (+41%, $p \leq 0.05$) in femur. In L2 vertebral body BFR/BS decreased by 36% ($p \leq 0.05$) and Oc.S/BS increased by 20% ($p \leq 0.05$) (Table 2, Fig.2).

Table 1. Animals body weight after centrifugation.

	Control	3g	Control	2g Exp 1	Control	2g Exp 2
Body weight,g	24 ± 2	21 ± 1*	25 ± 2	24 ± 2	24 ± 1	23 ± 1

Data are shown as mean ± SD. Non-parametric Mann-Whitney test, 3g or 2g compared to control, * $p \leq 0.05$.

Table 2. μ CT and histomorphometry analysis of femur diaphysis and distal metaphysis, and L2 vertebral body in control and 3g centrifugation groups.

Groups Treatment?	Femur		L2 vertebral body	
	Control	3g	Control	3g
Cortical bone				
BMD,mg/cm ³	1186 \pm 12	1190 \pm 11	ND	ND
Trabecular bone				
BV/TV,%	13.8 \pm 4	12.5 \pm 4	23.5 \pm 3	21.8 \pm 2
Tb.Th, μ m	38 \pm 5	34 \pm 7	40 \pm 4	38 \pm 2
Tb.N,mm ⁻¹	3.6 \pm 0.6	3.6 \pm 0.5	5.9 \pm 0.4	5.7 \pm 0.3
Tb.Sp, μ m	244 \pm 50	251 \pm 40	130 \pm 13	136 \pm 9
Conn.D,mm ⁻³	112 \pm 27	114 \pm 25	257 \pm 21	267 \pm 26
SMI	2.4 \pm 0.4	2.6 \pm 0.3	1.1 \pm 0.3	1.2 \pm 0.2
DA	1.62 \pm 0.08	1.56 \pm 0.13	1.84 \pm 0.11	1.78 \pm 0.07
OS/BS,%	17.9 \pm 3.8	11.7 \pm 4.6*	ND	ND
dLS/BS,%	27.5 \pm 6	22.1 \pm 4.9*	11 \pm 2	8.6 \pm 2.4*
MAR, μ m/day	1.2 \pm 0.1	1 \pm 0.06*	0.9 \pm 0.05	0.7 \pm 0.06*
LGR, μ m/day	11.1 \pm 1.7	8.7 \pm 1*	ND	ND

Data are shown as mean \pm SD. Non-parametric Mann-Whitney test, 3g compared to control, *p \leq 0.05, ***p \leq 0.001. ND – not done (parameters were too small for reliable measurements).

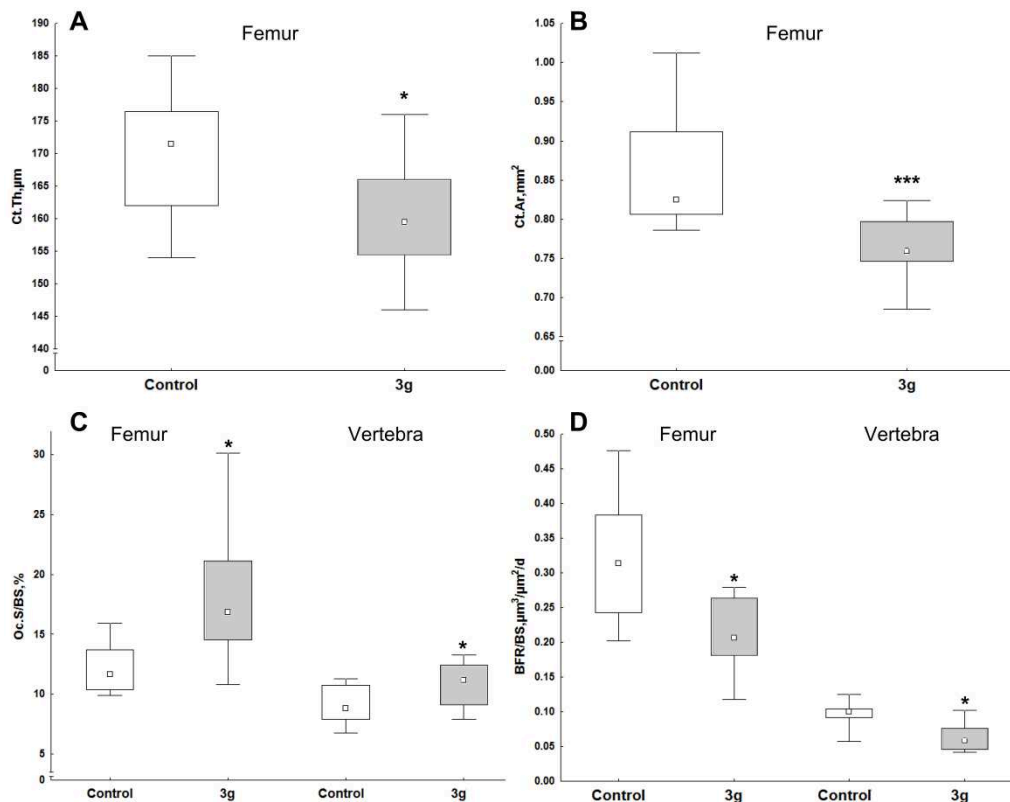


Figure 2. Microarchitecture and histomorphometry parameters in control and 3g centrifugation groups. Femoral distal metaphysis and L2 vertebral body: cortical thickness (Ct.Th) (A), cortical area (Ct.Ar) (B), osteoclasts surface over bone surface (Oc.S/BS) (C) and bone formation rate (BFR/BS) (D). Boxes represent 50% of values (25% to 75%), whiskers represent minimum and maximum values, middle point represents median. Non-parametric Mann-Whitney test, * $p \leq 0.05$, *** $p \leq 0.001$.

2g Centrifugation

Body weight

In both 2g experiments, at the end of the experiment there was no change in body weight compared to controls (Table 1).

μ CT and histomorphometry

In femur cortex, exposure to 2g did not change mass-structural parameters (Table 3). However, trabecular bone in both distal femur and vertebral body was affected. In femur there was an increase of BV/TV (+24%, $p \leq 0.05$), Tb.N (+18%, $p \leq 0.05$), and Conn.D (+36%, $p \leq 0.05$), and decrease of Tb.Sp (-22%, $p \leq 0.05$), and SMI (-17%, $p \leq 0.05$) as compared to controls (Fig. 3). Tb.Th and DA were not affected (Table 3). In vertebral body we found similar positive alterations: increase of BV/TV (+13%, $p \leq 0.05$) and Tb.N (+4%, $p \leq 0.05$), and decrease of Tb.Sp (-9%, $p \leq 0.05$), and SMI (-33%, $p \leq 0.05$). However, contrary to femur, Tb.Th increased by 9% ($p \leq 0.05$), and Conn.D was not affected (Table 3).

Bone cellular activities were altered in both femur and vertebral body regions. In femur 2g led to decrease of Oc.S/BS (-36%, $p \leq 0.05$), and increase of OS/BS (+33%, $p \leq 0.001$) and dLS/BS (+31%, $p \leq 0.05$). At the same time, we found a decrease of MAR (-15%, $p \leq 0.05$), and BFR/BS did not change (Fig. 3). There were also no changes in LGR (Table 3). In L2 vertebral body, we observed increase of dLS/BS (+48%, $p \leq 0.001$) and BFR/BS (+45%, $p \leq 0.05$), and a decrease of Oc.S/BS (-16%, $p \leq 0.05$). MAR remained unchanged (Table 3).

Table 3. μ CT and histomorphometry analysis of femur diaphysis and distal metaphysis and L2 vertebral body in control and 2g centrifugation groups.

Groups	Femur		L2 vertebral body	
	Control	2g	Control	2g
Cortical bone				
BMD,mg/cm ³	1212 \pm 13	1206 \pm 14	ND	ND
Ct.Th, μ m	184 \pm 16	178 \pm 12	ND	ND
Ct.Ar,mm ²	0.95 \pm 0.1	0.91 \pm 0.1	ND	ND
Trabecular bone				
Tb.Sp, μ m	206 \pm 60	161 \pm 21*	126 \pm 16	115 \pm 6*
SMI	2.1 \pm 0.5	1.8 \pm 0.3*	0.9 \pm 0.4	0.6 \pm 0.2*
DA	1.56 \pm 0.12	1.51 \pm 0.04	1.76 \pm 0.09	1.76 \pm 0.08
OS/BS,%	16.5 \pm 3.1	22 \pm 3***	ND	ND
dLS/BS,%	13.8 \pm 4.9	18 \pm 4.4*	6 \pm 1.3	8.9 \pm 2.5***
MAR, μ m/day	1.2 \pm 0.1	1 \pm 0.18*	0.86 \pm 0.05	0.83 \pm 0.07
LGR, μ m/day	11.2 \pm 1.9	10.2 \pm 2.1	ND	ND

Data are shown as mean \pm SD. Non-parametric Mann-Whitney test, 2g compared to control, *p \leq 0.05, ***p \leq 0.001. ND – not done (parameters were too small for reliable measurements).

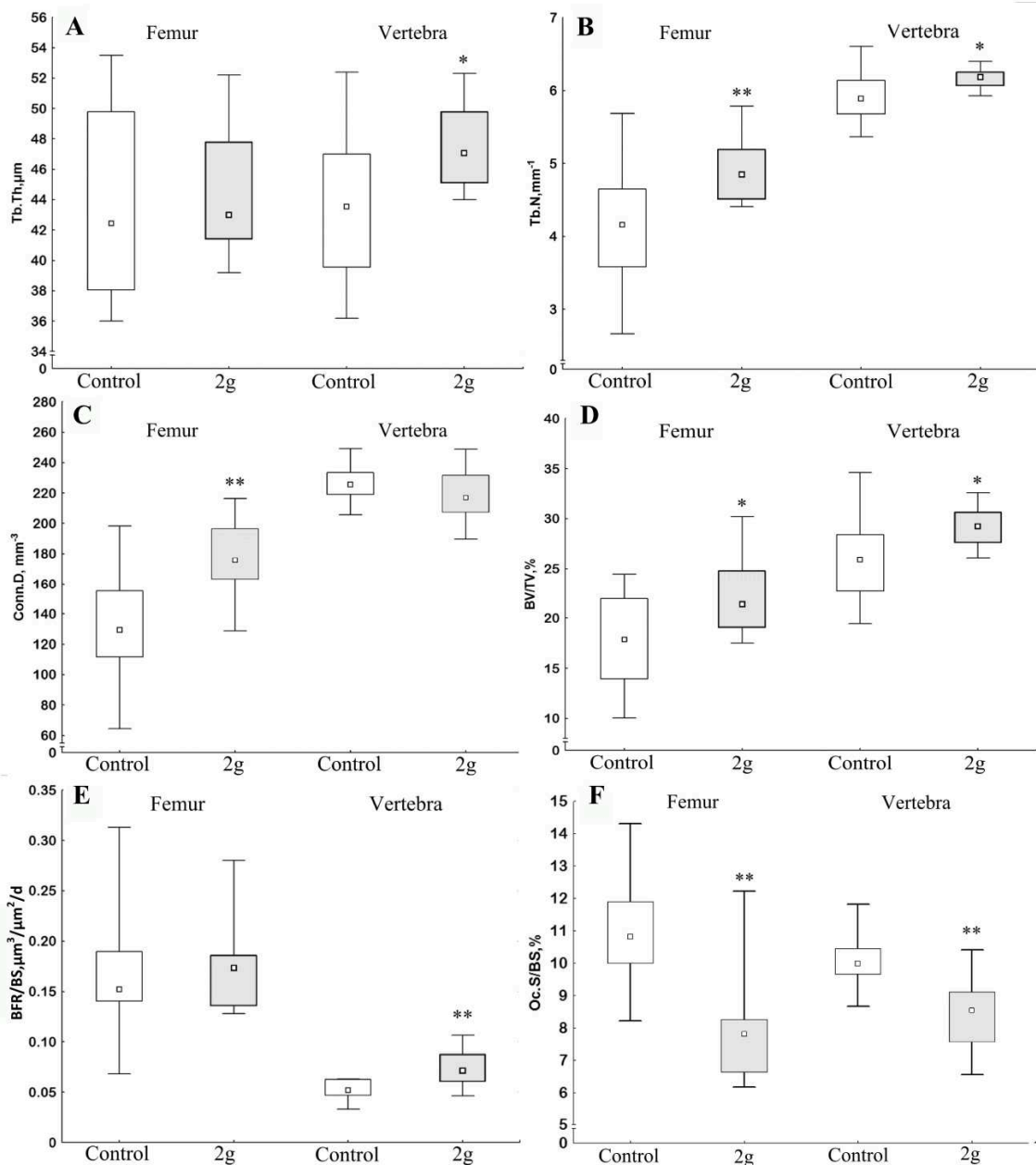


Figure 3. Microarchitecture parameters assessed with μ CT, and histomorphometry analysis in control and 2g centrifugation groups. Femoral distal metaphysis and L2 vertebral body: trabecular thickness (Tb.Th) (A), trabecular number (Tb.N) (B), connectivity density (Conn.D) (C), bone volume over total volume (BV/TV) (D), bone formation rate (BFR/BS) (E), and osteoclasts surface over bone surface (Oc.S/BS) (F). Boxes represent 50% of values (25% to 75%), whiskers represent minimum and maximum values, middle point represents median. Non-parametric Mann-Whitney test, * $p \leq 0.05$, ** $p \leq 0.01$.

Bone vascularization

Exposure to 2g led to an increase of both number of vessels (+22%, $p \leq 0.05$) and their volume (+44%, $p \leq 0.01$) in distal femur secondary spongiosa compared to controls (Table 4).

Table 4. Effects of 21 days 2g centrifugation on vascularization in the femoral distal metaphysis.

Groups	Control	2g centrifugation
Ves.N/Mar.Ar./mm ²	61.6 ± 11.3	74.9 ± 6.8*
Ves.V/Mar.V,%	12.7 ± 3.2	18.3 ± 2.3**

Data are shown as mean ± SD. Non-parametric Mann-Whitney test, 2g compared to control, *p<0.05, **p<0.01.

Circulating Sclerostin immunoassay

When analyzing circulating Sclerostin with the ELISA kit, no difference was found between control group (205 ± 32 pg/ml, n=7) and 2g group (225 ± 24.8 pg/ml, n=7).

Quantitative analysis of immunohistochemical data

No significant differences between groups were detected in osteocyte density, percentage of Sclerostin, or DMP1 positive cells (Table 5). However, the fluorescence intensity (RawIntDens, see chapter Materials and methods) of individual osteocytes showed differences between 2g and controls. In 2g group, osteocyte Sclerostin fluorescence (Fig. 4) was 35% less than in control group (medians: 365 vs 560 respectively, p<0.001). Osteocyte DMP1 fluorescence (Fig. 4) was 60% higher than in controls (medians: 3610 vs 2258 respectively, p<0.001) (Table 5).

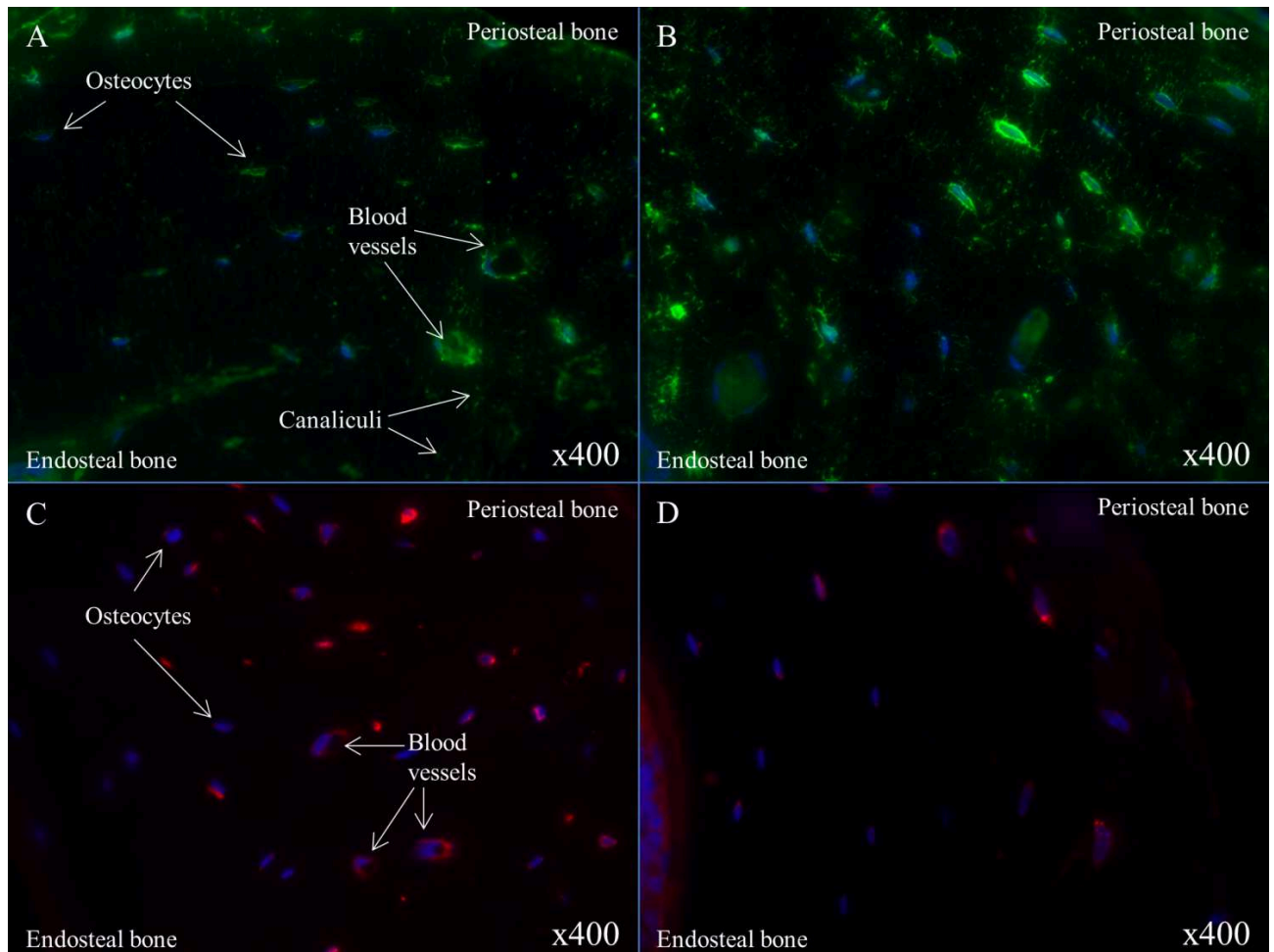


Figure 4. Representative pictures of immunohistochemistry on cortical bone. DAPI (blue) and DMP1 staining (green) of control (A) and 2g experimental (B) groups; DAPI (blue) and Sclerostin (red) staining of control (C) and 2g experimental (D) groups. Blood vessels, bone marrow and collagen are visible due to their natural autofluorescence. Pictures are part of total cortical bone mosaic images, which were used for fluorescence quantitative analysis (chapter materials and methods). Images were equally adjusted for brightness and contrast for demonstrative purposes.

Table 5. Effects of 21 days 2g centrifugation on osteocyte quantitative parameters in femur cortical bone compared to controls.

Groups	Control		2g centrifugation	
Osteocytes density, $1/\mu\text{m}^2$	0.032 ± 0.004		0.034 ± 0.004	
	Sclerostin	DMP1	Sclerostin	DMP1
Positive osteocytes, %	61.8 ± 5.2	87.1 ± 3.4	53.5 ± 5.8	88.7 ± 5.2
RawIntDens per group	560	2258	365***	3610***

Data are shown as mean \pm SD for osteocytes' density (DAPI staining) and percentage of positive cells (immunohistochemistry); as medians for level of fluorescence (RawIntDens, arbitrary unit). Non-parametric Mann-Whitney test, 2g compared to control, *** $p \leq 0.002$.

Discussion

It has been assumed that chronic hypergravity might induce physiological responses, which would be opposite to microgravity effects (5, 18, 62). We found this assumption to be true for 2g. While microgravity led to an increase of bone resorption and decrease of trabecular

BV/TV in rodents (58–60), 2g centrifugation resulted in lower osteoclastic activity and augmented BV/TV in both femur and vertebra. Ikawa et al. (22) reported a bone gain in rats centrifuged at 2.9g. Bojados and Jamon (3) found in male C57Bl6/J mice that hypergravity acted as endurance training on muscle force until 3g, and then became deleterious only at 4g. Thus it could be expected that adaptation to a 3g environment would also lead to improvement of bone tissue. However, in our study μ CT evaluation after exposure to 3g demonstrated a decrease of Ct.Ar and Ct.Th in young mice. In the Ikawa et al. study (22), beside the fact that animals were adult rats, the centrifuge had a 50 cm radius (1.4 m in our study), and much smaller cages which raises concerns that animals may have experienced increased stress due to close confinement; also hypergravity was interrupted daily for 15 minutes. This makes direct comparison difficult.

Even though μ CT demonstrated that femoral and L2 vertebral body trabecular compartments remained the same, histology revealed inhibition of bone formation and stimulation of bone resorption, suggesting that longer exposure to 3g might result in trabecular bone loss. Similarly to other authors (18, 66), we observed body weight loss, which could be a result of low food intake (66) and high stress as indicated by serum corticosterone assay (18). Although infra-red video surveillance was not quantitative, it seemed that the animals' motion activity was lower compared to control suggesting that 3g loading prevented normal locomotor behavior. It can be assumed that potential osteogenic effects of high mechanical loading were counterbalanced by stressful 3g environment. In addition, less movement could result in increase of the static component of mechanical loading, which is known to be deleterious for cortical bone (28). At the same time, muscles strength might benefit from isometric contractions (32). This might explain why at 3g an increase in muscle force was occurring along with bone growth reduction. In contrast to 3g, centrifugation at 2g did not lead to any significant alteration of body weight. Same was previously observed after 21 (18) or 30 (38) days of 2g centrifugation with the same facility, mice and conditions as in present study. In addition, no differences in plasma corticosterone level (18) or adrenal gland weights (38) were found between control and 2g experimental groups.

Longitudinal bone growth can be impaired by high static or dynamic mechanical loading, as it was demonstrated in the rat ulna (45). In contrast to 3g, centrifugation at 2g did not lead to any decrease of longitudinal growth rate, which further indicates that 2g is a safe model.

It is known that microgravity (27) primarily affects trabecular compartment. Interestingly, centrifugation at 2g also altered trabecular bone in the first place, and the weight-bearing bones (femur) were more affected than non-weight-bearing bones (vertebra) in relation to BV/TV and Conn.D parameters. These findings are important as biomechanical properties of bones are highly dependent on trabecular organization (16, 26).

In addition, we observed that 2g modified trabecular microarchitecture in femur and vertebra in different ways. Increase of Tb.Th and Tb.N in vertebra without alteration of Conn.D can be a consequence of adaptation to greater gravitational forces applied along typical loading vector, which animals were exposed to (6, 13, 21, and 41). In contrast to alterations in vertebra, we found no increase of Tb.Th in femoral metaphysis, however we detected an increase of Conn.D. In relation to biomechanical properties, increase of Conn.D is more beneficial than trabeculae thickening (19). Combined with higher Tb.N it results in more uniform mechanical stress distribution (44). Such adaptation suggests that during locomotion at 2g femoral bones experienced specific strain distribution and mechanical forces that were unusually directed. This can be linked to the fact that exposure to 2g modifies gait parameters as it was demonstrated in younger animals (2). At the same time, we detected no effects of 2g continuous hypergravity on the cortical bone, which demonstrates that cortical and trabecular bones respond differently to continuous gravitational challenge.

As we registered changes in trabecular compartments of femur and L2 vertebral body, we analyzed cellular activities there. Exposure to 2g resulted in increased osteoid and mineralized surfaces, presumably due to increase of osteoblast recruitment and/or lifespan. At the same time, MAR decreased in femur, and did not change in vertebra. Similar changes were detected in rats centrifuged at 2.9g for four weeks (lower MAR, BFR/BS, and osteoblast surface), however authors provided little explanations regarding the phenomena of trabecular bone gain along with lower bone formation (22). Our findings suggest that hypergravity might alter individual osteoblast function and mineralization in a transient manner, or that reduction of osteoclastic parameters has played a major role in trabecular bone gain. Future in vitro investigations of osteoblastic cells from centrifuged animal may shed light on the underlying mechanisms. Centrifugation at 2g resulted in notable reduction of osteoclasts' parameters both in weight-bearing and non-weight-bearing bones. It is particularly important for microgravity-related bone loss, as resistive physical exercises cannot reduce high bone resorption level, which has been constantly observed in crewmembers (53).

After 21 days of hypergravity, we observed an increase of bone marrow vascularization (as assessed by vessel number and volume), although the exact underlying mechanism is not known. A link between load-induced bone gain and vascularization has been previously reported (1, 11, 39, 65). Beside in microgravity there is a thoraco-cephalic fluid shift (35), we can also assume that hypergravity induces blood pooling in extremities which might contribute to increased vessel volume. Further, higher capillary density and enhanced microcirculation were reported after «gravitational therapy» with a short-arm centrifuge at 1.5-3Gz, in humans with fractures or osteomyelitis (17).

Mechanical stimulation has been shown to alter osteocyte protein expression. In rodent ulna, axial cycling loading (46) results in a decrease of Sclerostin expression, while in the orthodontic appliance model (15) DMP1 expression is increased. In our study, we observed for the first time similar changes for Sclerostin (-35%) and DMP1 (+60%) expression in osteocytes of the femur diaphysis after an exposure to chronic hypergravity. However, in contrast to axial loading or orthodontic appliance models (15, 46) we did not detect any significant difference in percentage of positive/negative osteocytes (Table 5). This could be explained by the fact that these experimental models vary significantly from ours. It must also be taken into account that while during normal locomotion compressive mechanical strains are about 200-350 $\mu\epsilon$ (43, 54), the models of cycling axial loading provide strains up to 2200 $\mu\epsilon$ (46). Therefore, even assuming that chronic 2g centrifugation provides twice higher strains during locomotion, centrifugation is still a milder challenge for bones, which results in modest but statistically significant alterations of osteocyte protein expressions. It should be noted that decrease of Sclerostin level and low resorption can be linked together as it was shown that Sclerostin affects osteocytes and promotes osteoclastogenesis and osteoclasts activation (63). Moreover, we did not find any changes in serum Sclerostin after 2g centrifugation. These findings imply either that changes in serum Sclerostin levels do not necessarily reflect alterations of Sclerostin production in osteocytes, as it has been shown in ovariectomized mice (25), or that decreased protein expression in femur diaphysis represents a local, and not a generalized effect of 2g exposure.

As there was no alteration of cortical bone after 21 days, we hypothesized that continuous 2g hypergravity affects trabecular bone in the first place, and longer exposure to hypergravity is needed to stimulate cortical bone formation.

This study has the following limitations: 1) there is no data regarding possible increase of bone strength after 2g centrifugation, as no mechanical testing was done; 2) data obtained do not represent dynamics of adaptation processes to hypergravity; 3) we did not study recovery processes after centrifugation; 4) due to stressful conditions of 3g centrifugation, it is difficult to distinguish between effects the stress effects and impact of mechanical loading on bones; 5) no quantitative analysis of food/water intake or animal activity during experiments was presented, as the video surveillance system was not designed for it.

Conclusion

Our main findings are that effects of centrifugation are bone compartment-specific and depend on the gravity level; and that centrifugation at 2g appeared to be a safe model for young animals in relation to bone and body growth. Centrifugation at 2g brought down osteoclastic resorption and local Sclerostin expression. It stimulated osteoid deposition and angiogenesis, and increased DMP1 level. Thus, centrifuge is a promising platform for investigating bone mechanosensitivity and gravity-related alterations. In our study we argue that further research investigating the bone metabolism dynamics is needed to define optimal level and duration of hypergravity; and that future experiments can be performed in combination with bone loss animal models, to assess protective or/and regenerative effects of hypergravity.

Acknowledgments

We acknowledge G. Gauquelin-Koch from CNES and M. Jamon (INSERM U1106, Marseille) for their help with the hypergravity facility, and the staff of the animal facility PLEXAN of the University of Saint-Etienne. We thank K. de Rooij and M. van der Velde from Leiden University Medical Centre for the assistance with IHC techniques. We are also grateful to M. Goubier, C. Hunot, F. Louis and W. Boulefour for their technical assistance.

Grants

We acknowledge financial support from the French National Space Agency (CNES) (Program 'Microgravity and Development'), the 'Agence Nationale de la Recherche' ANR-09-BLAN-0148 (AdapHyG), and INSERM (Institut National de la Santé et de la Recherche Médicale). V. Gnyubkin has received a scholarship from the French Ministry of Higher Education and Research.

Author contributions

Study design: LV, VG, MHLP. Study conduct and data collection: VG, AG, NL and AVB. Data analysis: VG and AG. Statistical analysis: MN. Data interpretation: VG and LV. Drafting manuscript: VG and LV. Revised manuscript content: MHLP. Approval of final manuscript: VG, AG, NL, AVB, MN, MHLP and LV. LV supervised the overall study.

References

1. **Barou O, Mekraldi S, Vico L, Boivin G, Alexandre C, Lafage-Proust MH.** Relationships between trabecular bone remodeling and bone vascularization: a quantitative study. *Bone* 30: 604–612, 2002.
2. **Bojados M, Herbin M, Jamon M.** Kinematics of treadmill locomotion in mice raised in hypergravity. *Behav Brain Res* 244: 48–57, 2013.
3. **Bojados M, Jamon M.** The long-term consequences of the exposure to increasing gravity levels on the muscular, vestibular and cognitive functions in adult mice. *Behav Brain Res* 264: 64–73, 2014.
4. **Bonewald LF.** Osteocytes as dynamic multifunctional cells. *Ann N Y Acad Sci* 1116: 281–290, 2007.
5. **Burton RR, Smith AH.** Can centrifugation at increased G be used to predict results of 0G? *J Gravitational Physiol* 6: P1–4, 1999.
6. **Ciarelli TE, Fyhrie DP, Schaffler MB, Goldstein SA.** Variations in three-dimensional cancellous bone architecture of the proximal femur in female hip fractures and in controls. *J Bone Miner Res* 15: 32–40, 2000.
7. **Clément G, Pavy-Le Traon A.** Centrifugation as a countermeasure during actual and simulated microgravity: a review. *Eur J Appl Physiol* 92: 235–248, 2004.
8. **Crawford-Young SJ.** Effects of microgravity on cell cytoskeleton and embryogenesis. *Int J Dev Biol* 50: 183–191, 2006.
9. **David V, Lafage-Proust M-H, Laroche N, Christian A, Ruegsegger P, Vico L.** Two-week longitudinal survey of bone architecture alteration in the hindlimb-unloaded rat model of bone loss: sex differences. *Am J Physiol Endocrinol Metab* 290: E440–447, 2006.
10. **David V, Laroche N, Boudignon B, Lafage-Proust M-H, Alexandre C, Ruegsegger P, Vico L.** Noninvasive in vivo monitoring of bone architecture alterations in hindlimb-unloaded female rats using novel three-dimensional microcomputed tomography. *J Bone Miner Res* 18: 1622–1631, 2003.

11. **Fei J, Jia F, Peyrin F, Françoise P, Malaval L, Vico L, Laurence V, Lafage-Proust M-H, Marie-Hélène L-P.** Imaging and quantitative assessment of long bone vascularization in the adult rat using microcomputed tomography. *Anat Rec* 2007 293: 215–224, 2010.
12. **Feng JQ, Ward LM, Liu S, Lu Y, Xie Y, Yuan B, Yu X, Rauch F, Davis SI, Zhang S, Rios H, Drezner MK, Quarles LD, Bonewald LF, White KE.** Loss of DMP1 causes rickets and osteomalacia and identifies a role for osteocytes in mineral metabolism. *Nat Genet* 38: 1310–1315, 2006.
13. **Frost HM.** On the trabecular “thickness”-number problem. *J Bone Miner Res* 14: 1816–1821, 1999.
14. **Gerdes MJ, Sevinsky CJ, Sood A, Adak S, Bello MO, Bordwell A, Can A, Corwin A, Dinn S, Filkins RJ, Hollman D, Kamath V, Kaanumalle S, Kenny K, Larsen M, Lazare M, Li Q, Lowes C, McCulloch CC, McDonough E, Montalto MC, Pang Z, Rittscher J, Santamaria-Pang A, Sarachan BD, Seel ML, Seppo A, Shaikh K, Sui Y, Zhang J, Ginty F.** Highly multiplexed single-cell analysis of formalin-fixed, paraffin-embedded cancer tissue. *Proc Natl Acad Sci* 110: 11982–11987, 2013.
15. **Gluhak-Heinrich J, Ye L, Bonewald LF, Feng JQ, MacDougall M, Harris SE, Pavlin D.** Mechanical Loading Stimulates Dentin Matrix Protein 1 (DMP1) Expression in Osteocytes In Vivo. *J Bone Miner Res* 18: 807–817, 2003.
16. **Goulet RW, Goldstein SA, Ciarelli MJ, Kuhn JL, Brown MB, Feldkamp LA.** The relationship between the structural and orthogonal compressive properties of trabecular bone. *J Biomech* 27: 375–389, 1994.
17. **Kotelnikov G. P, Sonis A.G.** Influence of gravitational therapy on reparative osteogenesis in patients with osteomyelitis of lower extremities. *Saratov J Med Sci Res*, 2010.
18. **Guéguinou N, Bojados M, Jamon M, Derradji H, Baatout S, Tschirhart E, Fripiat J-P, Legrand-Frossi C.** Stress response and humoral immune system alterations related to chronic hypergravity in mice. *Psychoneuroendocrinology* 37: 137–147, 2012.
19. **Guo XE, Kim CH.** Mechanical consequence of trabecular bone loss and its treatment: a three-dimensional model simulation. *Bone* 30: 404–411, 2002.
20. **Harris SE, Gluhak-Heinrich J, Harris MA, Yang W, Bonewald LF, Riha D, Rowe PSN, Robling AG, Turner CH, Feng JQ, McKee MD, Nicollela D.** DMP1 and MEPE expression are elevated in osteocytes after mechanical loading in vivo: theoretical role in controlling mineral quality in the perilacunar matrix. *J Musculoskelet Neuronal Interact* 7: 313–315, 2007.
21. **Homminga J, McCreadie BR, Ciarelli TE, Weinans H, Goldstein SA, Huiskes R.** Cancellous bone mechanical properties from normals and patients with hip fractures differ on the structure level, not on the bone hard tissue level. *Bone* 30: 759–764, 2002.

22. **Ikawa T, Kawaguchi A, Okabe T, Ninomiya T, Nakamichi Y, Nakamura M, Uehara S, Nakamura H, Udagawa N, Takahashi N, Nakamura H, Wakitani S.** Hypergravity suppresses bone resorption in ovariectomized rats. *Adv Space Res* 47: 1214–1224, 2011.
23. **Iwase S, Takada H, Watanabe Y, Ishida K, Akima H, Katayama K, Iwase M, Hirayanagi K, Shiozawa T, Hamaoka T, Masuo Y, Custaud M-A.** Effect of centrifuge-induced artificial gravity and ergometric exercise on cardiovascular deconditioning, myatrophy, and osteoporosis induced by a -6 degrees head-down bedrest. *J Gravitational Physiol* 11: P243–244, 2004.
24. **Jamon M, Serradj N.** Ground-Based Researches on the Effects of Altered Gravity on Mice Development. *Microgravity Sci Technol* 21: 327–337, 2009.
25. **Jastrzebski S, Kalinowski J, Stolina M, Mirza F, Torreggiani E, Kalajzic I, Won HY, Lee S-K, Lorenzo J.** Changes in bone sclerostin levels in mice after ovariectomy vary independently of changes in serum sclerostin levels. *J Bone Miner Res* 28: 618–626, 2013.
26. **Kleerekoper M, Villanueva AR, Stanciu J, Rao DS, Parfitt AM.** The role of three-dimensional trabecular microstructure in the pathogenesis of vertebral compression fractures. *Calcif Tissue Int* 37: 594–597, 1985.
27. **Lang T, LeBlanc A, Evans H, Lu Y, Genant H, Yu A.** Cortical and trabecular bone mineral loss from the spine and hip in long-duration spaceflight. *J Bone Miner Res* 19: 1006–1012, 2004.
28. **Lanyon LE, Rubin CT.** Static vs dynamic loads as an influence on bone remodelling. *J Biomech* 17: 897–905, 1984.
29. **LeBlanc A, Schneider V, Shackelford L, West S, Oganov V, Bakulin A, Voronin L.** Bone mineral and lean tissue loss after long duration space flight. *J Musculoskeletal Neuronal Interact* 1: 157–160, 2000.
30. **LeBlanc A, Shackelford L, Schneider V.** Future human bone research in space. *Bone* 22: 113S–116S, 1998.
31. **Lin C, Jiang X, Dai Z, Guo X, Weng T, Wang J, Li Y, Feng G, Gao X, He L.** Sclerostin mediates bone response to mechanical unloading through antagonizing Wnt/beta-catenin signaling. *J Bone Miner Res* 24: 1651–1661, 2009.
32. **Lindh M.** Increase of muscle strength from isometric quadriceps exercises at different knee angles. *Scand J Rehabil Med* 11: 33–36, 1979.
33. **Ling Y, Rios HF, Myers ER, Lu Y, Feng JQ, Boskey AL.** DMP1 depletion decreases bone mineralization in vivo: an FTIR imaging analysis. *J Bone Miner Res* 20: 2169–2177, 2005.
34. **Li X, Zhang Y, Kang H, Liu W, Liu P, Zhang J, Harris SE, Wu D.** Sclerostin binds to LRP5/6 and antagonizes canonical Wnt signaling. *J Biol Chem* 280: 19883–19887, 2005.

35. **Maciejewska I, Qin D, Huang B, Sun Y, Mues G, Svoboda K, Bonewald L, Butler WT, Feng JQ, Qin C.** Distinct compartmentalization of dentin matrix protein 1 fragments in mineralized tissues and cells. *Cells Tissues Organs* 189: 186–191, 2009.
36. **McCarthy ID.** Fluid shifts due to microgravity and their effects on bone: a review of current knowledge. *Ann Biomed Eng* 33: 95–103, 2005.
37. **Naumann FL, Bennell KL, Wark JD.** The effects of +Gz force on the bone mineral density of fighter pilots. *Aviat Space Environ Med* 72: 177–181, 2001.
38. **Naumann FL, Grant MC, Dhaliwal SS.** Changes in cervical spine bone mineral density in response to flight training. *Aviat Space Environ Med* 75: 255–259, 2004.
39. **Ogneva IV, Gnyubkin V, Laroche N, Maximova MV, Larina IM, Vico L.** Structure of the cortical cytoskeleton in fibers of postural muscles and cardiomyocytes of mice after 30-day 2-g centrifugation. *J Appl Physiol* 118: 613–623, 2015.
40. **Oshima M, Suzuki H, Guo X, Oshima H.** Increased level of serum vascular endothelial growth factor by long-term exposure to hypergravity. *Exp Anim* 56: 309–313, 2007.
41. **Oyama J.** Response and adaptation of beagle dogs to hypergravity. *Life Sci Space Res* 13: 11–17, 1975.
42. **Parfitt AM, Mathews CH, Villanueva AR, Kleerekoper M, Frame B, Rao DS.** Relationships between surface, volume, and thickness of iliac trabecular bone in aging and in osteoporosis. Implications for the microanatomic and cellular mechanisms of bone loss. *J Clin Invest* 72: 1396–1409, 1983.
43. **Phillips RW.** Gravity: It's the law. *J Gravitational Physiol* 9: P15–16, 2002.
44. **Prasad J, Wiater BP, Nork SE, Bain SD, Gross TS.** Characterizing gait induced normal strains in a murine tibia cortical bone defect model. *J Biomech* 43: 2765–2770, 2010.
45. **Van Rietbergen B, Huiskes R, Eckstein F, Rügsegger P.** Trabecular bone tissue strains in the healthy and osteoporotic human femur. *J Bone Miner Res* 18: 1781–1788, 2003.
46. **Robling AG, Duijvelaar KM, Geevers JV, Ohashi N, Turner CH.** Modulation of appositional and longitudinal bone growth in the rat ulna by applied static and dynamic force. *Bone* 29: 105–113, 2001.
47. **Robling AG, Niziolek PJ, Baldridge LA, Condon KW, Allen MR, Alam I, Mantila SM, Gluhak-Heinrich J, Bellido TM, Harris SE, Turner CH.** Mechanical stimulation of bone in vivo reduces osteocyte expression of Sost/sclerostin. *J Biol Chem* 283: 5866–5875, 2008.
48. **Roche B, David V, Vanden-Bossche A, Peyrin F, Malaval L, Vico L, Lafage-Proust M-H.** Structure and quantification of microvascularisation within mouse long bones:

- what and how should we measure? *Bone* 50: 390–399, 2012.
49. **Rubin CT, Bain SD, McLeod KJ.** Suppression of the osteogenic response in the aging skeleton. *Calcif Tissue Int* 50: 306–313, 1992.
 50. **Sibonga JD.** Spaceflight-induced bone loss: is there an osteoporosis risk? *Curr Osteoporos Rep* 11: 92–98, 2013.
 51. **Sibonga JD, Evans HJ, Sung HG, Spector ER, Lang TF, Oganov VS, Bakulin AV, Shackelford LC, LeBlanc AD.** Recovery of spaceflight-induced bone loss: bone mineral density after long-duration missions as fitted with an exponential function. *Bone* 41: 973–978, 2007.
 52. **Smith SM, Heer MA, Shackelford LC, Sibonga JD, Ploutz-Snyder L, Zwart SR.** Benefits for bone from resistance exercise and nutrition in long-duration spaceflight: Evidence from biochemistry and densitometry. *J Bone Miner Res* 27: 1896–1906, 2012.
 53. **Smith SM, Zwart SR, Heer MA, Baecker N, Evans HJ, Feiveson AH, Shackelford LC, LeBlanc AD.** Effects of artificial gravity during bed rest on bone metabolism in humans. *J Appl Physiol* 107: 47–53, 2009.
 54. **Smith SM, Zwart SR, Heer M, Hudson EK, Shackelford L, Morgan JL.** Men and women in space: bone loss and kidney stone risk after long-duration spaceflight. *J Bone Miner Res* 29: 1639–1645, 2014.
 55. **De Souza RL, Matsuura M, Eckstein F, Rawlinson SCF, Lanyon LE, Pitsillides AA.** Non-invasive axial loading of mouse tibiae increases cortical bone formation and modifies trabecular organization: A new model to study cortical and cancellous compartments in a single loaded element. *Bone* 37: 810–818, 2005.
 56. **Srinivasan S, Agans SC, King KA, Moy NY, Poliachik SL, Gross TS.** Enabling bone formation in the aged skeleton via rest-inserted mechanical loading. *Bone* 33: 946–955, 2003.
 57. **Turner CH, Takano Y, Owan I.** Aging changes mechanical loading thresholds for bone formation in rats. *J Bone Miner Res* 10: 1544–1549, 1995.
 58. **Vico L, Barou O, Laroche N, Alexandre C, Lafage-Proust MH.** Effects of centrifuging at 2g on rat long bone metaphyses. *Eur J Appl Physiol* 80: 360–366, 1999.
 59. **Vico L, Bourrin S, Genty C, Palle S, Alexandre C.** Histomorphometric analyses of cancellous bone from COSMOS 2044 rats. *J Appl Physiol Bethesda Md* 1985 75: 2203–2208, 1993.
 60. **Vico L, Chappard D, Alexandre C, Palle S, Minaire P, Riffat G, Novikov VE, Bakulin AV.** Effects of weightlessness on bone mass and osteoclast number in pregnant rats after a five-day spaceflight (COSMOS 1514). *Bone* 8: 95–103, 1987.
 61. **Vico L, Chappard D, Palle S, Bakulin AV, Novikov VE, Alexandre C.** Trabecular bone remodeling after seven days of weightlessness exposure (BIOCOSMOS 1667). *Am*

J Physiol 255: R243–247, 1988.

62. **Vico L, Collet P, Guignandon A, Lafage-Proust M-H, Thomas T, Rehalia M, Alexandre C.** Effects of long-term microgravity exposure on cancellous and cortical weight-bearing bones of cosmonauts. *The Lancet* 355: 1607–1611, 2000.
63. **Wade CE.** Responses across the gravity continuum: hypergravity to microgravity. *Adv Space Biol Med* 10: 225–245, 2005.
64. **Wijenayaka AR, Kogawa M, Lim HP, Bonewald LF, Findlay DM, Atkins GJ.** Sclerostin Stimulates Osteocyte Support of Osteoclast Activity by a RANKL-Dependent Pathway. *PLoS ONE* 6: e25900, 2011.
65. **Williams D, Kuipers A, Mukai C, Thirsk R.** Acclimation during space flight: effects on human physiology. *CMAJ* 180: 1317–1323, 2009.
66. **Yao Z, Lafage-Proust M-H, Plouët J, Bloomfield S, Alexandre C, Vico L.** Increase of both angiogenesis and bone mass in response to exercise depends on VEGF. *J Bone Miner Res* 19: 1471–1480, 2004.
67. **Yuwaki K, Okuno M.** Changes in food intake and growth rate in mice under hypergravity. *Biol Sci Space* 17: 219–220, 2003.
68. **Zhang L-F, Sun B, Cao X-S, Liu C, Yu Z-B, Zhang L-N, Cheng J-H, Wu Y-H, Wu X-Y.** Effectiveness of intermittent -Gx gravitation in preventing deconditioning due to simulated microgravity. *J Appl Physiol Bethesda Md* 1985 95: 207–218, 2003.

Supporting information

S1 video. Centrifuge rotating at 2g.

Conclusion/perspectives

We demonstrated that centrifugation decreased resorption parameters and resulted in trabecular bone gain in both weight-bearing and non-weight-bearing bones. Notably, trabecular re-organization was site-specific and differed in femur and vertebra, presumably due to particular vector of acceleration force. Interestingly, decrease of Sclerostin expression and increase of DMP1 did not result in any detectable mass-structural alterations of cortical bone, however we assumed that longer exposure to 2g might trigger cortical bone growth.

Perspective studies may investigate the ability of hypergravity to prevent a bone loss. Considering technical difficulties of placing a centrifuge in space, effects of hypergravity on recovery processes after microgravity can be studied. Additionally, effects of short-time (minutes to hours) exposure to hypergravity should be addressed in future studies as more applicable for humans.

3.2 Skeleton adaptation to intermittent hypergravity

3.2.1 Introduction to the paper

In the WBV study, we used the same acceleration (2g) and the same experiment duration (21 days) as in continuous hypergravity experiment. We were aiming to (a) establish a whole body vibration regimen, which promotes bone gain in healthy animals, and (b) investigate effects of intermittent hypergravity produced by WBV on mice of the same type and age as were used in continuous hypergravity experiment. The vibration frequency of 90Hz was selected based on results of WBV study performed by our team, which showed that vibration at 90Hz was the most beneficial for healthy rats [86].

The use of young animals allowed us to verify that WBV applied during the period of active skeletal growth accelerates an acquisition of the peak bone mass and/or further increases it and that WBV at a high acceleration does not impair bone growth or the increase in body weight.

In the non-published part of the experiment, we investigated whether long-term (9-week) low-acceleration WBV at 0.5g would trigger bone gain in healthy animals, as the most of published papers demonstrated no beneficial effect on bone structural parameters from WBV at acceleration $\geq 1g$. Additionally, we had a concern about safety of a long-term WBV at 2g, thus we introduced a group which received WBV at gradually increasing acceleration from 0.5g to 2g over the period of the experiment. Also, we wanted to test if such progressive loading is more beneficial for bones than the constant one.

3.2.2 Paper #2: “High-acceleration Whole Body Vibration stimulates cortical bone accrual and increases bone mineral content in growing mice”

Vasily Gnyubkin^a, Alain Guignandon^a, Norbert Laroche^a, Arnaud Vanden-Bossche^a, Luc Malaval^a, Laurence Vico^a

^a INSERM U1059, Laboratoire de Biologie intégrative du Tissu Osseux, Université de Lyon, 42023 Saint-Etienne, France.

Corresponding author: Laurence Vico

INSERM U1059, LBTO

Address: 10 Chemin de la Marandière, Faculty of Medicine, St-Priest en Jarez, 42270, France

Phone: +33 4 77 42 14 23

Email : vico@univ-st-etienne.fr

Abstract

Whole body vibration (WBV) is a promising tool for counteracting bone loss. Most WBV studies on animals have been performed at acceleration < 1g and frequency between 30 and 90Hz. Such WBV conditions trigger bone growth in osteopenia models, but not in healthy animals. In order to test an ability of WBV to promote osteogenesis in young animals, we exposed seven-week-old male mice to vibration at 90Hz, 2g peak acceleration for 15 min/day, 5 days/week. We examined the effects on skeletal tissues with micro-computed tomography and histology. We also quantified bone vascularization and mechanosensitive osteocyte proteins, Sclerostin and DMP1. Three weeks of WBV resulted in an increase of femur cortical thickness (+5%) and area (+6%), associated with a 25% decrease of Sclerostin expression, and 35% increase of DMP1 expression in cortical osteocytes. Mass-structural parameters of trabecular bone were unaltered in femur or vertebra, while osteoclastic parameters and bone formation rate were increased at both sites. Three weeks of WBV resulted in higher blood vessel numbers (+23%) in the femoral metaphysis.

After 9-week of WBV, we have not observed difference in structural cortical or trabecular parameters. However, the tissue mineral density of cortical bone was increased by 2.5%.

Three or nine weeks of 2g/90Hz WBV treatment did not affect longitudinal growth rate or body weight increase under our experimental conditions, indicating that these are safe to use.

These results validate a potential of 2g/90Hz WBV to stimulate trabecular bone cellular activity, cortical bone growth, and peak bone mass acquisition.

Keywords: Osteocytes, Sclerostin, DMP1, μ CT, Immunohistochemistry, Bone vascularization.

Introduction

Bones are constantly adapting to mechanical loading, and therefore appropriate mechanical stimulation could be used to counteract bone loss inducing factors [1,2]. Bone adaptation

processes depend on the intensity of loading and the number of loading cycles [3]. Whole body vibration (WBV) can be an addition or even an alternative to physical exercise, as it produces thousands of low-impact strain events in a relatively short period of time with no significant efforts from a recipient, making it promising for individuals with impaired mobility or attenuated muscle strength.

A pioneer study performed by Rubin et al. (2001) showed that one year of a 30Hz vibration at 0.3g leads to a 30% increase of the trabecular bone volume and density, as well as bone strength and stiffness in sheep [4]. Even though in recent years there have been numerous WBV studies on both animals and humans, it is still difficult, due to high variability of experimental procedures, to decide which WBV protocol is the most beneficial for bones [5]. Among published WBV animal studies, acceleration ranges between 0.3g and 3g ($1g = 9.81m/s^2$) [6], and frequencies between 8 and 90Hz [7,8]. The studies also vary in duration of exposure and resting times [9,10], choice of studied species (rat, mouse, sheep), and age of the animals [6,11,12]. In spite of various possible combinations, most of the WBV studies have been done with magnitudes below 1g, and frequencies from 30 to 50Hz on physiologically challenged (ovariectomized, unloaded, or immobilized) animals. This has been done in order to test WBV ability to prevent an induced bone loss. Notably, the low-magnitude WBV had mostly beneficial effects on osteopenic models, but did not promote bone accrual in control animals.

The effects of high-acceleration (above 1g) WBV have not been much investigated yet. It could be expected that higher acceleration would result in higher strain, and therefore in bone formation [13], even in healthy animals. However, despite the high g-level, WBV at 2g/50Hz and 3g/30Hz appeared osteogenic for ovariectomized animals but not for controls [6,14]. Such results were presumably informed by suboptimal frequencies. A comparison of WBV frequencies (8Hz, 52Hz and 90Hz) with the same acceleration (0.7g) revealed that only a frequency of 90Hz stimulated bone formation in healthy rats [7].

In a present study, our goal was to establish a WBV regimen, which promotes bone gain in healthy animals. We hypothesized that, due to an interrelationship between loading cycles and bone adaptation [13], a combination of 90Hz frequency and high acceleration (2g) would efficiently stimulate bone growth in healthy mice. Young animals were chosen to verify that (a) WBV applied during the period of active skeletal growth accelerates an acquisition of the

peak bone mass and/or further increases it and (b) WBV at a high acceleration does not impair bone growth or the increase in body weight.

We showed that a high acceleration WBV regimen increases mouse bone cellular activity, accelerates cortical bone size acquisition and, in the long run (9 weeks), results in a net increase in bone matrix mineral content.

Materials and Methods

Care for animals

Seven-week-old C57BL/6J male mice (Charles River Laboratories, l'Arbresle, France) were housed in the PLEXAN facility (Platform for Experiments and Analysis, Faculty of Medicine, University of Saint-Etienne, France). The procedures for the animal care were done in accordance with the European Community Standards (Ministère de l'Agriculture, France, Authorization 04827). All animal experiments were approved by the local ethical committee (Comité d'Ethique en Expérimentation Animale de la Loire CEEAL-UJM, agreement n° 98) and the Animal Welfare Committee of the PLEXAN. Mice were kept at a standard temperature ($23\pm 2^{\circ}\text{C}$), in a light controlled environment (12h light/12h dark cycle). Mice were housed by four in standard cages (36x20x14cm) with bedding material, in a quiet room with constant temperature ($23\pm 2^{\circ}\text{C}$) with 50% relative humidity, in a light controlled environment (12h light/12h dark cycle). Food and water were provided ad libitum (Safe diets A04, Augy, France). The light/dark cycle was inverted so that WBV sessions were performed during the active day phase in a dark quiet room.

Material set-up

Shakers (TIRA TV 52120) with attached aluminum table (30 cm diameter, 4 mm thickness) were used to generate vibrations (Fig. 1a). The g-level was controlled by an accelerometer (PBB Piezotronics, 100 mV/g, ref 352C33) glued under the table at midradius distance. During each WBV session, four mice from the same cage were put on the table and left free to move. WBV was applied 15 min/day, 5 days/week, at 90Hz frequency (sinusoidal signal) for 3 or 9 weeks. To avoid potential stress, the peak acceleration level was gradually increased from 0.5g to 2g within the first week of the experiment. Mice in the control group were put for the same duration/day on an inactive shaker for a sham-WBV.

Experimental design

The experimental design is summarized in Fig. 1b. A total of 58 animals were distributed as follows: 10 animals in basal control group euthanized at the beginning, 32 mice in the three weeks experiment randomly divided in control and experimental groups (n=16/group). At the end-point, 8 animals from each group were processed for microcomputed tomography (μ CT), histomorphometry, and immunohistochemistry (IHC) analysis. The other 8 were perfused with barium sulfate for bone vascular imaging. For the nine weeks experiment, 16 mice were randomly divided in control and experimental groups (n=8/group) and processed at the end-point for μ CT and histomorphometry.

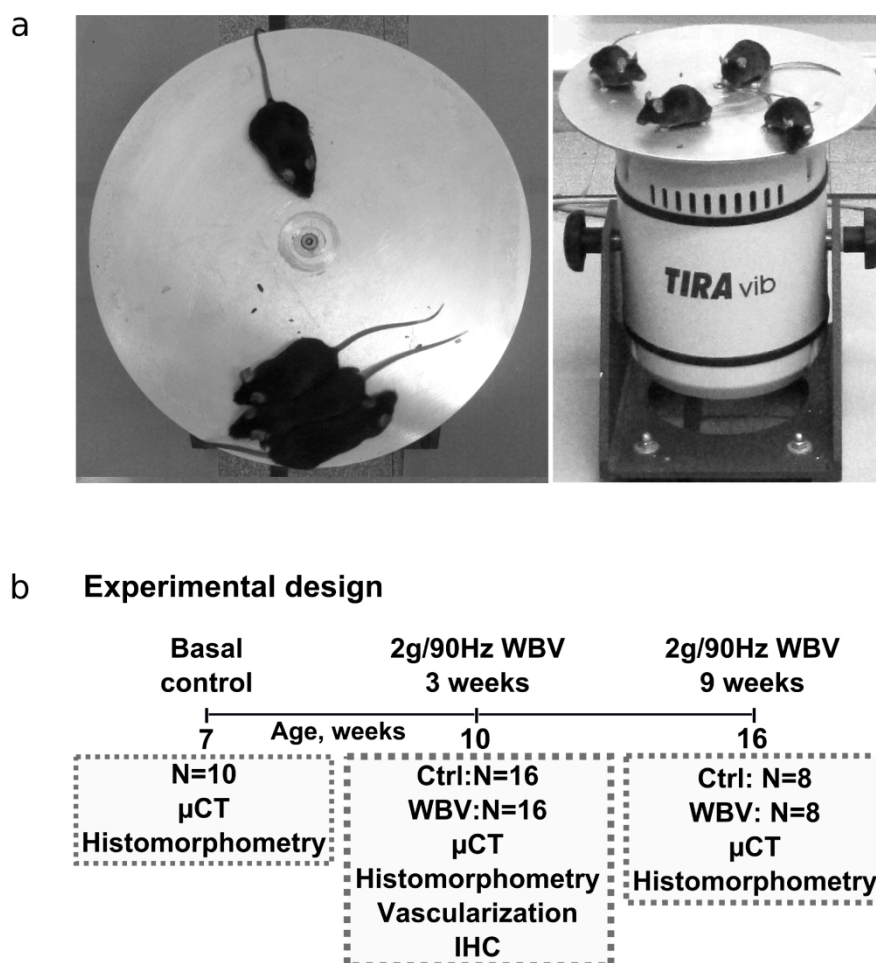


Figure 1. Vibration device and a scheme of the experimental design. a – descriptive photo of the vibration device during a vibration session; b - scheme of the experimental design, number of animals and performed analyses are listed for each group/experiment. Ctrl = control, WBV = whole body vibration.

Microtomography

Formalin fixed and ethanol-dehydrated femur and L2 vertebral body were scanned with a high-resolution μ CT (Viva CT 40; Scanco Medical, Switzerland). Data were acquired at 55keV energy, with 145 μ A current for 10 μ m cubic resolution. The distal right femur was scanned through 4.1mm starting from the growth plate (Fig.2a). The L2 vertebra was scanned entirely (Fig.2e). Three-dimensional reconstructions were generated with the following parameters: Sigma, 1.2; Support, 2; Threshold, 160 (spongiosa) or 280 (cortex). In the femur distal metaphysis the ROI was restricted to the trabecular area (Fig.2b, 2c). The cortical area was assessed at diaphysis (Fig.2d). In the vertebral body, the trabecular bone was assessed between the two growth plates (Fig.2f, 2g). Tissue Mineral Density (TMD, mg/cm³), cortical thickness (Ct.Th, mm), and cortical area (Ct.Ar, mm²) were measured in the cortical bone. In trabecular bone, we measured bone volume/trabecular volume (BV/TV, %), trabecular separation (Tb.Sp, μ m), trabecular thickness (Tb.Th, μ m), trabecular number (Tb.N, mm⁻¹), connectivity density (Conn.D, mm⁻³), structure model index (SMI), and the degree of anisotropy (DA).

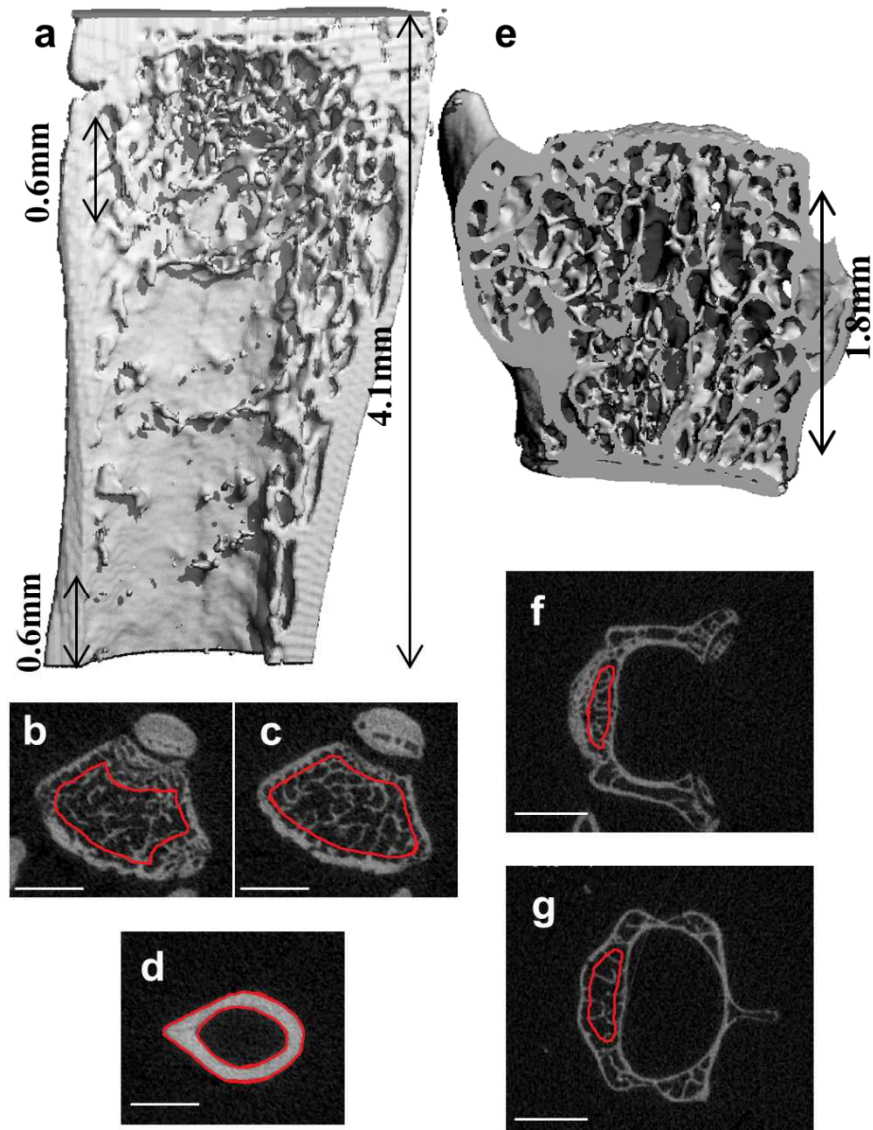


Figure 2. Locations of the Regions Of Interest for μ CT analysis of trabecular and cortical bones. Mice femur, scanned area of 4.1 mm height (a), manual selection of region of interest for analysis on distal metaphysis (0.6 mm, 60 successive sections) starting below the primary spongiosa (b), up to the middle of the secondary spongiosa (c), and in the diaphysis (0.6 mm, 60 successive sections) (d); L2 vertebral body, scanned area (e), manual selection of region of interest (1.8 mm, 180 sections) for analysis from primary spongiosa (f), and including entire secondary spongiosa (g).

Histomorphometry

Six and two days before euthanasia, the mice were injected intraperitoneally with 200 μ l of a 0.37% tetracycline solution. After μ CT analysis, femur metaphysis and the L2 vertebra were embedded undecalcified in methylmethacrylate and processed for histomorphometry as previously described [15]. Bone cellular parameters were measured in the secondary spongiosa with a digitizing tablet (Summasketch; Summagraphics, Paris, France) and software designed in our laboratory [15]. In brief, we measured osteoid surfaces (OS/BS, %),

surfaces double labeled with tetracycline (dLS/BS, %) and mineral apposition rate (MAR, $\mu\text{m}/\text{day}$), from which the bone formation rate (BFR/BS, $\mu\text{m}^3/\mu\text{m}^2/\text{day}$) was calculated. Osteoclast surfaces (Oc.S/BS,%) were assessed through tartrate-resistant acid phosphatase (TRAP) labeling of osteoclast. In the primary spongiosa of the femur, a longitudinal growth rate (LGR, $\mu\text{m}/\text{day}$) was determined through tetracycline labeling by measuring the distance in $\mu\text{m}/\text{day}$ between the two fluorochrome labelings (parallel to the growth plate) in the primary spongiosa.

In the cortical bone, we assessed endosteal MAR, however, due to bone scraping during dissection it was not possible to reliably measure periosteal bone formation.

Bone vessel imaging and quantification

Vascular imaging was done as previously described by Roche et al [16]. In brief, euthanized mice received an intracardiac perfusion of BaSO₄ solution (Micropaque Guerbet, Paris, France). Femurs were embedded in Neg50 (Thermo Scientific, Ref. 6502) by snap-freezing in liquid nitrogen. Nine μm -thick longitudinal sections (Fig.3) of a whole bone were cut with $27\mu\text{m}$ increments with a cryotome (Microm HM 525, Thermo Scientific). Results are expressed as Vessel Number/ mm^2 of Marrow Area (Ves.N/Mar.Ar) and Vessel Volume/Marrow Volume (Ves.V/Mar.V), as described in [16].

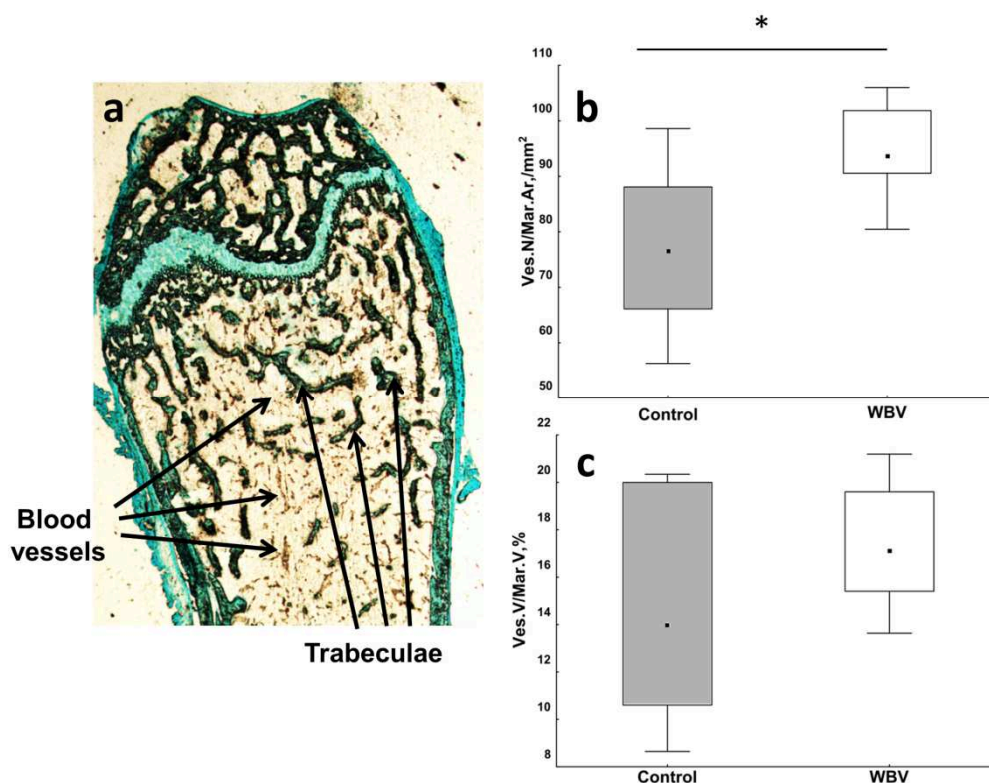


Figure 3. Effects of 3-week whole body vibration on distal femur metaphysis vascularization. Cryosection (9µm-thick) of a mice femur perfused with barium sulfate (a); vessels number over bone marrow area (b); vessel volume over bone marrow volume (c). Control = age-matched control, WBV = whole body vibration. Boxes represent 50% of values (25% to 75%), whiskers represent minimum and maximum values, middle point represents median. Non-parametric Mann-Whitney U-test, *p<0.05.

Quantitative immunohistochemistry

We used fluorescent IHC as in [17] to perform semi-automatic quantitative analysis of proteins expression level. Femurs were fixed in 10% neutral buffered formalin and then in 70% ethanol. Three mm long sections of the mid-diaphysis (5 and 8 mm from the distal epiphysis) were cut out with a precision diamond wire saw (ESCIL Well, France), decalcified for 24 hours (Immunocal, Decal Chemical Corp., Ref 1440), and embedded in paraffin. Five µm thick transversal sections of the diaphysis, separated by 250 µm, were cut from the distal part of the sample with a Leica RM2245 microtome and immunolabeled for Sclerostin (Primary antibody: polyclonal, goat, R&D Systems, AF1589, 1:400), and DMP1 (dentin matrix acidic phosphoprotein 1, Primary antibody: polyclonal, rabbit, Takara, M176, 1:500). Sclerostin was detected using a biotinylated secondary polyclonal rabbit anti-goat antibody (Dako, E0466) and Streptavidin-Alexa Fluor (Life technologies, S 11225, 1:500). DMP1 was detected using a biotin-free ready-to-use PowerFluor immunofluorescence detection kit (MaxVision Biosciences, PF 21-M). Cell nuclei were visualized with DAPI (Santa Cruz, 28718-90-3).

Black and white pictures of Sclerostin, DMP1 and DAPI labelling in the entire cortical area were obtained with an AxioObserver Z1 microscope (Zeiss, Darmstad, Germany), at a magnification of 400 (oil immersed objective), and automatically merged using the Mosaic plugin of Axiovision 4.7 software (Zeiss). Mosaic images were directly analyzed with the ImageJ software (<http://imagej.nih.gov/ij/>), without any brightness or contrast correction. ROIs were restricted to the cortical bone. A mask of DAPI cells was merged with Sclerostin or DMP1 staining in order to provide fluorescence intensity data for individual osteocytes. As a lacunar size exceeds the area of DAPI staining, we applied two successive dilations of the DAPI mask to fit with lacunar area. As the “dilated DAPI” area did not entirely match the osteocyte lacuna, pixels in the surrounding bone matrix with zero gray level were sometimes included in the ROI. Because of this we did not calculate the Mean Gray Level and used instead the Raw Integrated Density (RawIntDens) parameter of ImageJ, which sums up the gray levels of all pixels within the ROI. The gray level of collagen and osteocyte autofluorescence was removed with the Subtract function of ImageJ. Intra- and inter-observer coefficients of variation (measurements 3 times with the same operator and 3 times with a

different operator on 5 sections) were less than 3%. To insure representativity of osteocytes population, we analyzed 3 to 4 cortical transversal sections from 5 mice per group; the average number of osteocytes per group was 7500.

Circulating Sclerostin immunoassay

Serum from control and 3-week WBV mice was isolated by 10 min centrifugation at 4400g, aliquoted and stored at -80°C. The Quantikine mouse/rat Sclerostin ELISA kit (R&D systems, MSST00) was used in accordance with the manufacture protocol.

Statistical analysis

Data analysis was performed with the STATISTICA[®] software (version 8.2; StataCorp, College Station, TX). When age-matched controls and experimental groups were compared, data were assessed with the non-parametric Mann-Whitney U-test. When basal controls, age-matched controls and experimental groups were compared altogether (to assess growth effects), data were assessed with the non-parametric Kruskal-Wallis ANOVA test; if significant differences were detected, it was followed by the non-parametric post-hoc Mann-Whitney U-tests with Bonferroni correction.

Results

2g/90Hz WBV does not affect mouse growth

To assess the growth-related differences between 7 week-old (basal control), 10 week-old (3-week WBV experiment) and 16 week-old (9-week WBV experiment) mice, we compared the basal control group with respective age-matched controls. While as expected we found an increase in body weight ($p < 0.05$), which usually comes with age, and a decrease in LGR ($p < 0.002$), WBV did not affect these parameters, neither after 3 weeks, nor after 9 weeks (Fig. 4).

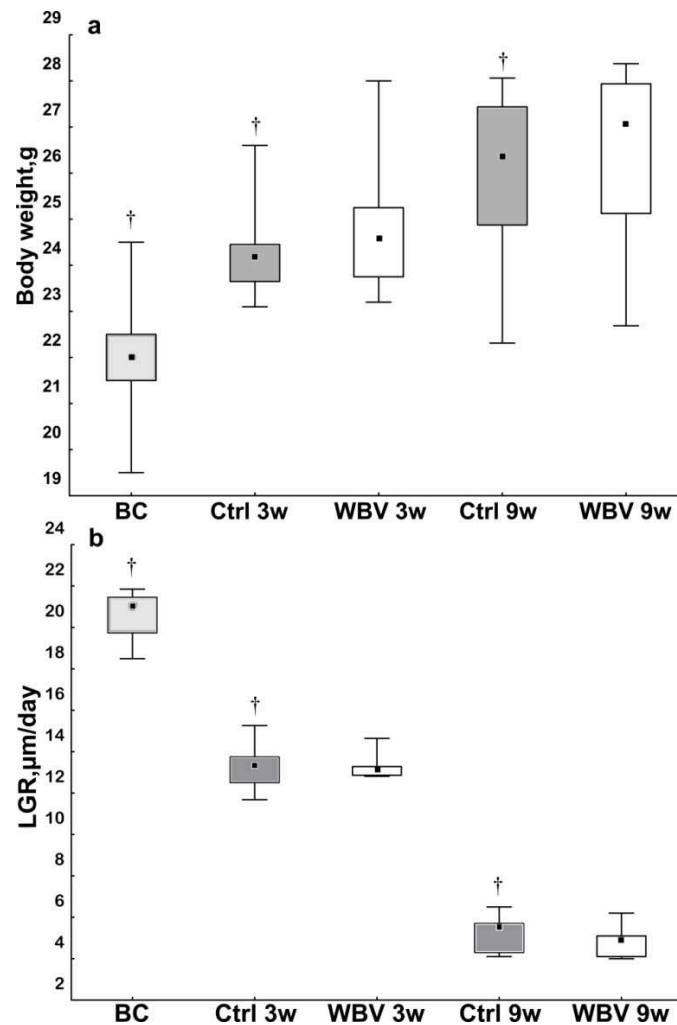


Figure 4. Effects of whole body vibration on growth processes. Animals body weight (a); longitudinal growth rate (b). BC = basal control, Ctrl = age-matched control, WBV = whole body vibration, w = weeks. Boxes represent 50% of values (25% to 75%), whiskers represent minimum and maximum values, middle point represents median. Non-parametric Kruskal-Wallis ANOVA test followed by post-hoc Mann-Whitney U-tests with Bonferroni correction, † indicates difference ($p < 0.01$) between BC, and Ctrl 3w or Ctrl 9w.

Three weeks of WBV accelerates cortical bone growth

Dynamic bone formation parameters were increased in the trabecular bone of the distal femur and L2 vertebral body, as compared to age-matched controls (Fig. 5). In addition, OS/BS only detectable in femur was also increased by WBV (Fig.5). Osteoclast surfaces (Oc.S/BS) were also higher after 3 weeks of WBV (Fig.5e, 5i).

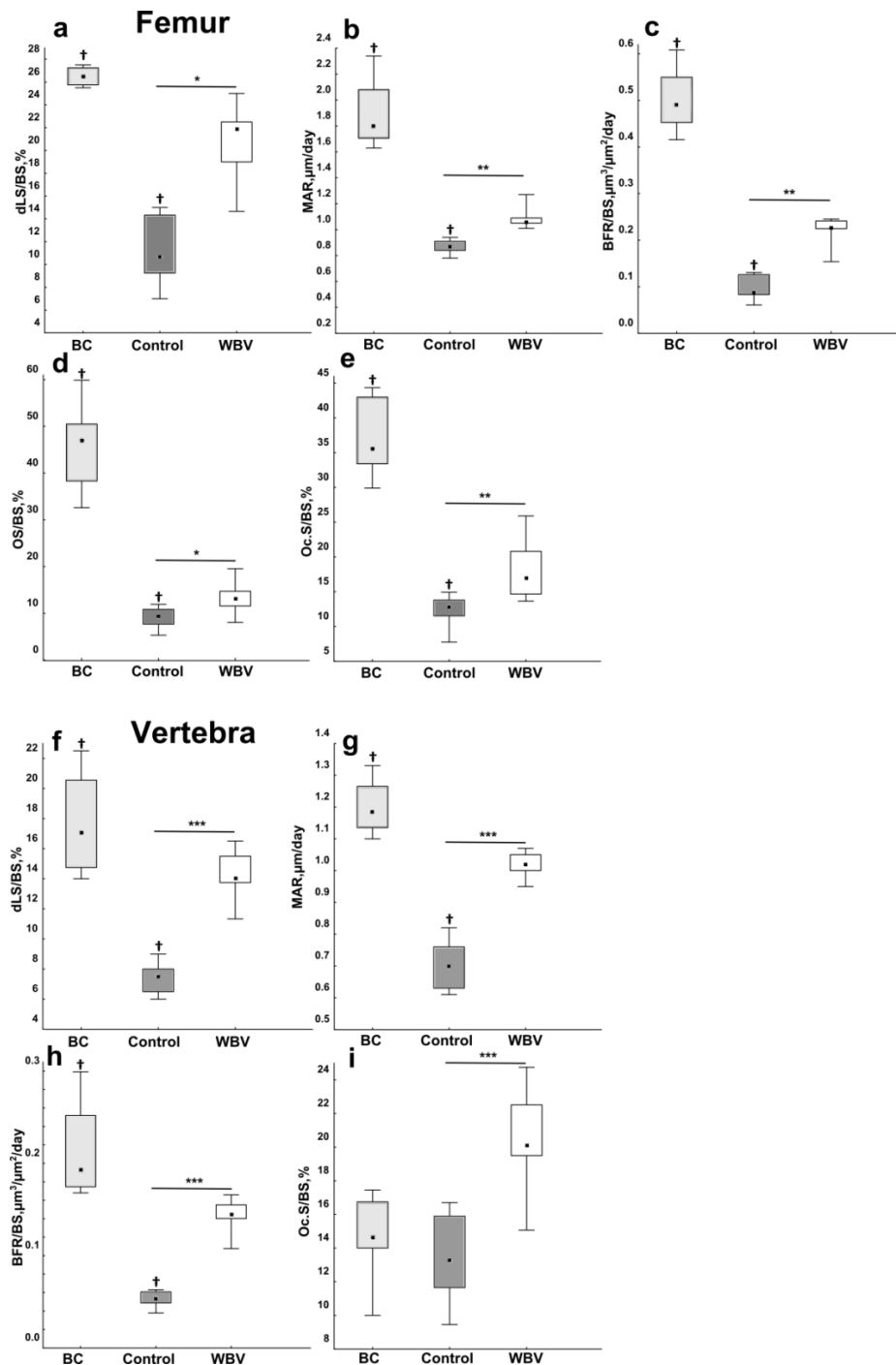


Figure 5. Effects of 3-week whole body vibration on trabecular bone cellular activities. dLS = double labeled surface, MAR = mineral apposition rate, BFR = bone formation rate, OS = osteoid surface, Oc.S = osteoclast surface, BS = bone surface. Analysis was performed in distal femoral metaphysis (a,b,c,d,e), and L2 vertebral body (f,g,h,i). BC = basal control, Control = age-matched control, WBV = whole body vibration. Boxes represent 50% of values (25% to 75%), whiskers represent minimum and maximum values, middle point represents median. Non-parametric Kruskal-Wallis ANOVA test followed by post-hoc Mann-Whitney U-tests with Bonferroni correction. † indicates difference ($p < 0.01$) between BC, and Control, * indicates difference ($*p < 0.05$, $**p < 0.01$, $***p < 0.001$) between Control and WBV.

Three-week WBV also led to 23% increase of vessels number in the femur metaphysis vs. age-matched controls, with no change of vessel volume (Fig. 3b, 2c).

However, this stimulation of bone cellular activities did not translate into a net increase of any trabecular parameters (Table 1).

Table 1. μ CT analysis of femoral diaphysis, distal metaphysis and L2 vertebral body in basal control, age-matched controls and Whole Body Vibration (WBV) groups.

Groups	BC	Ctrl 3w	WBV 3w	Ctrl 9w	WBV 9w
Femur, Trabecular bone					
BV/TV,%	17.4 ± 4.7	8.6 $\pm 0.9^a$	8.4 ± 1.0	12.2 $\pm 4^a$	12.9 ± 3
Tb.Th, μm	50.5 ± 5	35 $\pm 2^a$	35 ± 2	41 $\pm 6^a$	41 ± 4
Tb.N, mm^{-1}	5.6 ± 0.5	2.4 $\pm 0.2^a$	2.4 ± 0.4	2.9 $\pm 0.6^a$	3.1 ± 0.5
Tb.SP, μm	170 ± 20	377 $\pm 27^a$	390 ± 55	322 $\pm 93^a$	287 ± 60
Conn.D, mm^{-3}	161.3 ± 48.3	45.0 $\pm 11.2^a$	46.8 ± 17.8	60.6 $\pm 24^a$	74 ± 23
SMI	2.23 ± 0.3	3.1 $\pm 0.1^a$	3.1 ± 0.1	2.6 $\pm 0.5^{a,c}$	2.5 ± 0.4
DA	1.7 ± 0.04	1.33 $\pm 0.07^a$	1.42 ± 0.12	1.4 $\pm 0.2^a$	1.5 ± 1.2
Vertebra, Trabecular bone					
BV/TV,%	17.1 ± 1.9	21.7 $\pm 2^a$	21.5 ± 2	23.6 $\pm 3^a$	26.3 ± 4
Tb.Th, μm	43 ± 2	39 $\pm 2^a$	39 ± 1	43 ± 4	45 ± 4
Tb.N, mm^{-1}	5.4 ± 0.1	5.6 ± 0.3	5.5 ± 0.3	5.5 ± 0.2	5.9 ± 0.2
Tb.SP, μm	179 ± 4	141 $\pm 11^a$	143 ± 12	140 $\pm 11^a$	125 ± 9
Conn.D, mm^{-3}	191.2 ± 19.1	240.4 $\pm 13.5^a$	231.7 ± 30.7	199 $\pm 15^c$	200 ± 19
SMI	1.8 ± 0.2	1.2 $\pm 0.2^a$	1.2 ± 0.1	0.9 $\pm 0.3^{a,c}$	0.8 ± 0.3
DA	1.82 ± 0.07	1.59 $\pm 0.04^a$	1.6 ± 0.05	1.8 $\pm 0.1^c$	1.9 ± 0.1

Data are shown as mean \pm SD. BC = basal control group, Ctrl = age-matched control, WBV = whole body vibration, w = weeks. BC compared to Ctrl 3w and Ctrl 9w; Ctrl compared to relevant WBV (non-parametric Kruskal-Wallis ANOVA test followed by post-hoc Mann-Whitney U-tests with Bonferroni correction). Marked with the letter (a) when there is significant $p < 0.05$ difference between BC and Ctrl 3w or Ctrl 9w; marked with the letter (c) when there is significant $p < 0.05$ difference between Ctrl 3w and Ctrl 9w.

At the cortical level, WBV resulted in 5% increase of Ct.Th and 6% increase of Ct.Ar as compared to age-matched controls (Fig. 6). Also, cortical MAR was 60% higher ($p < 0.05$) in vibrated group (2.1 ± 0.4 , $\mu\text{m}/\text{day}$) as compared to age-matched controls (1.3 ± 0.3 , $\mu\text{m}/\text{day}$) (Supplementary Fig.1).

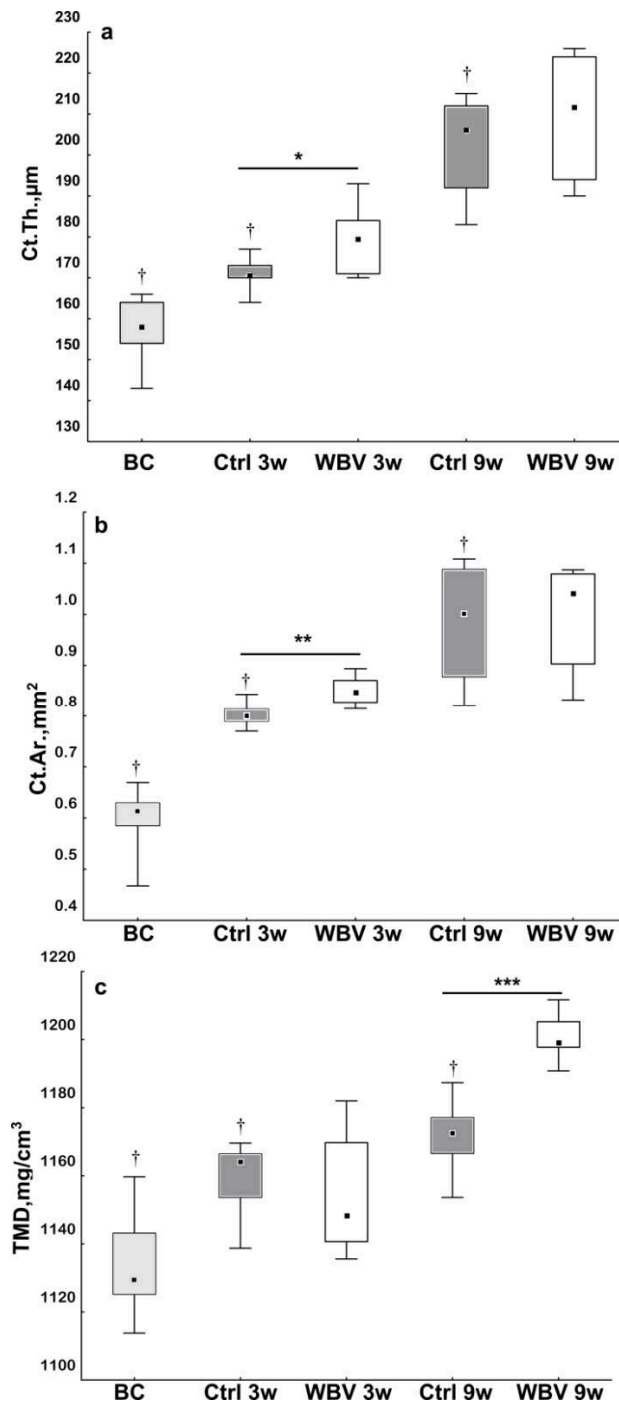


Figure 6. Effects of whole body vibration on cortical bone mass-structural parameters. Cortical thickness (a); cortical area (b); tissue mineral density (c). BC = basal control, Ctrl = age-matched control, WBV = whole body vibration, w = weeks. Boxes represent 50% of values (25% to 75%), whiskers represent minimum and maximum values, middle point represents median. Non-parametric Kruskal-Wallis ANOVA test followed by post-hoc Mann-Whitney U-tests with Bonferroni correction. † indicates difference ($p < 0.01$) between BC, and Ctrl 3w or Ctrl 9w. * indicates difference ($*p < 0.05$, $**p < 0.01$, $***p < 0.001$) between Ctrl and relevant WBV groups.

While a percent of Sclerostin positive osteocytes was 11.5% lower in the WBV group, the fraction of DMP1 positive osteocytes remained unchanged (Table 2).

Table 2. Effects of three-week WBV on osteocyte quantitative parameters in femur cortical bone compared to control: osteocyte density (DAPI staining); immunohistochemistry: percentage of osteocyte positive for Sclerostin or DMP1 and fluorescence levels (RawIntDens, arbitrary unit).

Groups	Control		WBV	
Osteocytes density, 1/1000 μm^2	0.82 \pm 0.08		0.84 \pm 0.04	
	Sclerostin	DMP1	Sclerostin	DMP1
Positive osteocytes, %	77%	71.5%	68.1%***	70.8%
RawIntDens per group	3656	2430	2751***	3300***

Data are shown as mean for osteocytes' density and percentage of positive; as medians for level of fluorescence. Non-parametric Mann-Whitney U-test, WBV compared to age-matched controls, *** $p \leq 0.002$.

Assessing the fluorescence intensity of individual osteocytes showed that Sclerostin protein expression was 25% lower in the WBV group; DMP1 expression was 35% higher than in age-matched controls (Table 2, Fig. 7). No difference in osteocyte density was detected.

Additionally no differences in the levels of circulating Sclerostin were observed between control (194 \pm 36 pg/ml, n=8) and WBV mice (184 \pm 37 pg/ml, n=8).

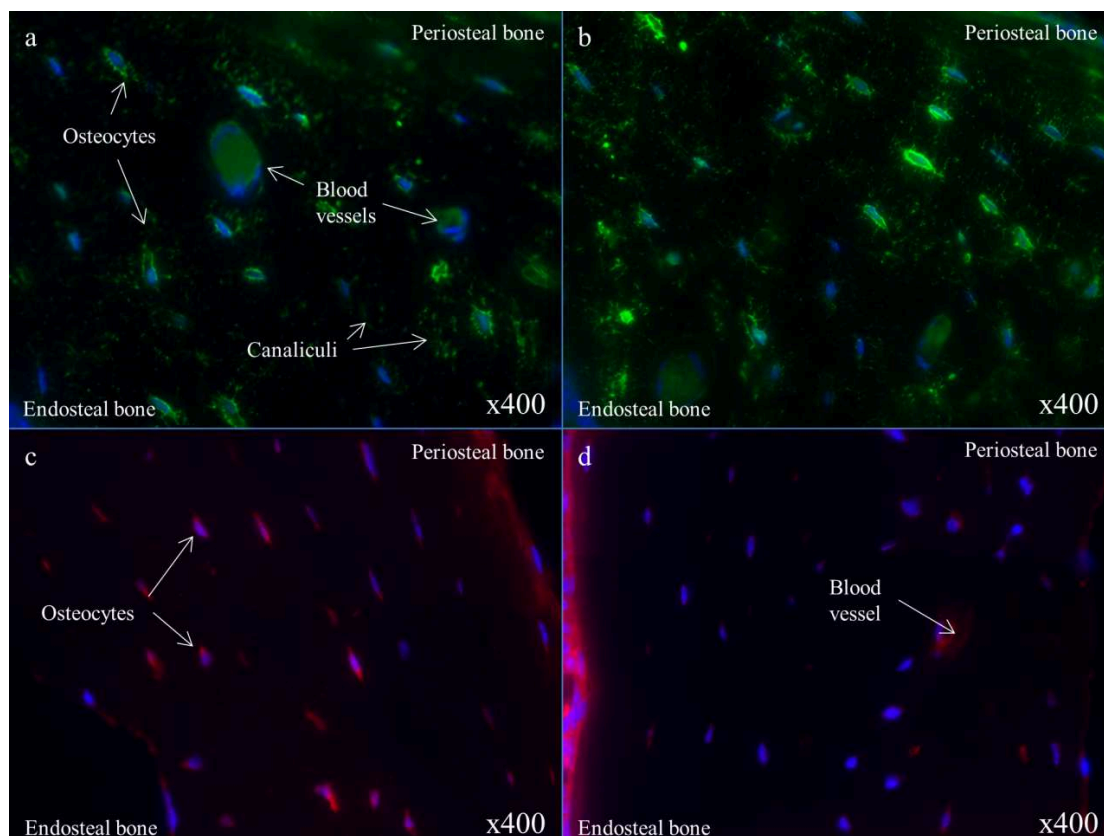


Figure 7. Representative pictures of immunohistochemistry on cortical bone. DAPI (blue) and DMP1 staining (green) of control (a) and 3-week WBV experimental (b) groups; DAPI (blue) and Sclerostin (red) staining of control (c) and 3-week WBV experimental (d) groups. Blood vessels, bone marrow and collagen are visible due to their natural autofluorescence. Pictures are part of total cortical bone mosaic images, which were used for fluorescence quantitative analysis (chapter materials and methods). Images were equally adjusted for brightness and contrast for demonstrative purposes.

Nine weeks of WBV results in a net increase in bone matrix mineral content

To test whether cellular activity changes will finally result in bone mass alteration we performed a longer WBV experiment. After 9-week 2g/90Hz WBV the femoral cortical TMD increased by 2.5% as compared to age-matched controls ($p < 0.001$, Fig. 6). Bone structural or cellular parameters in both femur and vertebra did not show any change (Table 2).

Discussion

One of the main findings was that 2g/90Hz WBV selectively promotes cortical bone growth in healthy animals, while it does not result in any observable alterations of trabecular compartment architecture. Several studies reported a stimulatory effect of WBV on cortical bone in ovariectomized animals [6,18,19], however to the best of our knowledge, there is only one study to report an increase of Ct.Th in healthy mice [7].

In relation to cellular activities, it has been shown that WBV stimulates bone formation and decreases osteoclastic parameters [5,10]. We also found that three weeks of 2g/90Hz WBV resulted in augmented osteoid and mineralized surfaces, presumably due to an increase of osteoblast recruitment and/or lifespan. Interestingly, cellular activities changed more in vertebra than in femur. This could be explained by higher local peak acceleration in the vertebra compared to hindlimbs, as our team previously recorded in rats during a 0.7g WBV study [7]. In growing mice, along with higher bone formation rate we detected an increase of Oc.S/BS in both femur metaphysis and vertebra. It is possible that in young healthy animals a 2g/90Hz WBV regimen would stimulate both formation and resorption activities, thus maintaining trabecular microarchitecture.

WBV has been shown to stimulate angiogenesis in fractured [20] and unloaded [21] bones. A link between load-induced bone gain and vascularization has also been detected [22–24]. Thus, the observed increase of vessel number after 2g/90Hz WBV confirms previous findings. Higher number of vessels after WBV treatment may be associated with the increased bone cellular activities, as vessels play an essential role in basic multicellular units where bone remodeling takes place [25]. Our findings further emphasize the importance of vascularization in bone adaptation processes.

In experimental models of high mechanical loading, osteocyte expression of Sclerostin has been reported to be reduced, while that of DMP1 was increased [26–28]. Our quantitative

IHC analysis allowed us to detect reduction of the percentage of osteocytes positive for Sclerostin along with shifts in Sclerostin and DMP1 expression. Although these effects of WBV appear modest, it must be considered that WBV generates a much lower mechanical strain (e.g., $23.4\mu\epsilon$ for 3g/30Hz WBV in long bones of rats [6]) than axial loading (up to $2200\mu\epsilon$ [26]). We did not find any changes in circulating Sclerostin suggesting that changes in serum levels do not necessarily reflect alterations of local production in osteocytes. Alternatively, decreased protein expression in femur diaphysis may not represent a generalized effect, as has been shown in ovariectomized mice [29].

As after three-week WBV we observed altered cellular activities in trabecular bone, a thicker cortex and higher DMP1, we assumed that a longer exposure to WBV may further stimulate adaptation processes and result in trabecular bone gain or cortex mineralization.

However, after nine weeks of 2g/90Hz WBV we still observed no changes of trabecular bone microarchitecture, and, in contrast to three-week WBV, no difference in cellular activities either in femur or vertebra. The latter may indicate that a steady state has been achieved in the adaptation of the skeleton to this mechanical environment.

While after 3-week WBV cortical size was increased, the difference between WBV and controls disappeared after 9 weeks. However, only after 9-week WBV we detected higher cortical TMD in experimental group compared to controls. The age of mice at the end of the experiment corresponded to their skeleton maturity [30,31]. We showed that exposure to 2g/90Hz WBV resulted in increased cortical peak bone mass. Importantly, such strengthening of the skeleton in period of skeletal growth could defer the onset of age-related bone loss [32,33]. Our findings suggested that young mice adapted to WBV by accelerating their natural growth processes, i.e., increasing cortical thickness, subsequently followed by mineralization. We also assumed that higher expression of DMP1 after 3-week WBV might contribute to latter tissue mineralization, as DMP1 is known to control mineralization processes [34–36].

Similar age-related differences in the effects of mechanical loading have been previously observed in rats subjected to running exercise [37]. In that study, while young animals (5 week-old) mostly displayed an increase of cortical cross-sectional area, adult rats (50 week-old) adapted through increase of bone mineral density. It is possible that the main effect of WBV would be to accelerate radial bone growth, and that the increase in TMD would reflect

the faster maturation of the bone matrix in vibrated mice, which would leave a longer time for secondary mineralization.

We did not observe any differences in animal body weight of WBV groups compared to controls throughout the experiments, and there were no detectable negative effects on bone growth or mass-structural parameters.

In conclusion, while WBV at acceleration of less than 1g had little or no effect on healthy animals, 2g/90Hz WBV affected healthy animals in a site-specific manner. It stimulated cortical bone growth after three weeks, and increased peak TMD in older animals after nine weeks. Our results suggest that WBV mechanical stimulation could increase the peak bone mass at the end of the skeletal growth phase, and do so in a safe and easy manner, which may lead to substantial strengthening of the skeleton and thereby defer the onset of osteoporosis.

Acknowledgments

We acknowledge financial support from the French National Space Agency (CNES) (Program ‘Microgravity and Development’), the ‘Agence Nationale de la Recherche’ ANR-09-BLAN-0148 (AdapHyG), and INSERM (Institut National de la Santé et de la Recherche Médicale). V. Gnyubkin had a scholarship from French Ministry of Higher Education and Research. We thank the staff of the animal facility PLEXAN of the University of Saint-Etienne. We are also grateful to E. Berger, V. Mucci, F. Louis and W. Bouleftour for technical assistance.

Ethical approval

All applicable international, national, and/or institutional guidelines for the care and use of animals were followed.

Conflict of Interest

The authors declare that they have no conflict of interest.

References

- [1] Smith SM, Heer MA, Shackelford LC, Sibonga JD, Ploutz-Snyder L, Zwart SR. Benefits for bone from resistance exercise and nutrition in long-duration spaceflight: Evidence from biochemistry and densitometry. *J Bone Miner Res* 2012;27:1896–906. doi:10.1002/jbmr.1647.

- [2] Tobias JH, Gould V, Brunton L, Deere K, Rittweger J, Lipperts M, et al. Physical Activity and Bone: May the Force be with You. *Front Endocrinol* 2014;5:20. doi:10.3389/fendo.2014.00020.
- [3] Qin YX, Rubin CT, McLeod KJ. Nonlinear dependence of loading intensity and cycle number in the maintenance of bone mass and morphology. *J Orthop Res* 1998;16:482–9. doi:10.1002/jor.1100160414.
- [4] Rubin C, Turner AS, Bain S, Mallinckrodt C, McLeod K. Anabolism. Low mechanical signals strengthen long bones. *Nature* 2001;412:603–4. doi:10.1038/35088122.
- [5] Prisby RD, Lafage-Proust M-H, Malaval L, Belli A, Vico L. Effects of whole body vibration on the skeleton and other organ systems in man and animal models: What we know and what we need to know. *Ageing Res Rev* 2008;7:319–29. doi:10.1016/j.arr.2008.07.004.
- [6] Rubinacci A, Marenzana M, Cavani F, Colasante F, Villa I, Willnecker J, et al. Ovariectomy sensitizes rat cortical bone to whole-body vibration. *Calcif Tissue Int* 2008;82:316–26. doi:10.1007/s00223-008-9115-8.
- [7] Pasqualini M, Lavet C, Elbadaoui M, Vanden-Bossche A, Laroche N, Gnyubkin V, et al. Skeletal site-specific effects of whole body vibration in mature rats: from deleterious to beneficial frequency-dependent effects. *Bone* 2013;55:69–77. doi:10.1016/j.bone.2013.03.013.
- [8] Judex S, Lei X, Han D, Rubin C. Low-magnitude mechanical signals that stimulate bone formation in the ovariectomized rat are dependent on the applied frequency but not on the strain magnitude. *J Biomech* 2007;40:1333–9. doi:10.1016/j.jbiomech.2006.05.014.
- [9] Zhang R, Gong H, Zhu D, Gao J, Fang J, Fan Y. Seven day insertion rest in whole body vibration improves multi-level bone quality in tail suspension rats. *PloS One* 2014;9:e92312. doi:10.1371/journal.pone.0092312.
- [10] Xie L, Jacobson JM, Choi ES, Busa B, Donahue LR, Miller LM, et al. Low-level mechanical vibrations can influence bone resorption and bone formation in the growing skeleton. *Bone* 2006;39:1059–66. doi:10.1016/j.bone.2006.05.012.
- [11] Rubin C, Turner AS, Mallinckrodt C, Jerome C, McLeod K, Bain S. Mechanical strain, induced noninvasively in the high-frequency domain, is anabolic to cancellous bone, but not cortical bone. *Bone* 2002;30:445–52.
- [12] Lynch MA, Brodt MD, Silva MJ. Skeletal Effects of Whole-Body Vibration in Adult and Aged Mice. *J Orthop Res* 2010;28:241–7. doi:10.1002/jor.20965.

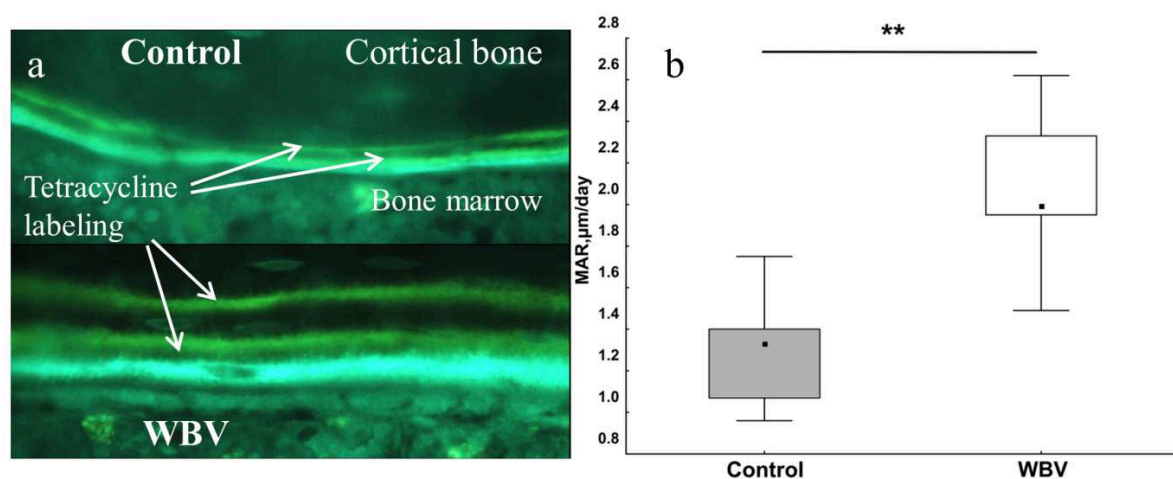
- [13] Ozcivici E, Luu YK, Adler B, Qin Y-X, Rubin J, Judex S, et al. Mechanical signals as anabolic agents in bone. *Nat Rev Rheumatol* 2010;6:50–9. doi:10.1038/nrrheum.2009.239.
- [14] Flieger J, Karachalios T, Khaldi L, Raptou P, Lyritis G. Mechanical stimulation in the form of vibration prevents postmenopausal bone loss in ovariectomized rats. *Calcif Tissue Int* 1998;63:510–4.
- [15] David V, Lafage-Proust M-H, Laroche N, Christian A, Ruegsegger P, Vico L. Two-week longitudinal survey of bone architecture alteration in the hindlimb-unloaded rat model of bone loss: sex differences. *Am J Physiol Endocrinol Metab* 2006;290:E440–7. doi:10.1152/ajpendo.00293.2004.
- [16] Roche B, David V, Vanden-Bossche A, Peyrin F, Malaval L, Vico L, et al. Structure and quantification of microvascularisation within mouse long bones: what and how should we measure? *Bone* 2012;50:390–9. doi:10.1016/j.bone.2011.09.051.
- [17] Gerdes MJ, Sevinsky CJ, Sood A, Adak S, Bello MO, Bordwell A, et al. Highly multiplexed single-cell analysis of formalin-fixed, paraffin-embedded cancer tissue. *Proc Natl Acad Sci* 2013;110:11982–7. doi:10.1073/pnas.1300136110.
- [18] Sehmisch S, Galal R, Kolios L, Tezval M, Dullin C, Zimmer S, et al. Effects of low-magnitude, high-frequency mechanical stimulation in the rat osteopenia model. *Osteoporos Int* 2009;20:1999–2008. doi:10.1007/s00198-009-0892-3.
- [19] Stuermer EK, Komrakova M, Werner C, Wicke M, Kolios L, Sehmisch S, et al. Musculoskeletal Response to Whole-Body Vibration During Fracture Healing in Intact and Ovariectomized Rats. *Calcif Tissue Int* 2010;87:168–80. doi:10.1007/s00223-010-9381-0.
- [20] Cheung W-H, Sun M-H, Zheng Y-P, Chu WC-W, Leung AH-C, Qin L, et al. Stimulated Angiogenesis for Fracture Healing Augmented by Low-Magnitude, High-Frequency Vibration in A Rat Model—Evaluation of Pulsed-Wave Doppler, 3-D Power Doppler Ultrasonography and Micro-CT Microangiography. *Ultrasound Med Biol* 2012;38:2120–9. doi:10.1016/j.ultrasmedbio.2012.07.025.
- [21] Kaneguchi A, Ozawa J, Kawamata S, Kurose T, Yamaoka K. Intermittent whole-body vibration attenuates a reduction in the number of the capillaries in unloaded rat skeletal muscle. *BMC Musculoskelet Disord* 2014;15:315. doi:10.1186/1471-2474-15-315.
- [22] Barou O, Mekraldi S, Vico L, Boivin G, Alexandre C, Lafage-Proust MH. Relationships between trabecular bone remodeling and bone vascularization: a quantitative study. *Bone* 2002;30:604–12. doi:10.1016/S8756-3282(02)00677-4.

- [23] Yao Z, Lafage-Proust M-H, Plouët J, Bloomfield S, Alexandre C, Vico L. Increase of both angiogenesis and bone mass in response to exercise depends on VEGF. *J Bone Miner Res* 2004;19:1471–80. doi:10.1359/JBMR.040517.
- [24] Fei J, Jia F, Peyrin F, Françoise P, Malaval L, Vico L, et al. Imaging and quantitative assessment of long bone vascularization in the adult rat using microcomputed tomography. *Anat Rec Hoboken NJ* 2007 2010;293:215–24. doi:10.1002/ar.21054.
- [25] Sims NA, Martin TJ. Coupling the activities of bone formation and resorption: a multitude of signals within the basic multicellular unit. *BoneKEy Rep* 2014;3. doi:10.1038/bonekey.2013.215.
- [26] Robling AG, Niziolek PJ, Baldrige LA, Condon KW, Allen MR, Alam I, et al. Mechanical stimulation of bone in vivo reduces osteocyte expression of Sost/sclerostin. *J Biol Chem* 2008;283:5866–75. doi:10.1074/jbc.M705092200.
- [27] Gluhak-Heinrich J, Ye L, Bonewald LF, Feng JQ, MacDougall M, Harris SE, et al. Mechanical Loading Stimulates Dentin Matrix Protein 1 (DMP1) Expression in Osteocytes In Vivo. *J Bone Miner Res* 2003;18:807–17. doi:10.1359/jbmr.2003.18.5.807.
- [28] Harris SE, Gluhak-Heinrich J, Harris MA, Yang W, Bonewald LF, Riha D, et al. DMP1 and MEPE expression are elevated in osteocytes after mechanical loading in vivo: theoretical role in controlling mineral quality in the perilacunar matrix. *J Musculoskelet Neuronal Interact* 2007;7:313–5.
- [29] Jastrzebski S, Kalinowski J, Stolina M, Mirza F, Torreggiani E, Kalajzic I, et al. Changes in bone sclerostin levels in mice after ovariectomy vary independently of changes in serum sclerostin levels. *J Bone Miner Res* 2013;28:618–26. doi:10.1002/jbmr.1773.
- [30] Amblard D, Lafage-Proust M-H, Laib A, Thomas T, Rügsegger P, Alexandre C, et al. Tail suspension induces bone loss in skeletally mature mice in the C57BL/6J strain but not in the C3H/HeJ strain. *J Bone Miner Res* 2003;18:561–9. doi:10.1359/jbmr.2003.18.3.561.
- [31] Somerville JM, Aspden RM, Armour KE, Armour KJ, Reid DM. Growth of C57Bl/6 Mice and the Material and Mechanical Properties of Cortical Bone from the Tibia. *Calcif Tissue Int* 2004;74:469–75. doi:10.1007/s00223-003-0101-x.
- [32] Tatò L, Antoniazzi F, Zamboni G. [Bone mass formation in childhood and risk of osteoporosis]. *Pediatr Medica* 1996;18:373–5.
- [33] Hernandez CJ, Beaupré GS, Carter DR. A theoretical analysis of the relative influences of peak BMD, age-related bone loss and menopause on the development of osteoporosis. *Osteoporos Int* 2003;14:843–7. doi:10.1007/s00198-003-1454-8.

- [34] Ling Y, Rios HF, Myers ER, Lu Y, Feng JQ, Boskey AL. DMP1 depletion decreases bone mineralization in vivo: an FTIR imaging analysis. *J Bone Miner* 2005;20:2169–77. doi:10.1359/JBMR.050815.
- [35] Feng JQ, Ward LM, Liu S, Lu Y, Xie Y, Yuan B, et al. Loss of DMP1 causes rickets and osteomalacia and identifies a role for osteocytes in mineral metabolism. *Nat Genet* 2006;38:1310–5. doi:10.1038/ng1905.
- [36] Maciejewska I, Qin D, Huang B, Sun Y, Mues G, Svoboda K, et al. Distinct compartmentalization of dentin matrix protein 1 fragments in mineralized tissues and cells. *Cells Tissues Organs* 2009;189:186–91. doi:10.1159/000151372.
- [37] Järvinen TL, Pajamäki I, Sievänen H, Vuohelainen T, Tuukkanen J, Järvinen M, et al. Femoral Neck Response to Exercise and Subsequent Deconditioning in Young and Adult Rats. *J Bone Miner Res* 2003;18:1292–9. doi:10.1359/jbmr.2003.18.7.1292.

Supplementary information

Supplementary figure 1. Effects of 3-week whole body vibration on endosteal cortical bone growth. Representative images (x400) of double tetracycline labeling in femur cortical bone (a), mineral apposition rate (b). Control = age-matched control, WBV = whole body vibration. Boxes represent 50% of values (25% to 75%), whiskers represent minimum and maximum values, middle point represents median. Non-parametric Mann-Whitney U-test, **p<0.01



Supplementary figure 1. Effects of 3-week whole body vibration on endosteal cortical bone growth. Representative images (x400) of double tetracycline labeling in femur cortical bone (a), mineral apposition rate (b). Control = age-matched control, WBV = whole body vibration. Boxes represent 50% of values (25% to 75%), whiskers represent minimum and maximum values, middle point represents median. Non-parametric Mann-Whitney U-test, **p<0.01

Not published data (0.5g, 0.5-2g)

In the 9-week WBV experiment there were also two more groups: one that received WBV with the acceleration of 0.5g at 90Hz, and a group that received WBV with progressively increased acceleration from 0.5g to 2g. The increment was done equally twice a week thus the first WBV session was at 0.5g and the last WBV session was at 2g. Animals of these groups similar to 2g/90Hz group stayed the first week at 0.5g acceleration for acclimatization. At the end of experiment femur and L2 vertebrae were harvested, fixed and processed for μ CT as described in Materials and Methods chapter. We have observed that 9-week WBV at 0.5g or with the increment from 0.5g to 2g both had no statistically significant effects on bone mass-structural parameters of healthy animals (Fig. 11, Fig. 12, Fig. 13). We only observed a trend for increasing of TMD after WBV at progressively increased acceleration (Fig.11a). We hypothesized that it happened because animals were treated by WBV with the acceleration $>1g$ (presumably osteogenic) yet not long enough to cause significant alterations.

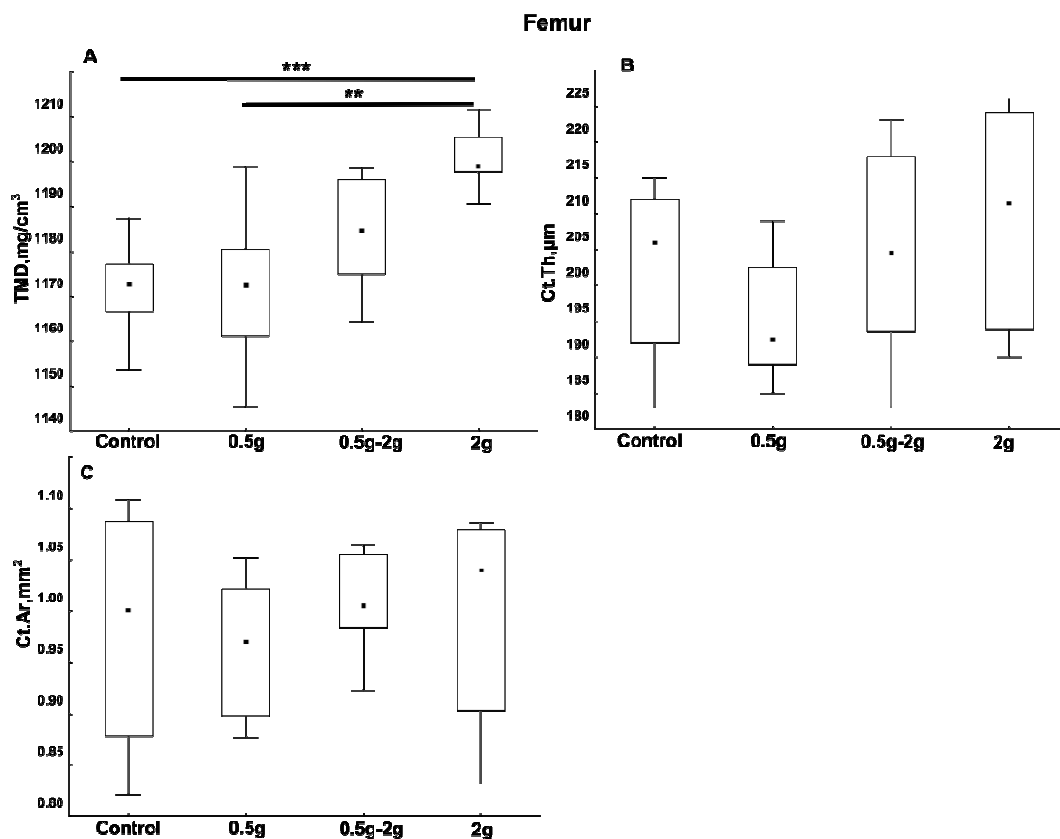


Figure 11. Effects of whole body vibration at different accelerations on cortical bone mass-structural parameters. tissue mineral density (a); Cortical thickness (b); cortical area (c). Boxes represent 50% of values (25% to 75%), whiskers represent minimum and maximum values, middle point represents

median. Non-parametric Kruskal-Wallis ANOVA test followed by post-hoc Mann-Whitney U-tests with Bonferroni correction. * indicates difference (** $p < 0.01$, *** $p < 0.001$).

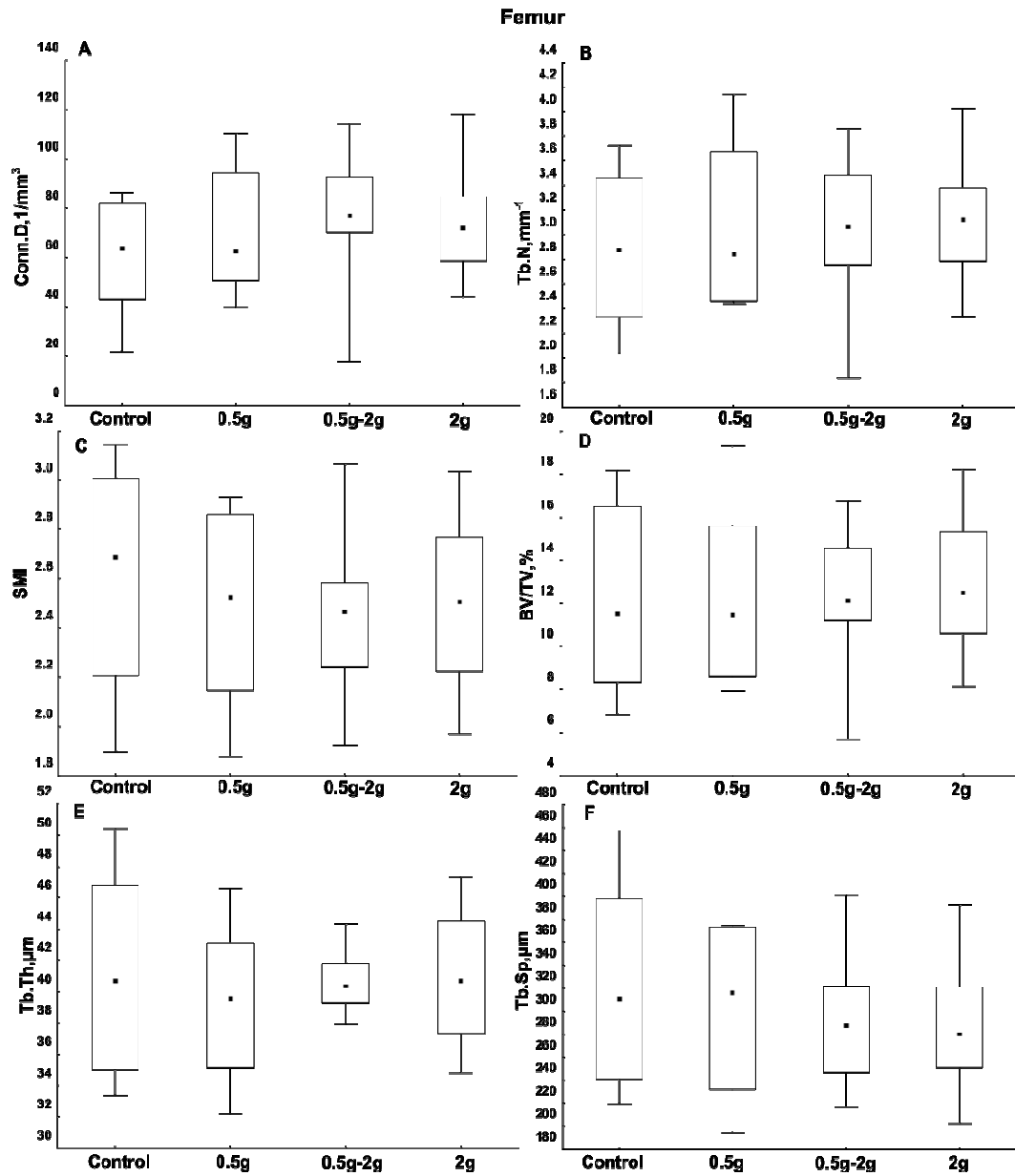


Figure 12. Effects of whole body vibration at different accelerations on trabecular bone structural parameters. Connectivity density (a), trabecular number (b), structure model index (c), bone volume (d), trabecular thickness (e), trabecular separation (f). Boxes represent 50% of values (25% to 75%), whiskers represent minimum and maximum values, middle point represents median. Non-parametric Kruskal-Wallis ANOVA test.

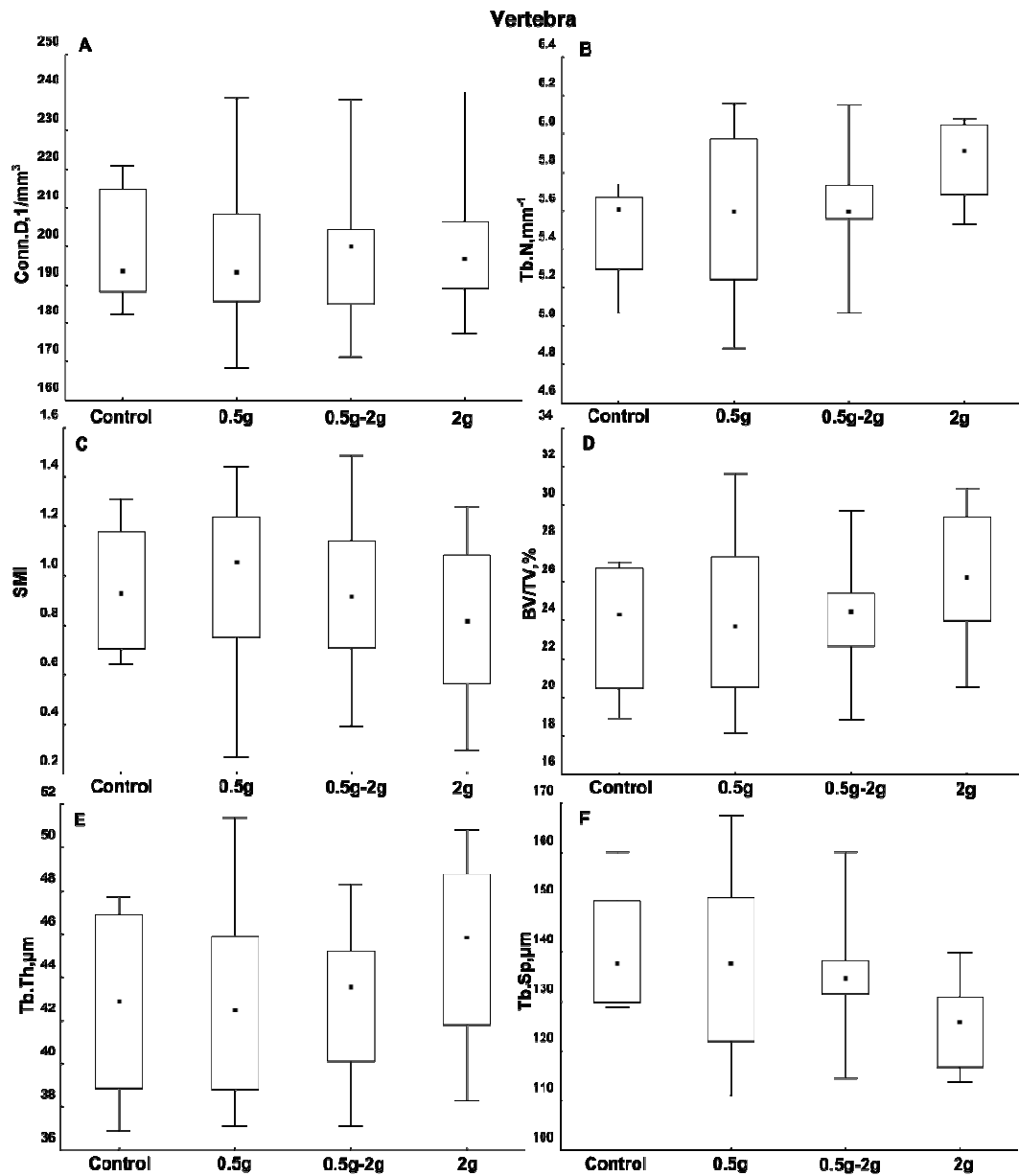


Figure 13. Effects of whole body vibration at different accelerations on trabecular bone structural parameters. Connectivity density (a), trabecular number (b), structure model index (c), bone volume (d), trabecular thickness (e), trabecular separation (f). Boxes represent 50% of values (25% to 75%), whiskers represent minimum and maximum values, middle point represents median. Non-parametric Kruskal-Wallis ANOVA test.

Conclusion /perspective

Different WBV regimes and durations were tested. We found that while high-acceleration 2g/90Hz WBV altered bone mass-structural parameters, 0.5g and 0.5g-2g WBV failed to trigger bone growth in healthy animals.

Important finding was that 2g/90Hz WBV increased cortical peak bone density and showed no negative effects. Surprisingly, stimulation of cellular activities and vascularization in femoral metaphysis did not result in detectable trabecular reorganization and even longer stimulation was not efficient. The question of future studies might be whether 2g/90Hz WBV has protective effects from microgravity- or ovariectomy- or disuse-induced bone loss, or whether it is efficient in older animals? Another important aspect to consider is improvement of bone mechanical properties.

3.3 Immunohistochemical detection of osteocyte proteins

In the two hypergravity studies, our goal was to assess mechanosensitive proteins at osteocyte level. Because of lack of detailed IHC protocols in the literature of reliable staining and representative quantification of such proteins we had to develop optimized techniques in our laboratory for mouse and human bone samples, embedded in paraffin or methyl methacrylate. Thus, a significant part of work was dedicated to the technical objective of current research project, which was to establish the reliable protocols for immunohistochemical detection of osteocyte proteins. The importance of this analytical approach is hard to overestimate in studies of bone adaptations to mechanical loading. Therefore, the primary targets were mechanosensitive proteins Sclerostin and DMP1. The first draft of a paper dedicated to technical aspects of quantitative IHC on osteocyte proteins is presented below in this manuscript.

For assessment of bone cellular activities by histomorphometry samples were embedded in methyl methacrylate (MMA), but we also wanted to use already embedded samples for IHC analysis. Therefore, initially, IHC attempts were done on MMA embedded mouse bones with a protocols based on enzymatic signal detections (horseradish peroxidase (HRP). Although we were able to immunolabel Sclerostin on MMA embedded mouse bone sections, the staining and histological quality was unsatisfactory (Fig. 14a, 14d). Next we shifted to a paraffin embedding techniques and successfully established protocols for Sclerostin (Fig.14b, 14c, 14e), DMP1 (Fig. 14f), and Periostin (Fig.14g, 14h) immunolabelings. Additionally, a protocol for double IHC labeling has been established for simultaneous detection of Sclerostin and DMP1 (Fig. 14i). Exact protocols of IHC can be found in the Supplementary materials.

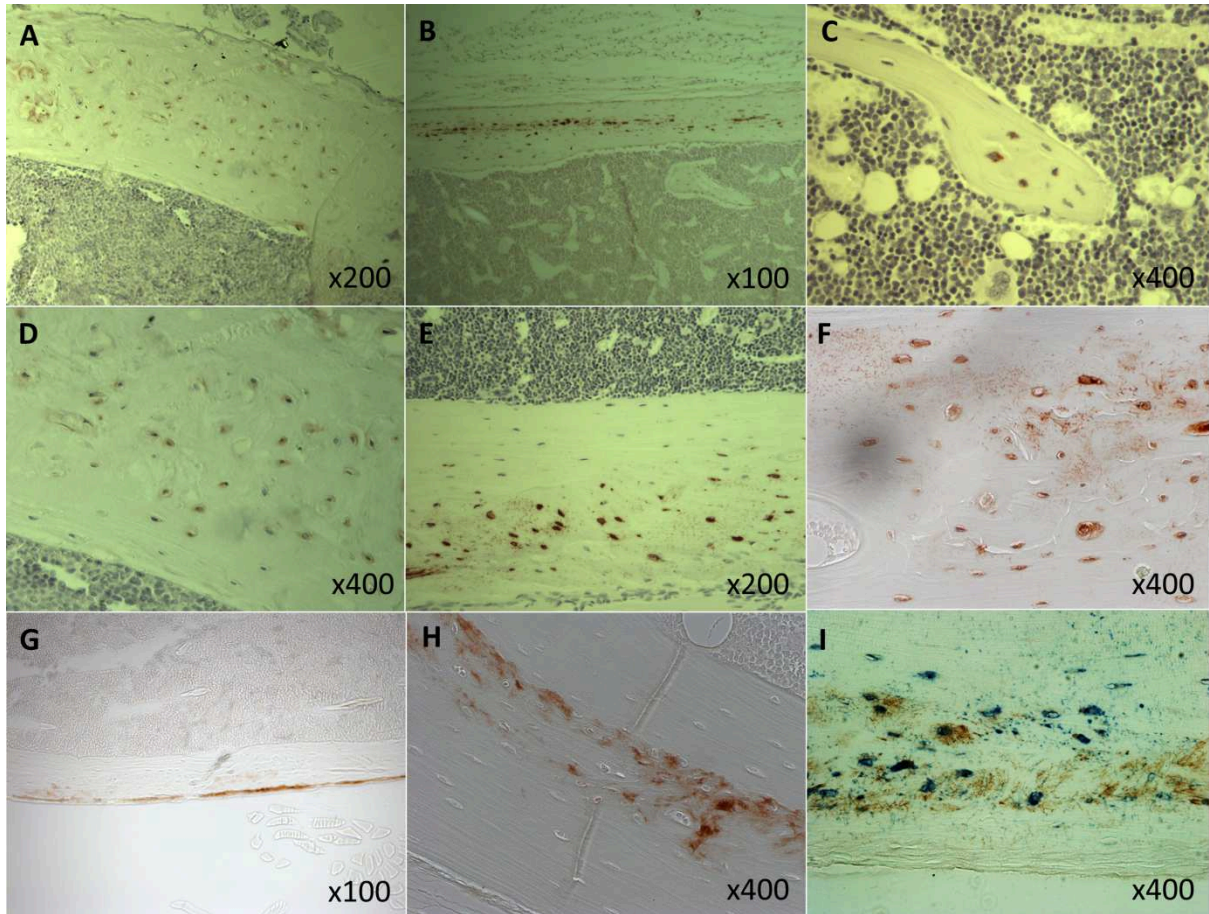


Figure 14. Immunohistochemistry with enzymatic detection of osteocyte proteins in mouse femoral bones. Sclerostin staining (brown) on methyl methacrylate (a,d) and paraffin (b,c,e), DMP1 (f) and Periostin (g,h) staining (brown) on paraffin, double staining of Sclerostin (blue) and DMP1 (brown) on paraffin (i).

Enzymatic detection did not satisfy our needs because it was not suitable for analysis of proteins co-localization due to mutual sheltering of chromogen (HRP and AP) signals, particularly within canalicular system. Fluorescent IHC is much more appropriate tool for analysis of co-localized proteins as different fluorescent dyes have different excitation and emission wave-lengths. Thus, image acquisition can be done separately for each labeled protein and then obtained color images can be merged. Thus, we developed protocols for Sclerostin, DMP1 and Periostin fluorescent IHC labeling for paraffin embedded mouse bones (Fig. 15-19).

The first step was to set up a protocol for a single IHC staining and we began with Sclerostin (Fig. 15). We found that fluorescent IHC is more preferable even for detection of a single protein as it allowed us to see more details compared to HRP based detection. The main problem with HRP detection that we have experienced is that staining develops overtime and long exposure to chromogen, which is necessary see tiny details of canalicular Sclerostin distribution, results in high risk of non-specific background staining, and in overstrained

osteocytes and blood vessels (structures with higher concentration of Sclerostin compared to canaliculi). With the fluorescence IHC, the staining was much more contrast (Fig. 15) and its intensity has been easy to control just by adjusting UV-lamp power and/or exposition time in order to highlight structures with low or high Sclerostin concentration.

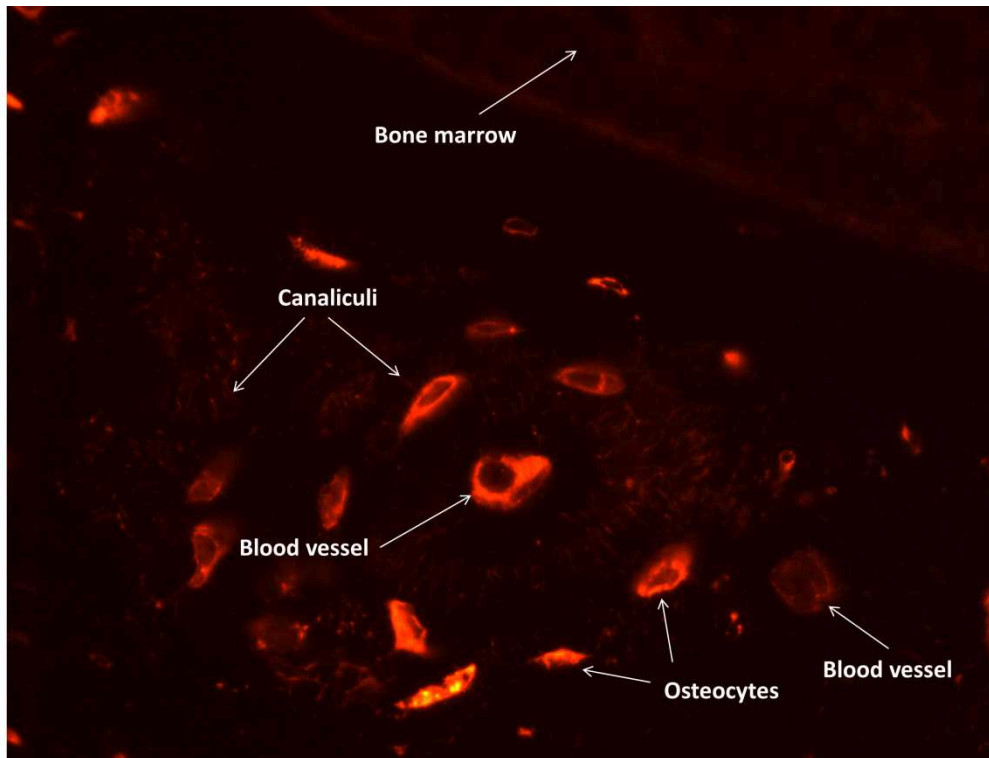


Figure 15. Sclerostin labeling. Fluorescent immunohistochemistry on paraffin embedded mouse femoral cortex. Sclerostin is visible in red in different areas of the cortex: osteocytes, canaliculi and blood vessel walls. Oil immersed objective, x630.

After establishing single-staining protocols for Sclerostin and DMP1, we were interested in analysis of their co-localization. We found that while both proteins were largely presented in osteocytes, DMP1 was much more abundant in canalicular system (Fig. 16 and Fig. 17). Interestingly, we found that Sclerostin was generally localized mostly inside osteocyte lacunae whereas DMP1 was on their perimeters.

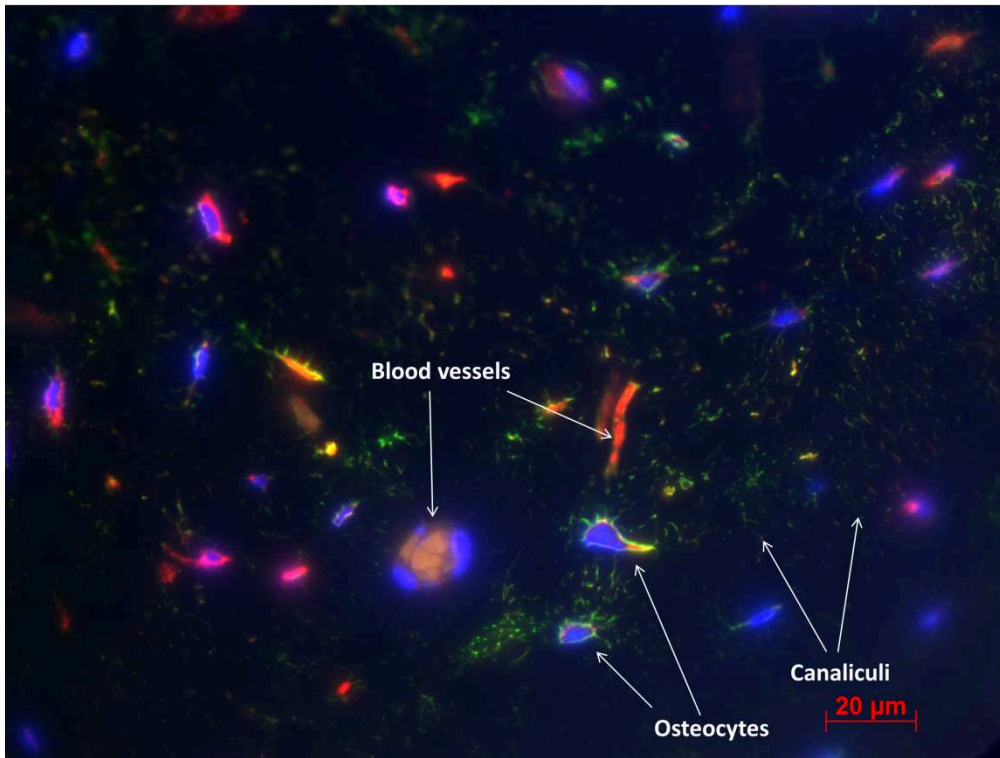


Figure 16. Fluorescent immunohistochemistry on paraffin embedded mouse femoral cortex. Oil immersed objective, x400. Sclerostin labeling (red), DMP1 labeling (green), DAPI labeling (blue). Co-localization of Sclerostin and DMP1 in yellow.

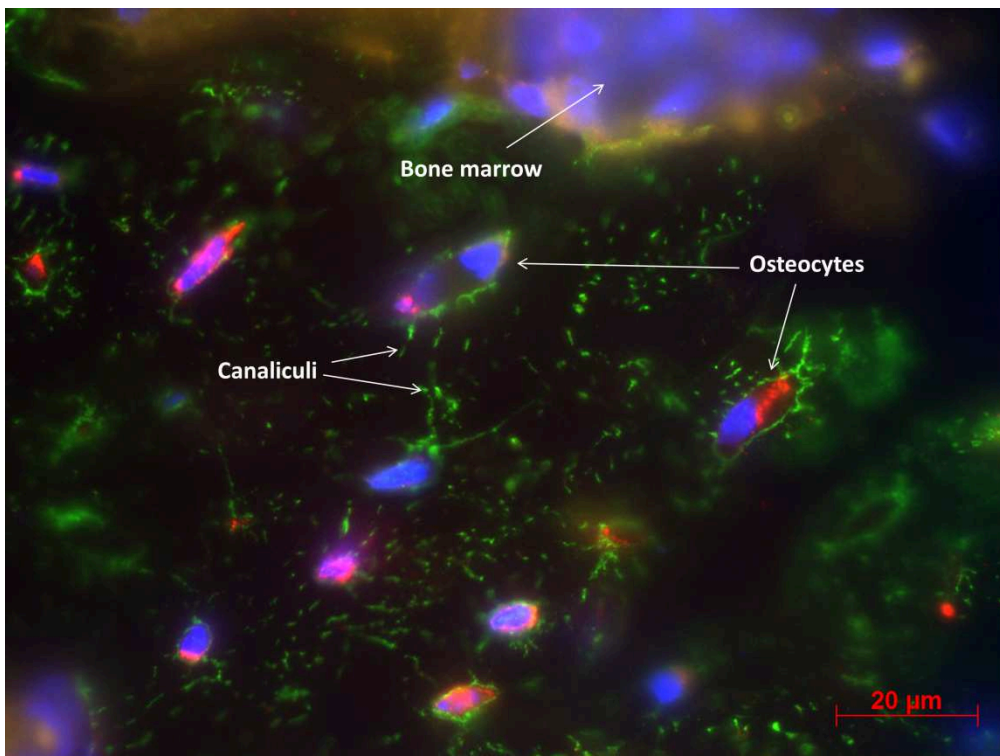


Figure 17. Fluorescent immunohistochemistry on paraffin embedded mouse femoral cortex. Oil immersed objective, x1000. Sclerostin labeling (red), DMP1 labeling (green), DAPI labeling (blue). Co-localization of Sclerostin and DMP1 in yellow.

Sometimes osteocytes contained both proteins intercellularly (Fig. 18, osteocytes on the upper part of the image). We found that vessels were often positive for Sclerostin, however due to technical limitations it was impossible to detect its exact localization.

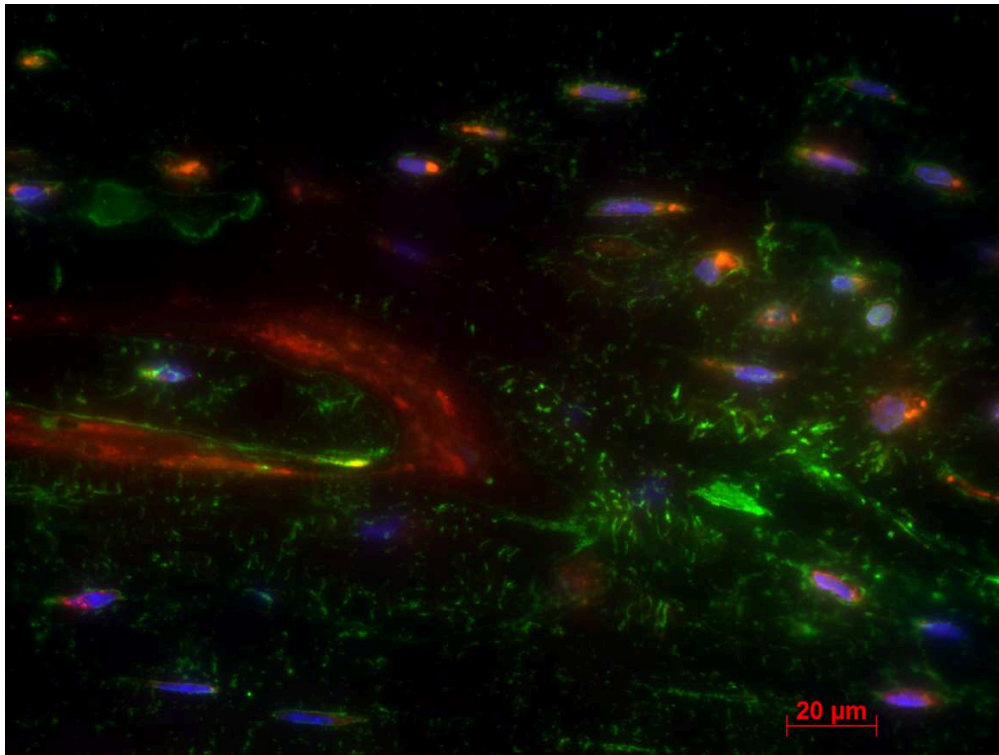


Figure 18. Fluorescent immunohistochemistry on paraffin embedded mouse femoral cortex. Oil immersed objective, x400. Sclerostin labeling (red), DMP1 labeling (green), DAPI labeling (blue). Co-localization of Sclerostin and DMP1 in yellow. Clearly visible blood vessel (left-middle part of the image) is highly positive for Sclerostin.

We also analyzed co-localization of matrix-bonded proteins Periostin and DMP1.

Interestingly, we found that Periostin was observable within cortical bone only in areas where collagen fibers seemed to be disorganized (Fig. 19A and B), and it was always associated with a diffused (not localized within LCN) DMP1 staining in the same (Fig. 16 and 17).

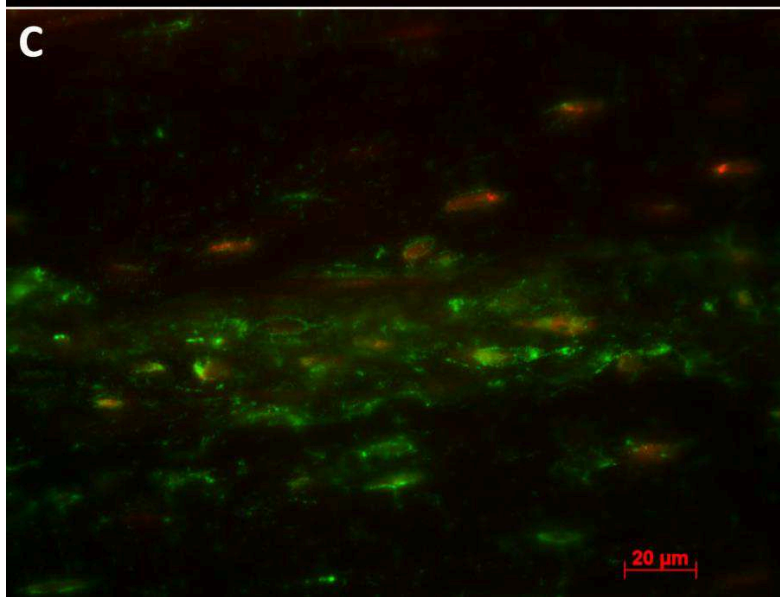
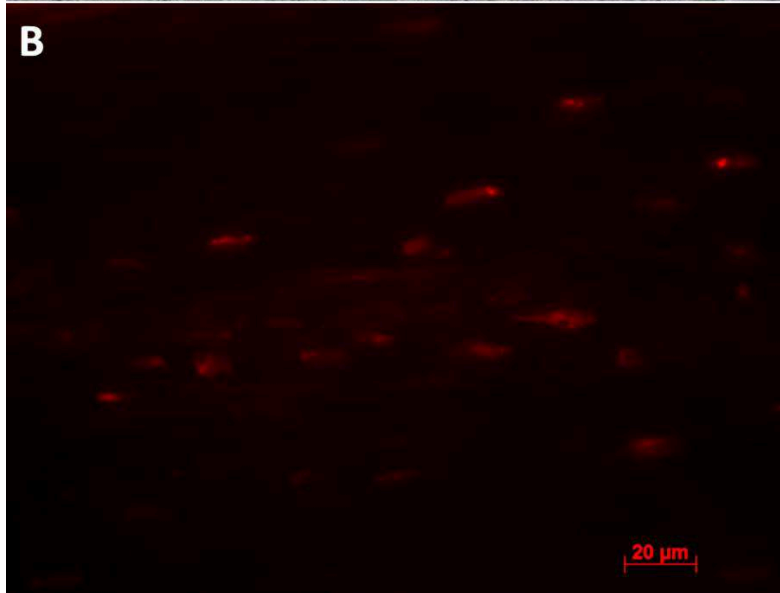
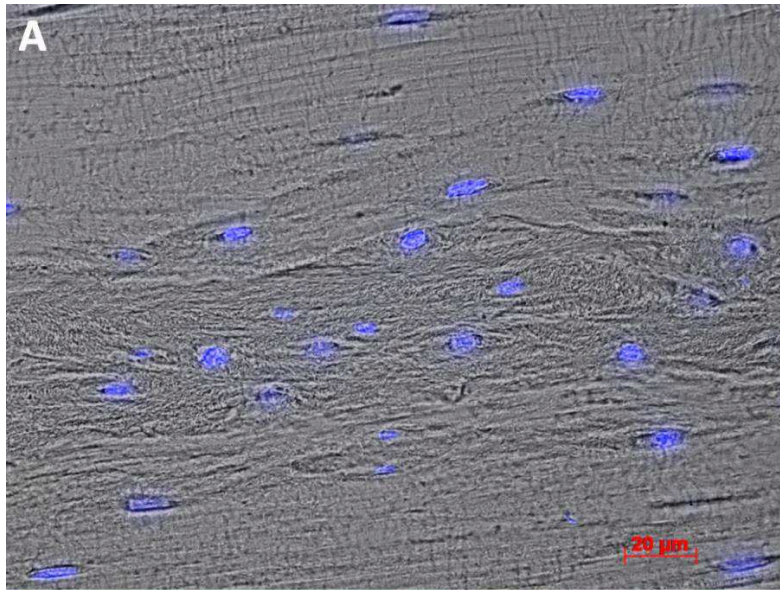


Figure 19. Fluorescent immunohistochemistry on paraffin embedded mouse femoral cortex. Oil immersed objective, x400. Periostin labeling (red), DMP1 labeling (green), DAPI labeling (blue). Co-localization of Periostin and DMP1 in yellow. Matrix-bound Periostin localized in the cortical bone has only been spotted in areas where collagen fibers were not well aligned (a,b) and Fig.14 h. Also, we noticed Periostin in such locations was always co-localized with matrix-bound DMP1 (c).

To the best of our knowledge, many teams work or have access to banks of human bone biopsies from different pathologies, which were embedded in MMA. These teams and our own would like to have a tool to perform IHC on these materials. Thus, we developed a method of fluorescent IHC for human bone biopsies embedded in MMA. The staining protocol was similar to one used for paraffin embedded mouse bones. However, some important improvements have been introduced.

Examples of single and double IHC staining for Sclerostin and DMP1 on iliac crest biopsies are on Fig. 18, Fig. 19, and Fig 20. Exact protocols of IHC on mouse and human bones are in the Supplementary data of “Osteocyte protein expression in mouse and human biopsies: optimized methods for detection and quantification” paper.

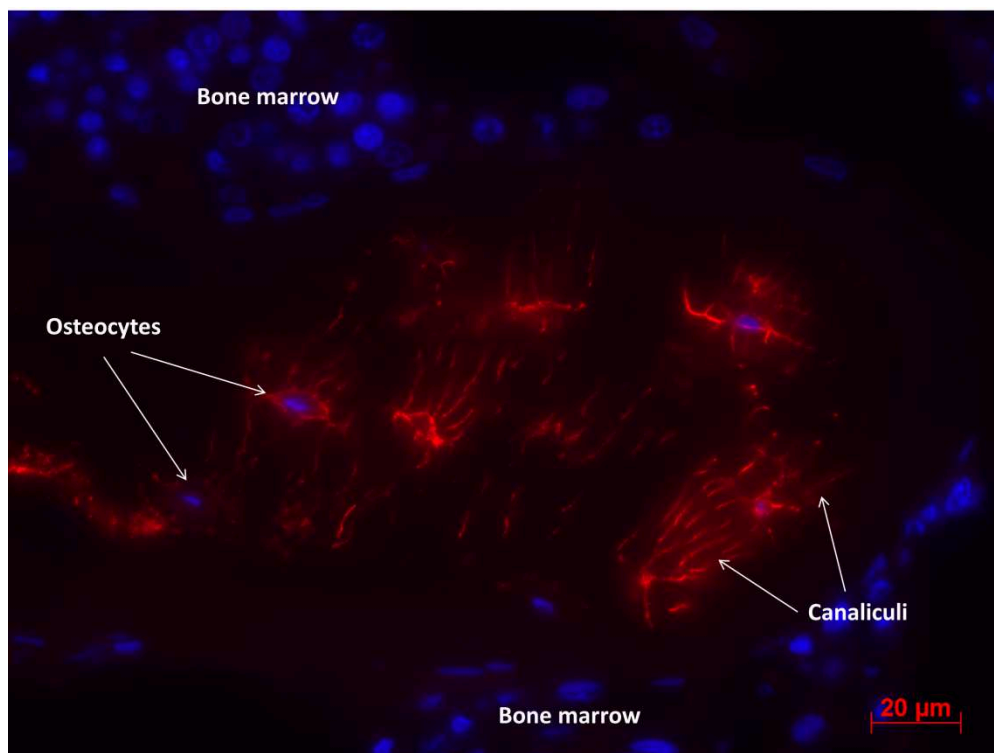


Figure 20. Fluorescent immunohistochemistry on methyl methacrylate embedded human iliac crest biopsy, trabecular bone. Oil immersed objective, x400. DMP1 labeling (red), DAPI labeling (blue).

Interestingly, osteocytes in human biopsies demonstrated specialization in relation to DMP1 or Sclerostin expressions much more often than in mouse bones. Thus, on the Fig. 21

osteocytes and canaliculae closest to the bone marrow were selectively positive for Sclerostin, and others (on the right on the image) were solely positive for DMP1.

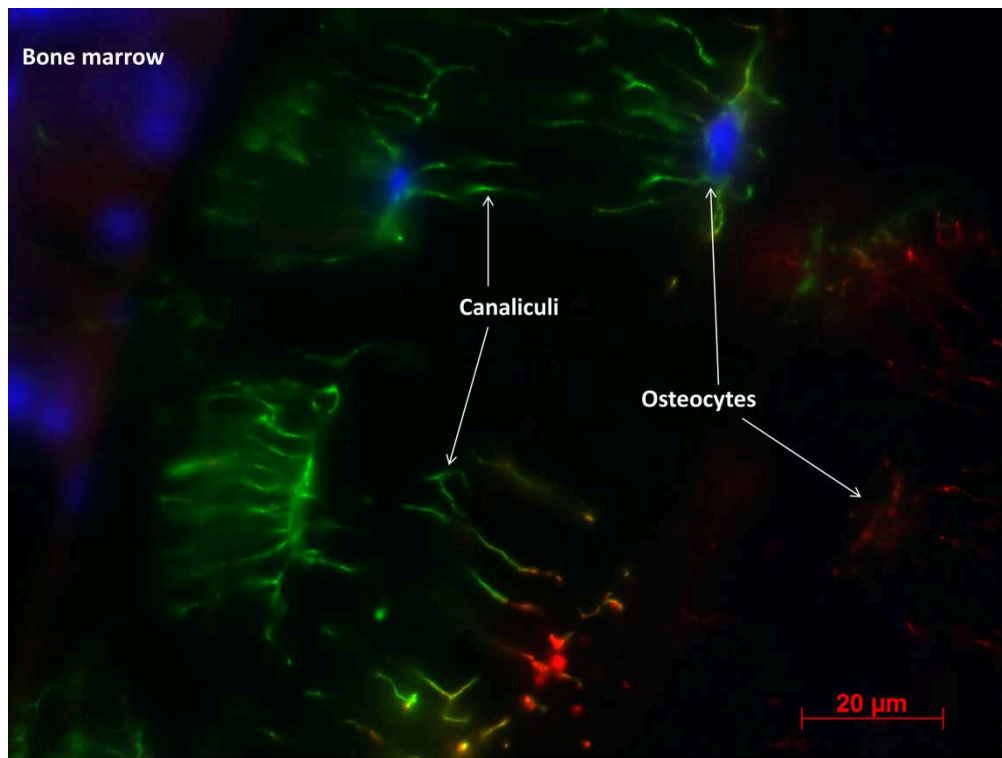


Figure 21. Fluorescent immunohistochemistry on methyl methacrylate embedded human iliac crest biopsy, cortical bone. Oil immersed objective, x630. DMP1 labeling (red), Sclerostin labeling (green), colocalization (yellow), DAPI labeling (blue).

We also observed that in human biopsies Sclerostin was much more widely spread in canalicular system compared to mouse bones (Fig. 21) and that the same canaliculi can be used for transportation of both proteins (Fig. 22).

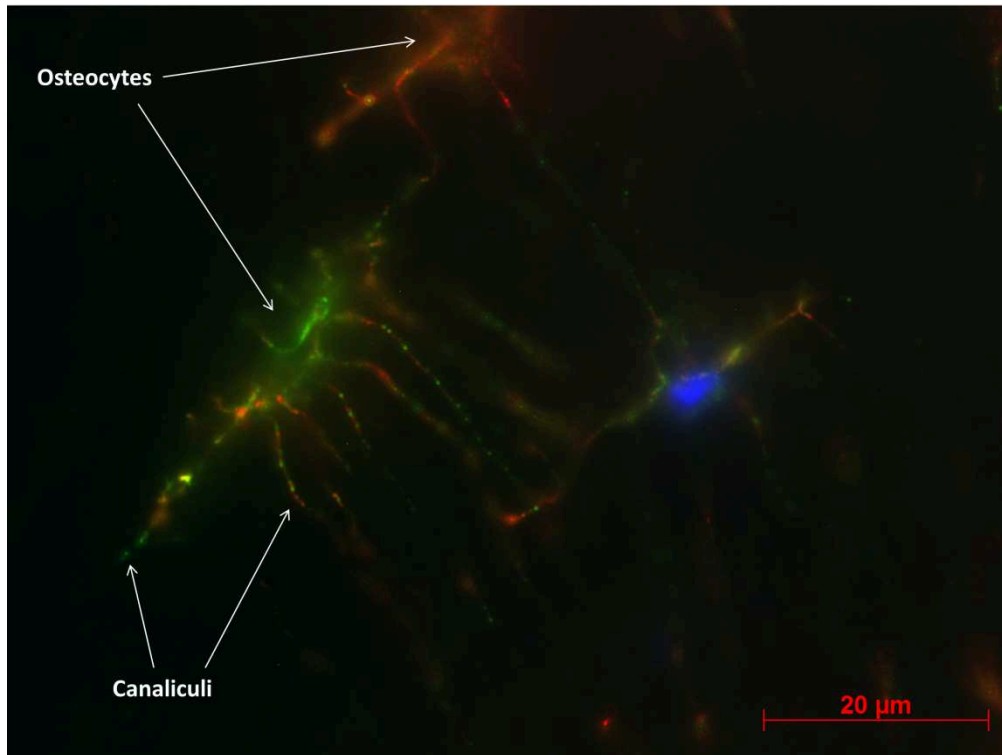


Figure 22. Fluorescent immunohistochemistry on methyl methacrylate embedded human iliac crest biopsy. Oil immersed objective, x1000. DMP1 labeling (red), Sclerostin labeling (green), co-localization (yellow), DAPI labeling (blue).

After establishing of reliable IHC protocols our next goal was to develop quantification method for osteocyte proteins. Here we propose a method based on measurements of fluorescence intensity for precise osteocyte – by – osteocyte analysis of proteins expression.

3.3.1 Paper #3: “Osteocyte protein expression in mouse and human biopsies: optimized methods for detection and quantification”

Gnyubkin V¹, Jannot M¹, Laroche N¹, de Rooij KE², Lafage-Proust MH¹, Vico L¹, Guignandon A^{1*}

¹INSERM U1059, Laboratoire de Biologie Intégrative du Tissu Osseux, University Jean Monnet, St-Etienne, France

²Department of Radiology, Leiden University Medical Center, the Netherlands and Percuros BV, Leiden, the Netherlands

*corresponding author

Key words: Immunofluorescence, cytometry, image analysis, Sclerostin, DMP1

Abstract

Osteocytes are the primary source of important proteins controlling bone remodeling such as Sclerostin and RANKL, which are potential targets for novel therapies of bone loss or mineral disorders. In vivo, production, storage and release of osteocyte proteins have complex and precise local regulations in order to satisfy changing bone physiological demands. Thus, interpretation of quantitative measurements of osteocyte proteins could be complicated with only conventional techniques such as ELISA. In this context we propose a quantitative approach for in situ measurements of osteocyte proteins by the combination of immunohistochemistry (IHC) protocols with a cell-by-cell image analysis. This method can be used for mice or human bone samples embedded in paraffin or methyl methacrylate. We found that our method can detect accurately 25% shifts in fluorescence intensity and presented a low coefficient of variation. The proposed quantification protocol can be used to analyze osteocyte proteins production in lacunae and/or canaliculae in different bone regions: endosteal, periosteal and mid-cortical. This approach is particularly adapted for revelation of subtle/physiological regulations that can't be appraised by more global measurements. The osteocyte-by-osteocyte assessment significantly increases the power of IHC measurements. This should allow developing a greater understanding of relationships between osteocyte proteins and bone and metabolism regulation.

Introduction

One of the most abundant bone cells, the osteocytes, are becoming the focus of more and more research as they are now recognized not only as key responders to mechanical loading but also as orchestrators of bone remodeling and mineral homeostasis (1). Osteocytes are postmitotic, terminally differentiated osteoblasts that during the process of matrix mineralization remain entrapped in the mineralizing matrix. One osteocyte resides in a lacuna either in the mineralized matrix or in the newly formed osteoid. Through canalicular ramifications, osteocytes are connected to each other and to cells at the bone surface. Thanks to improvements of analytical tools and techniques, the last decade has seen an exponential increase in our knowledge of osteocytes function and molecular mechanisms that govern their biology. Osteocytes are the primary source of several important proteins, which are new targets for therapies of bone loss or mineral disorders (2,3) such as Sclerostin, RANKL.

In osteocytes surrounding there is a well-established local and mechanical regulation of proteins production. Thus we suggest that local analysis of proteins is necessary in order to

link osteocytes activity to bone formation/resorption parameters, as the commonly used measurements of for example Sclerostin might poorly correlate with results of local IHC assessment (4).

Many papers, which have validated quantification IHC approaches, have used caricatured physiological challenges such as knock-out or overexpressing models for the proteins of interest, and in such situations sophisticated image analysis might not be necessary. The use of quantitative approaches is mandatory when the goal is to study physiological regulations for challenges in which protein expressions are modestly altered. In these physiological regulations a precise, accurate and objective quantification approach will be needed.

We propose an in situ cytometry approach for the quantitative fluorescent IHC in order to assess local osteocyte protein expression with a possibility to isolate signals from hundreds individual cells in different bone anatomical regions. We believe that such precise quantification may help register shifts of protein expression, especially in cases when visual comparison or manual scoring of IHC signal is difficult due to modest difference between compared samples. To illustrate our quantification technique we choose mechanosensitive osteocyte proteins Sclerostin and DMP1, as these proteins control bone formation (5,6) and mineralization (7–9).

Our method works not only on a widely used paraffin-embedded mouse bone, but also on methyl methacrylate (MMA) embedded human biopsy. We believe that it may be important for the bone research community, as despite the fact that nowadays most of the studies are done with paraffin embedded samples; there are significant stocks of MMA-embedded non-decalcified human biopsies with different pathologies. MMA is historically the resin of choice for non-decalcified human bone histology as it allows cutting of hard tissue with good preservation of structural details. Low-temperature MMA embedding (10) preserves antigens as we demonstrated that even 20-years old biopsies are suitable for IHC-F and following quantitative analysis.

Well established IHC protocol is a key for reliable quantification results as all steps from samples harvesting to image analysis are important and can affect the final result (11). However, many of the published papers do not provide precise protocols of IHC staining procedures. Additionally, in calcified tissues there are inherent difficulties in the process of preparation of histological sections for IHC due to extensive mineralization (12). Thus, in

addition to step-by-step protocols for an image analysis, here we provide step-by-step IHC protocols from tissue fixation to IHC detection for murine and human bone samples and step-by-step protocols for image analysis.

Materials and Methods

Tissue preparation and immunolabeling

Here we provide a brief description of the process. For detailed protocols one should refer to a supplementary material.

Femurs of 10 week-old male C57BL/6 mice were fixed in 10% neutral buffered formalin and then 70% ethanol. Three mm long sections of the mid-diaphysis (5 and 8 mm from the distal epiphysis) were cut out with a precision diamond wire saw (ESCIL Well, France), decalcified for 24 hours (Immunocal, Decal Chemical Corp., Ref 1440) and embedded in paraffin. Five μm thick transversal sections of the diaphysis were cut from the distal part with 250 μm increment with a microtome (Leica RM2245) and immunolabeled for Sclerostin (Primary antibody: polyclonal, goat, R&D Systems, AF1589, 1:300), and DMP1 (Primary antibody: polyclonal, rabbit, Takara, M176, 1:400). Sclerostin was detected using a biotinylated secondary polyclonal rabbit anti-goat antibody (Dako, E0466, 1:600) and Streptavidin-Alexa Fluor (Life technologies, S 11225, 1:500). DMP1 was detected using a biotin-free ready-to-use PowerFluor immunofluorescence detection kit (MaxFluor 488, MaxVision Biosciences, PF 21-M). Cell nuclei were visualized with DAPI (Santa Cruz, 28718-90-3).

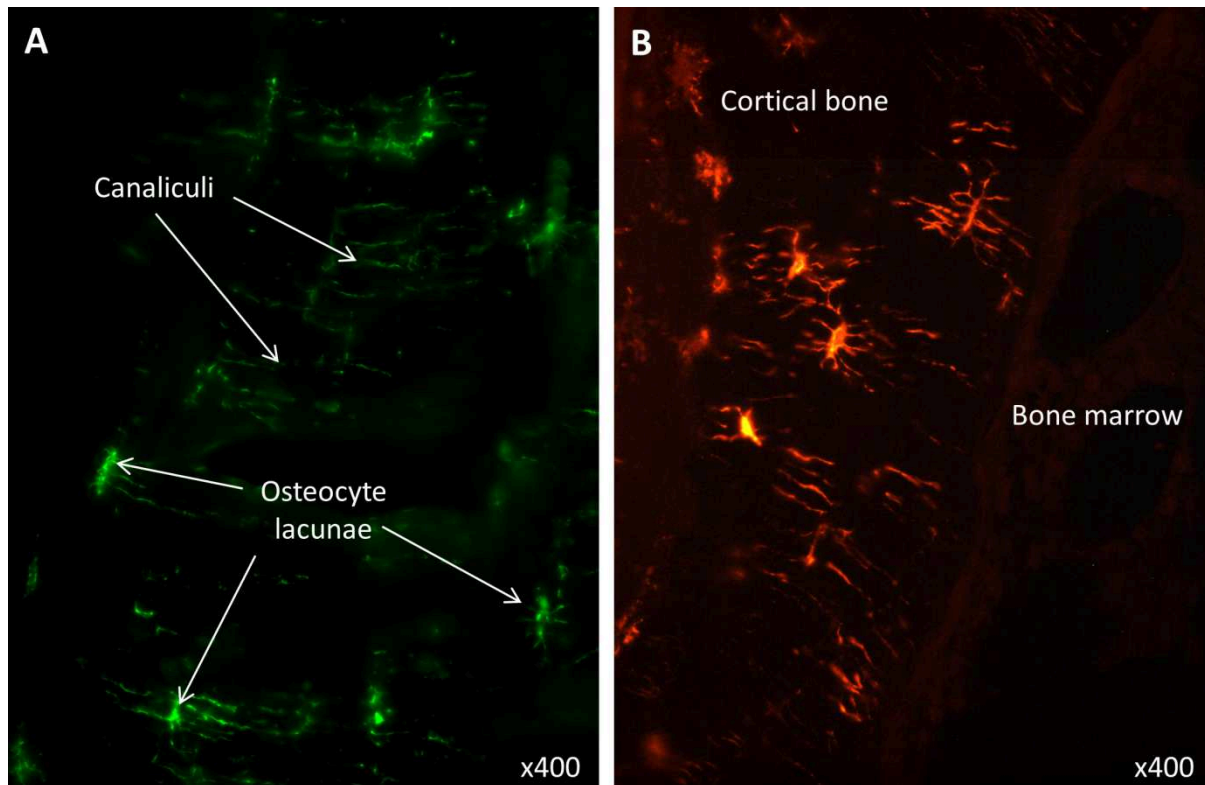


Figure 1. Immunohistochemistry on human iliac crest biopsies, methyl methacrylate embedding. A – Sclerostin; B – DMP1.

Human biopsies, trans iliac bone cores 8 mm in diameter and from 6 to 15 mm long, were harvested and fixed for 24 h in 4.5°C phosphate buffered formalin (7.35<pH<7.4; Merck,6345). After that, they were dehydrated for 24 h in absolute acetone (SDS ref: 0050516) at 4°C and embedded in methyl methacrylate. Five µm-thick sections were cut from the embedded specimens using a microtome (LEICA, SM2500E) fitted with a tungsten carbide blade and mounted on the gelatin coated slides (refer to supplementary data for detailed procedures). Bone sections were deacrylated in 2-methoxyethyl acetate (Sigma, 109886) during 3 days and decalcified for 24 hours (Immunocal, Decal Chemical Corp, 1440) Tissue was immunolabeled for Sclerostin (Primary antibody: polyclonal, rabbit, Abcam, ab63097, 1:300) and for DMP1 (monoclonal, mouse, Santa Cruz, LFMb-31, 1:100). Sclerostin and DMP1 were detected using a biotin-free ready-to-use PowerFluor immunofluorescence detection kits: MaxFluor 488, MaxVision Biosciences, PF 21-M for Sclerostin, and MaxFluor 594, MaxVision Biosciences, PF 13-S. Cell nuclei were visualized with DAPI (Santa Cruz, 28718-90-3).

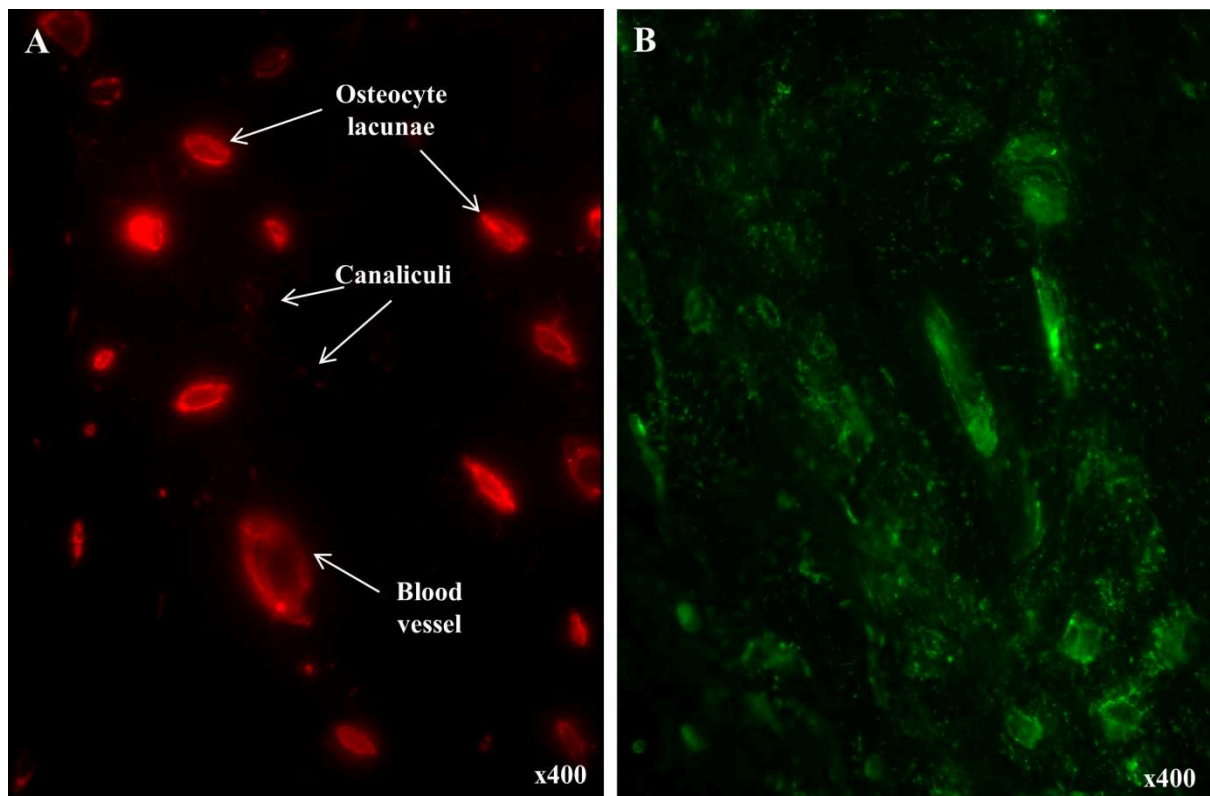


Figure 2. Immunohistochemistry on mouse femoral cortical bone, paraffin embedding. A – Sclerostin; B – DMP1.

Image acquisition for mouse cortical bone

Black and white images of the entire cortical area were obtained with an AxioObserver Z1 microscope (Zeiss, Darmstadt, Germany), at a magnification of 400 (oil immersed objective), and automatically merged using the Mosaic plugin of Axiovision 4.7 software (Zeiss). Automatic focusing on a channel specific for labeling was done on each image of the mosaic. Mosaic images of DAPI, Sclerostin and DMP1 were acquired at 50ms of exposure time for DAPI, 850ms for Sclerostin, and 400ms for DMP1. For the exposure time selection the main criteria was the absence of saturated areas in zones of the highest staining intensity. On average, the mosaic contained 7x11 images and the average size of a raw image was 400Mb. Merged mosaic images were exported in TIFF format with 0% compression from the raw images for both DAPI and labeling channels (Fig 3 and Fig 4). Mosaic images were directly analyzed with ImageJ software (<http://imagej.nih.gov/ij/>) without any brightness or contrast correction.

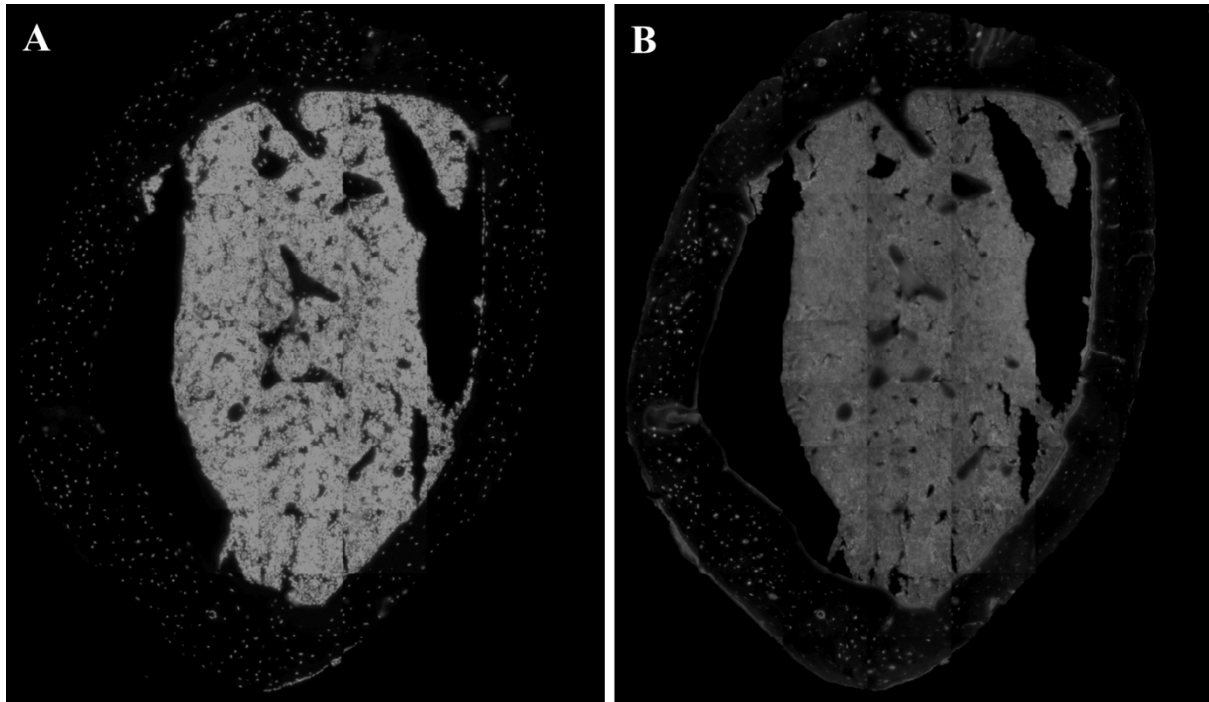


Figure 3. Mosaic composition of images of immunohistochemistry on mouse femoral cortical bone, paraffin embedding, magnification x400. A – DAPI; B – Sclerostin.

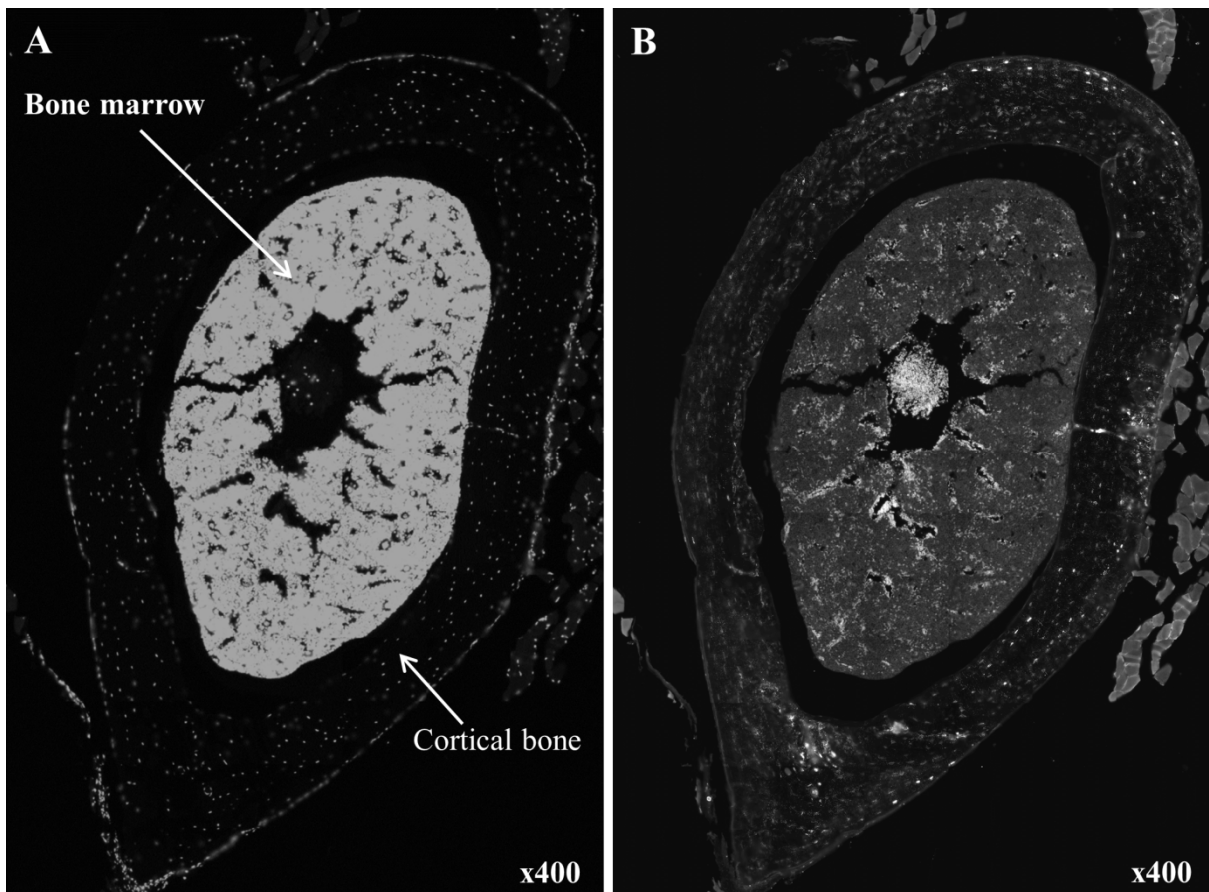


Figure 4. Mosaic composition of images of immunohistochemistry on mouse femoral cortical bone, paraffin embedding, magnification x400. A – DAPI; B – DMP1. Bone marrow, collagen and erythrocytes within blood vessels are well visible due to natural autofluorescence.

Analysis of osteocyte density, and Sclerostin or DMP1 expression on a cross-section of a cortical bone

First step was to define a region of interest (ROI) for the analysis. We used “polygon selection” function of ImageJ to draw a contour along external and internal perimeters of a cortical bone, avoiding periosteum and bone marrow as well as blood vessels and possible cutting/staining artifact (an example of a mask obtained after selection has done on Sclerostin image (Fig.3) is on Suppl Fig 1A). We used a DAPI staining to specify areas where the protein expression was measured. To obtain the DAPI map we thresholded the image (“triangle” option provides acceptable results, but for series of measurements the same thresholding values must be used) and converted to a binary format. The ROI selection was applied on DAPI binary image and two successive dilations were used in order to adjust a size of the DAPI stained nuclei to a size of osteocyte lacunae. At this step osteocyte density can be measured but an appropriate scale must be applied (“set scale” function of ImageJ). We measured the length of the same anatomical region in AxioVision in μm , and then in ImageJ in pixels; in our case $1\mu\text{m}$ was equal to 6.3 pixels. Next, the DAPI map was loaded to a ROI manager and applied to the Sclerostin or DMP1 image in order to measure the protein expression in the areas defined by the DAPI map. Measured fluorescence was saved as Excel table for analysis. Expression of a fluorescence signal as an arithmetic mean of pixels intensity has significant limitation as the staining distribution is not homogeneous in the analyzed area, therefore the mean value can be significantly lowered by unstained pixels (13). Thus, to express fluorescence intensity, instead of the mean value we used Raw Integrated Density (RawIntDens) which represents sum of all pixels intensity in selected area.

Collagen and osteocytes have a particular level of natural autofluorescence, which contributes to a total measured fluorescence level (Fig 5.). Obviously, it must be removed prior to the analysis of results. We used an approach called corrected total fluorescence to get rid of non-specific signals. In Excel we calculated the corrected fluorescence as a whole cell signal (sum of the pixels fluorescence intensity in the area) minus area in pixels multiplied by non-specific signal intensity (14). In order to get values of non-specific fluorescence a negative control bone section (a tissue, which received the same treatment but no primary antibody was applied) was measured in the same way, and a mean value of obtained RawIntDens was used for the corrected fluorescence calculation.

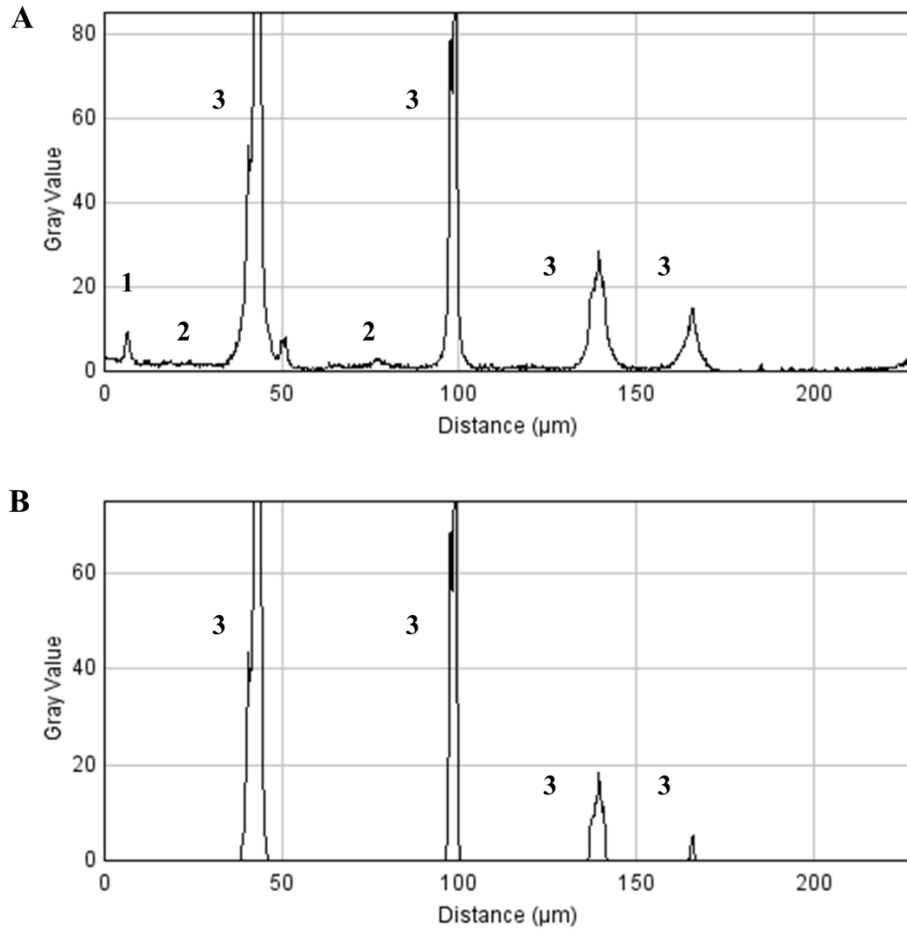


Figure 5. Justification for corrected fluorescence algorithm on example of Sclerostin immunolabeling. Level of autofluorescence on mouse cortical bone tissue. A – before non-specific fluorescence removal. B – after non-specific fluorescence removal. 1 – negative osteocyte; 2 – collagen; 3 – positive osteocytes.

Analysis of osteocyte proteins expression on different anatomical regions of a cortical bone

We observed that IHC staining is not equally distributed within cortical surface (Fig.3). Thus, we applied a mathematical model to isolate three different regions: endosteal, periosteal and mid-cortical bone in order to independently quantify protein expression there (Fig.6). We used a distance map on a mask of a cortical bone. By thresholding of the distance map we obtained three masks for endosteal, periosteal and mid-cortical areas (Suppl Fig 1). Next, these masks were applied on DAPI map, and then on Sclerostin or DMP1 staining images.

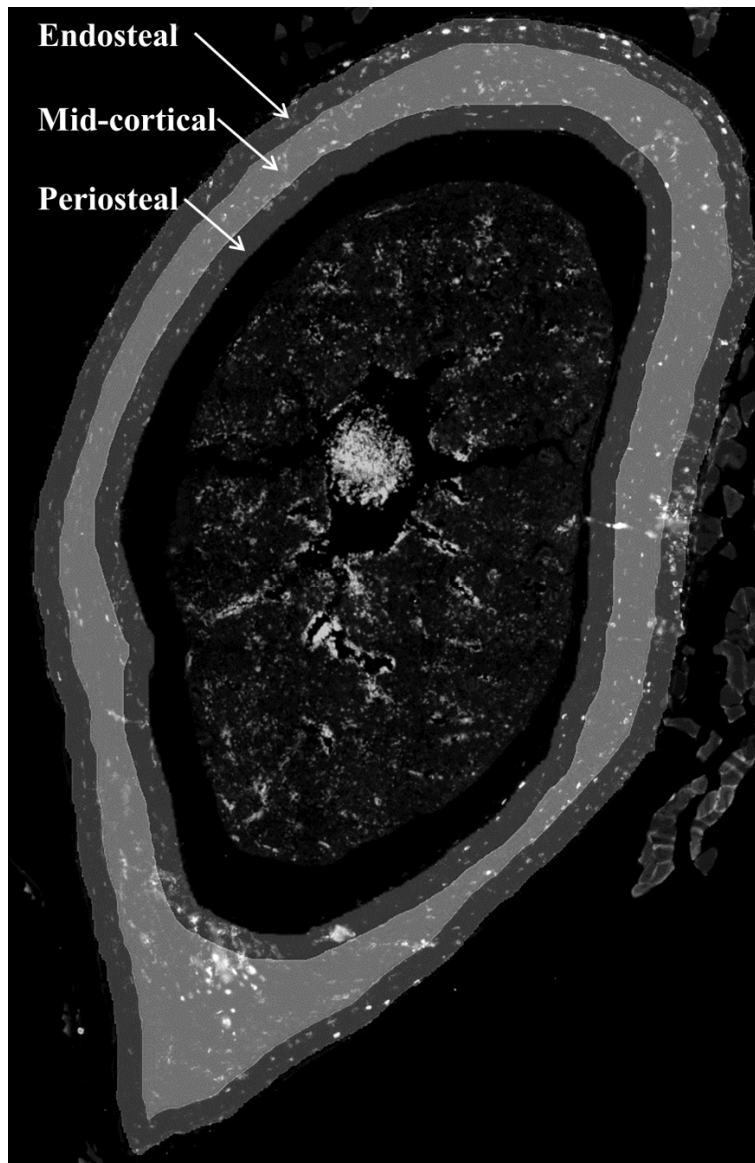


Figure 6. Example of anatomical regions restriction for mouse cortical bone on DMP1 immunolabeling; top – lateral internal, bottom – lateral external, right – anterior, left – posterior.

Analysis of osteocyte proteins expression within osteocyte regions of influence

There was a clear difference in staining patterns between Sclerostin and DMP1 in mouse cortical bone. While Sclerostin was mostly observable inside lacunar area, DMP1 was located not only around osteocytes but extensively distributed in a canalicular system and bone matrix (Fig 1 and Fig 2). However, to analyze lacunar and canalicular DMP1 expression we needed to define areas where the staining intensity is measured. We used Voronoi diagram of the DAPI mask to generate polygon-shaped selections for ROI manager, where each polygon contained one generating point (based on DAPI), and every point of a polygon was closer to its DAPI than to any other (Fig. 7). We called these polygons as osteocyte regions of

influence. Analysis based on the Voronoi diagram was also performed on three anatomical regions as described above. Importantly, for the calculation of corrected total fluorescence, a mean RawIntDens value of non-specific fluorescence should be measured using Voronoi diagram on a negative control bone section.

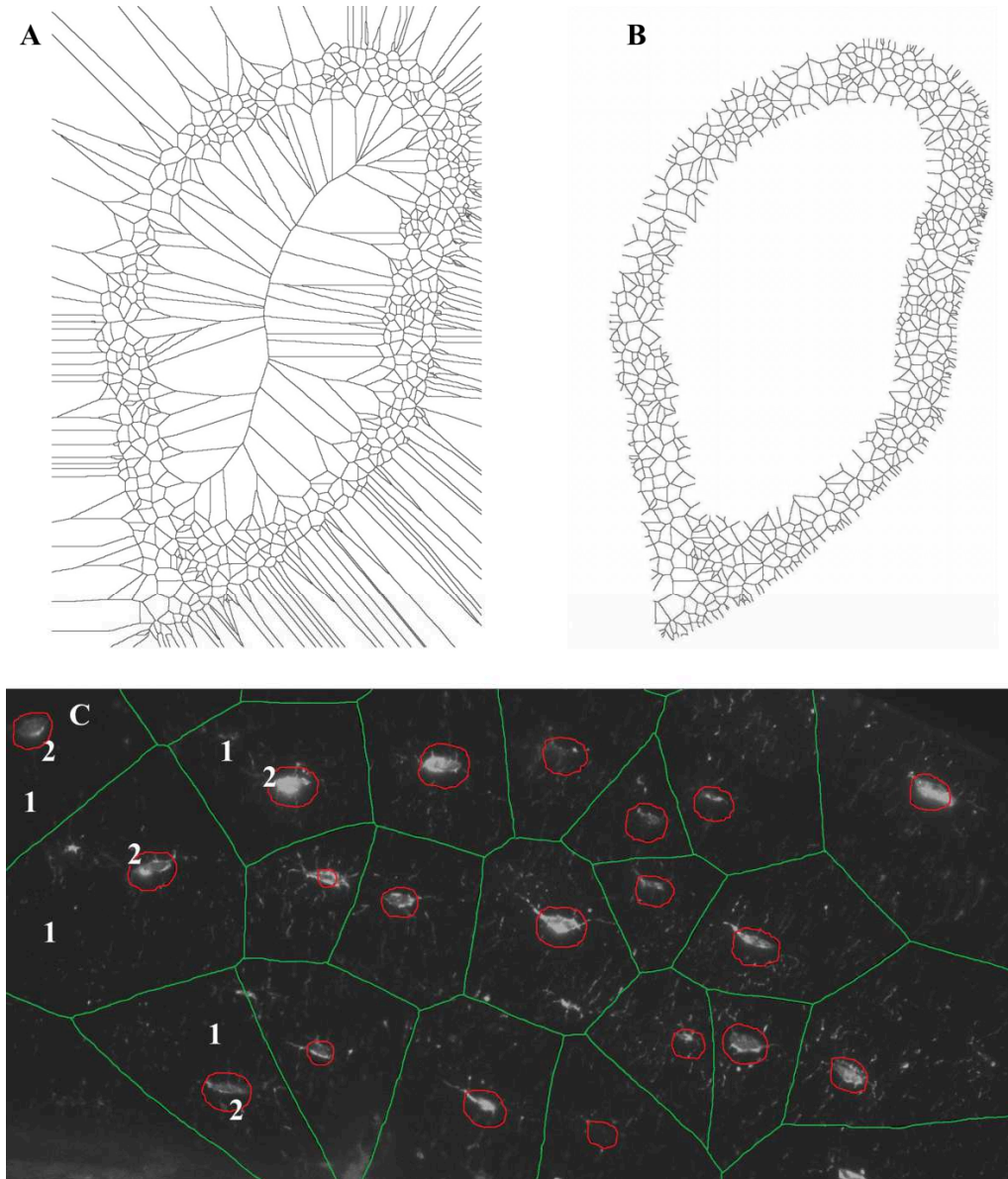


Figure 7. Areas for fluorescence measurements based on Voronoi diagram. A – raw Voronoi diagram, B – Voronoi diagram adjusted to cortical bone, C – difference between areas isolated by Voronoi diagram (1, in green) and DAPI map (2, in red).

Image Acquisition for Human Iliac crest biopsies

Black and white images of human iliac crest biopsies were obtained with the same microscope and magnification as for mouse bones. Focusing was manual for each channel. Images of DAPI, Sclerostin and DMP1 were acquired at 65ms of exposure time for DAPI, 400ms for Sclerostin, and 550ms for DMP1. In addition, a bright field image was acquired.

For human biopsies we could not use the same approach as for mouse cortical bone as a surface of a human biopsy was considerably larger. Thus, instead of a total mosaic image it was necessary to select particular areas for analysis. We believe that our quantification method could be used for analysis and comparison of proteins expression in a variety of bone pathologies. Hence, as a personal decision of an operator was involved in an area selection process, we proposed a method of a blind ROI selection to limit potential bias in comparison of different bone samples. According to our protocol, an operator had to decide based only on histological/cellular information from a bright field and DAPI channels, which area is a subject for analysis, thus an operator had no information of staining intensity of osteocytes in the acquired image.

Analysis of osteocyte Sclerostin or DMP1 expression on human biopsies

Quantification of fluorescence intensity on human biopsies required a particular approach of ROI selection due to abundant DAPI negative osteocytes, and higher canalicular (Sclerostin) and matrix (DMP1) IHC staining compared to mouse bone samples. Osteocytes were manually identified on a merged bright field, DAPI and IHC labeling images (Fig.8A, Fig. 9A). Locations of osteocytes were pointed with a Paintbrush tool of ImageJ (brush width = 50). Then the image was thresholded, and binarized. We tried two approaches: Voronoi diagram (Fig.8D, Fig 9D) and osteocyte map with 80 consecutive dilations (Process-Binary-Options, Iterations = 80, Process-Binary-Dilate, Process-Binary-Watershed) in order to restrict measurements to osteocyte lacunae and surrounding matrix (Fig.8E, Fig.9E). Prior to measurements, on an IHC staining image we selected an area where we perform measurements. With the selection we avoided blood vessels and cutting or staining artifacts. To obtain a value of non-specific fluorescence we used the same method of osteocytes identification on a negative control sample.

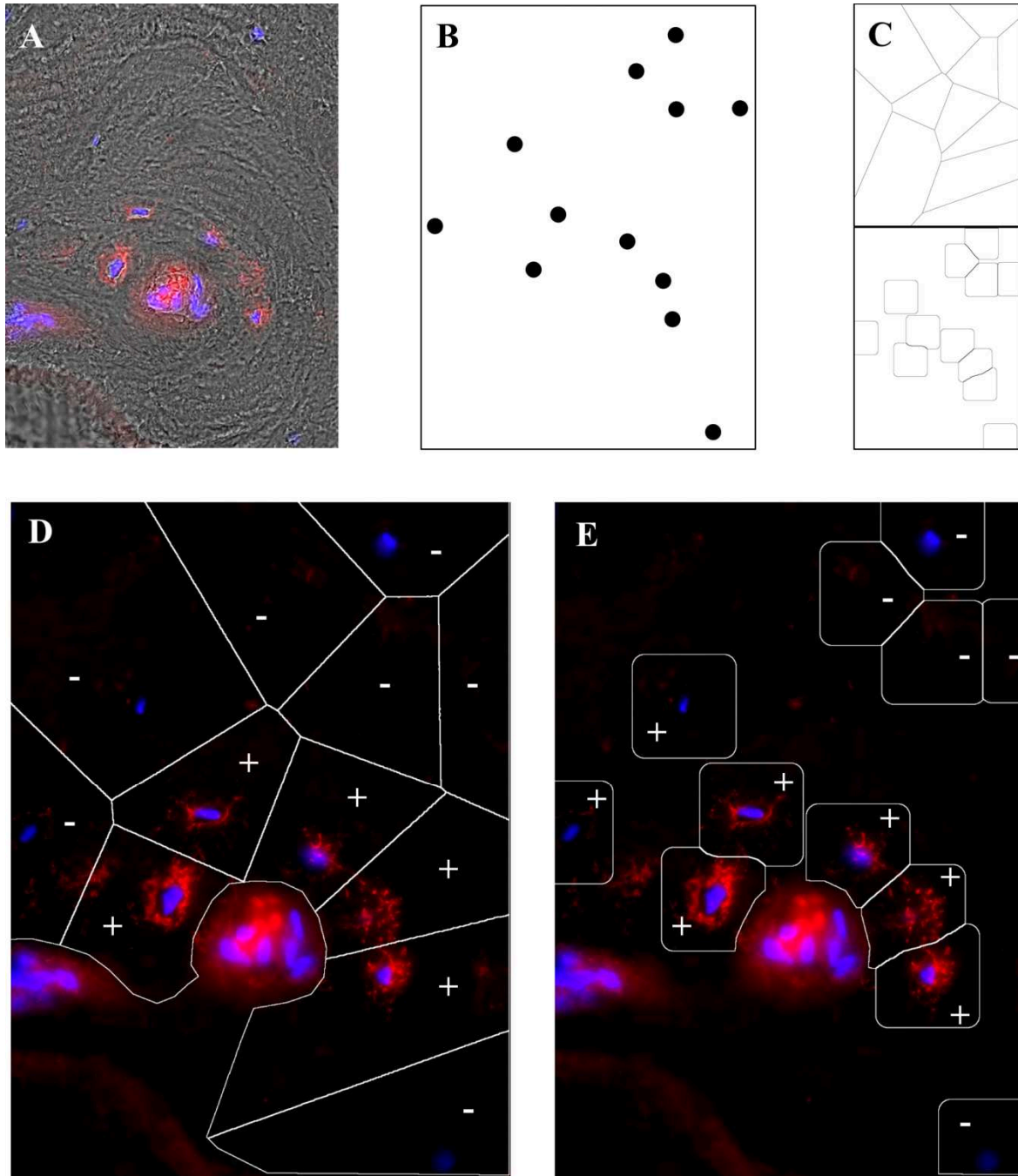


Figure 8. Analysis of DMP1 immunolabeling on human biopsies. A – merged image DMP1, DAPI, and brightfield channels for creation of an osteocyte map; B – osteocyte map; C – isolation of areas for measurements by Voronoi diagram (top) or by dilated osteocyte map (bottom); D – merged image of DMP1, DAPI and areas for measurements based on Voronoi diagram; E - merged image of DMP1, DAPI and areas for measurements based on dilated osteocyte map; (+) – positive osteocytes; (-) – negative osteocytes.

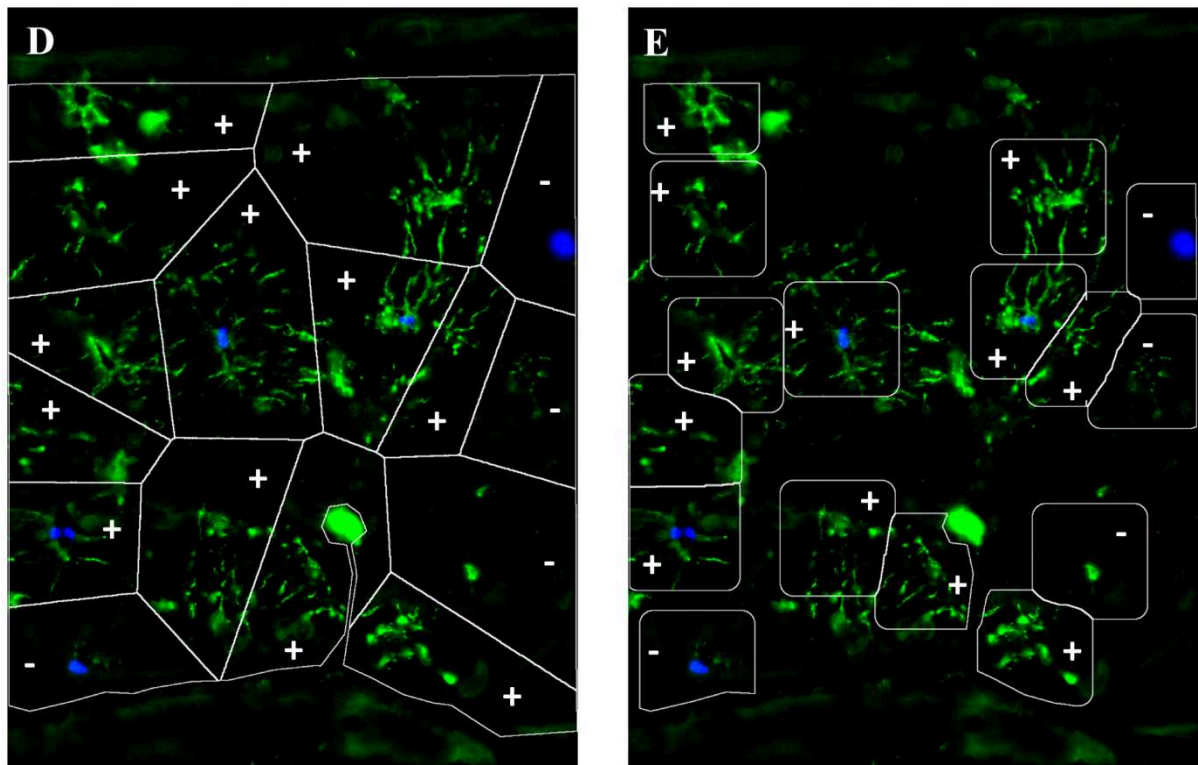
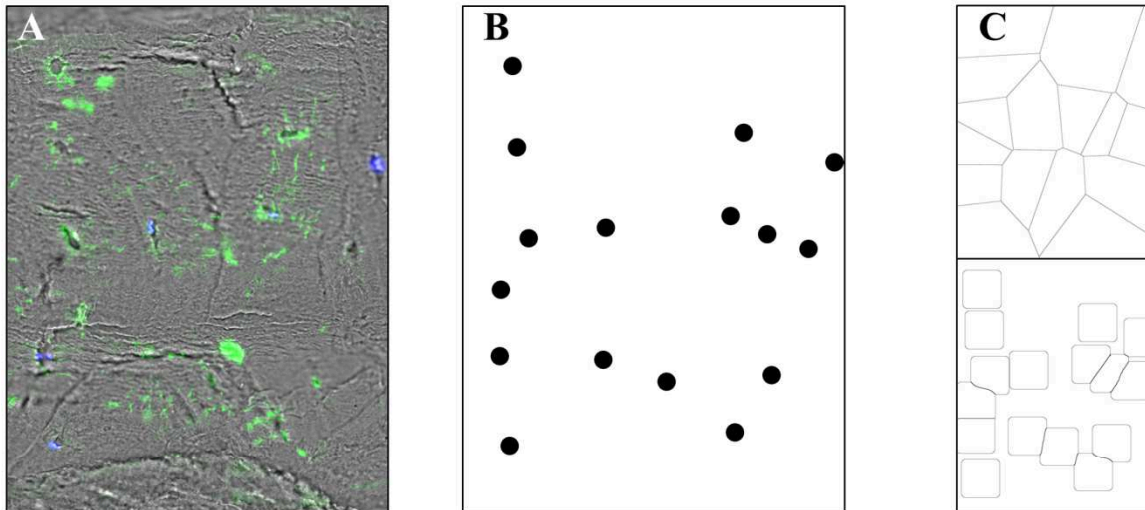


Figure 9. Analysis of Sclerostin immunolabeling on human biopsies. A – merged image DMP1, DAPI, and brightfield channels for creation of an osteocyte map; B – osteocyte map; C – isolation of areas for measurements by Voronoi diagram (top) or by dilated osteocyte map (bottom); D – merged image of DMP1, DAPI and areas for measurements based on Voronoi diagram; E - merged image of DMP1, DAPI and areas for measurements based on dilated osteocyte map; (+) – positive osteocytes; (-) – negative osteocytes.

Calculation of coefficient of variation

To calculate coefficient of variation three non-trained operators had to analyze independently the mouse cortical bone image with Sclerostin IHC labeling. They had to perform relevant measurements using DAPI map on a total cortical bone, from ROI selection to Excel

calculations of corrected fluorescence. Measurements were repeated fifteen times for each operator. Medians of RawIntDens values were compared.

Verification of quantification method sensitivity

As we had no chance to analyze biological samples from animals subjected to some kind of physiological or pharmacological challenges, we artificially mimicked a physiological challenge by altering Sclerostin expression level as it might happen as a result of the experiment. In order to do this, we used ImageJ function (Process-Math- Multiply by 0.75) to reduce fluorescence of selected areas by 25%. We applied such “challenge” on total cortical bone and then endosteal part. Next, we imitated an increase of Sclerostin expression on total cortical bone area and on periosteal area by 25%, with another ImageJ function (Process-Math-Multiply by 1.25). Level of non-specific fluorescence was reduced or increased by 25% respectively. We used DAPI map to measure Sclerostin expression values, which were compared with non-parametric Mann-Whitney U-test to values of the original image. We selected 25% shift in order to demonstrate that this difference is not obvious (Suppl Fig. 2) and without quantitative analysis such alteration in protein expression can be missed.

Also, to access the accuracy of the method, three operators five times independently performed analysis, starting from total cortical ROI selection, of the same images with IHC Sclerostin lowered by 25%, a control image (unchanged), and increased by 25%. DAPI map was used, and total cortical bone was analyzed (See chapter Analysis of osteocyte density, and Sclerostin or DMP1 expression on a cross-section of a cortical bone).

Results

Analysis of osteocyte density in mouse cortical bone

Osteocyte density calculated from the 2 DAPI images, corresponding to the Sclerostin and DMP1 IHC labeling (Fig.3 and 4), was 0.83 ± 0.01 , $1/1000\mu\text{m}^2$. Assessment of this parameter might have interest for researchers from a relevant field as it is altered by ageing or osteoporotic conditions (15).

Analysis of Sclerostin expression in mouse cortical bone

As most of the IHC labeling was observed within or very close to osteocytes lacunae, we used DAPI map in order to measure peri-lacunar Sclerostin expression. Two different methods were applied. Firstly, we assessed osteocytes of the total cortical bone. After correction of total fluorescence we found that only 66.2% of osteocytes were Sclerostin-positive, which is close to what was previously observed in mice (16), with a median RawIntDens of 3109. As we already noted, the distribution of Sclerostin seemed to be not homogeneous on the cortical area (Fig 3). Therefore, secondly, we performed analysis restricted to anatomical regions (Supplementary Figure 1) which revealed significant difference between mid-cortical (n osteocytes = 342; 64% of them were positive) and endosteal (n osteocytes = 115; 49% of them were positive) or periosteal bones (n osteocytes = 208; 63% of them were positive) (Fig. 10A).

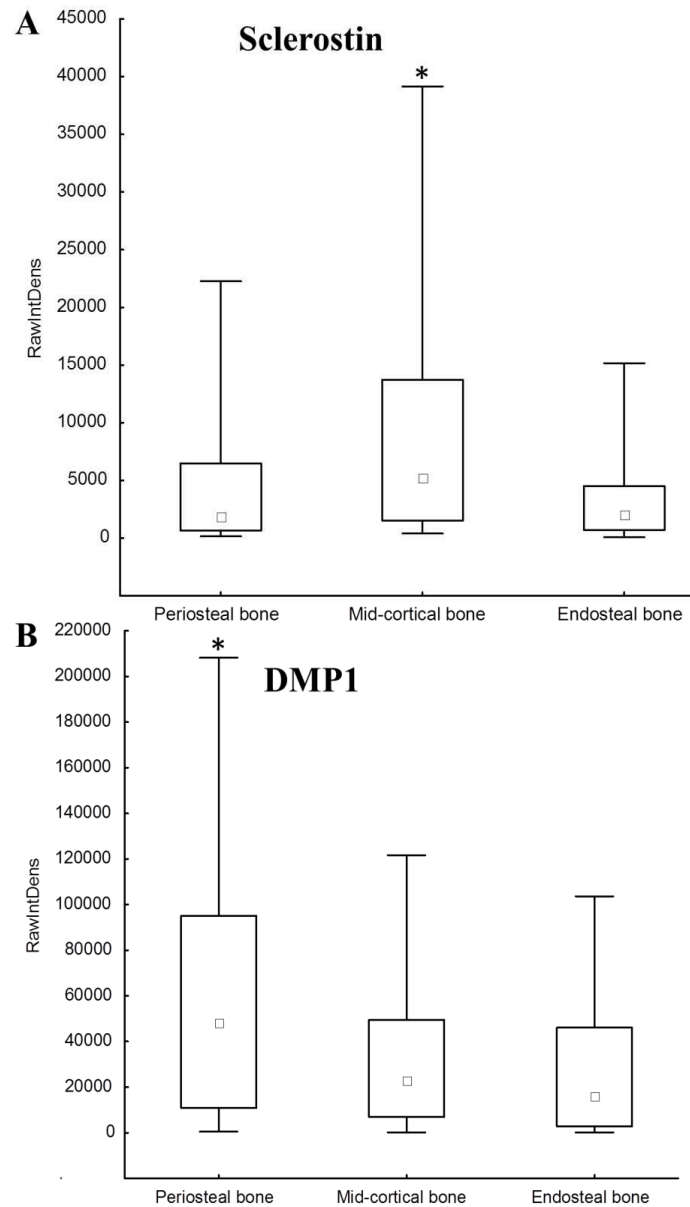


Figure 10. Distribution of protein expression within different anatomical regions of mouse cortical bone (endosteal, mid-cortical, and periosteal). A – expression of Sclerostin in the mid-cortical bone is significantly higher than in endosteal or periosteal bones ($p=0.0001$); B expression of DMP1 in the periosteal bone is significantly higher than in mid-cortical or endosteal bones ($p=0.0001$). Boxes represent 50% of values (25% to 75%), whiskers represent minimum and maximum values, middle point represents median. Non-parametric Kruskal-Wallis ANOVA test followed by post-hoc Mann-Whitney U-tests with Bonferroni correction

Analysis of DMP1 expression in mouse cortical bone

As DMP1 labeling demonstrated that the protein was vastly presented in the whole lacunar - canalicular system, the use of the same peri-lacunar quantification approach as for Sclerostin was not justified. Using Voronoi diagram we calculated DMP1 expression in osteocyte regions of influence. We found that on a total cortical bone 97.7% of these regions were positive for DMP1 with a median RawIntDens of 23353. After restricting measurements to the three anatomical regions, we observed that DMP1 expression was significantly higher in

the periosteal region (n regions = 228; 98.2% of them were positive) than in mid-cortical (n regions = 588; 97.7% of them were positive) or in endosteal (n regions = 216; 91.2% of them were positive) parts (Fig. 10B). Number of regions for fluorescence measurements was higher with Voronoi diagram than number of osteocytes defined by DAPI map, as some regions restricted by Voronoi diagram were in between of different anatomical regions.

Importantly, the use of Voronoi diagram to calculate Sclerostin was not appropriate. The measurements were done on a larger areas compared to DAPI restricted zones, thus there were many pixels with low values of gray level. And as a calculation of corrected fluorescence depends on the area of measurement, it so dramatically lowered our results, that only 35% of analyzed regions remained positive. Therefore, the location of the protein of interest dictates which type of mask should be used.

Analysis of DMP1 and Sclerostin expression in human biopsies

We believe that such approach allows researchers to bring quantitative data to usually subjective interpretation of IHC results, and dramatically multiply amount of generated data as compared to methods of measurements of mean of image total fluorescence. As we mentioned above, selection of quantification method depends on distribution of protein of interest in the tissue.

We found that the use of Voronoi diagram was appropriate only for Sclerostin IHC labeling but not DMP1. As it is illustrated on Fig. 8D, Voronoi diagram covered broad unstained areas on the DMP1 IHC image, which resulted in low corrected fluorescence and only five positive osteocytes were detected. We observed a similar trend when Voronoi diagram was used for Sclerostin measurements on mice cortical bone. Thus, we decided to use dilated osteocyte map (Fig. 8B and C) to cover specifically lacunae and surrounding matrix (Fig. 8E), which limited areas of analysis. It allowed us to identify more osteocytes as positive (7 out of 12).

It was observed that Voronoi diagram was useful for Sclerostin IHC (Fig. 9D): as the labeling was broadly distributed in canalicular network, number of positive osteocytes assessed with Voronoi (Fig. 9D) or dilated osteocyte map (Fig.9E) was equal (12 out of 16); but almost all Sclerostin labeled areas were taken into account only with Voronoi diagram.

Calculation of coefficient of variation

Interpersonal coefficient of variation was 5.8% (mean for three operators) and 6.5% intrapersonal (mean for three operators). We concluded that despite some manual operations and necessity of personal decision for ROI selection, our technique is reasonably reproducible.

Verification of quantification method accuracy and sensitivity

Assessment of method accuracy by analysis of total cortical bone images with intensities modified by 25%, showed that our quantification technique was able to detect shifts as 24.3% \pm 2.4 (comparison of medians, mean and SD of 35 measurements).

Assessment of modified by 25% endosteal and periosteal regions detected alterations of fluorescence intensity of 23.7% for endosteal and 24.4% for periosteal region. However, these changes were not statistically significant (non-parametric Mann-Whitney U-test) due to relatively low number of analyzed osteocytes per image (57 positive osteocytes in endosteal, and 132 in periosteal). When we compared mid-cortical bone areas, we observed that the detected shift of 24.5% was statistically significant ($p=0.01$) as 396 osteocytes per image were included into analysis. These findings emphasize that high number of measurements obtained from individual osteocytes is needed in order to detect even modest shifts of protein expression and to validate it with the statistical test.

Discussion

Immunohistochemistry is a widely used analytical tool, which combines advantages of *in situ* localization of specific antigens and a tissue histological assessment. Besides qualitative analysis, many attempts were done to bring a quantitative part in it. A recent reviews revealed hundreds of different quantification approaches for IHC labeling in histopathology and biology (17,18). Most of the reviewed papers used scoring systems widely accepted in histopathology semiquantitative (19) to derive quantitative data from biological tissues for statistical analysis. Such systems are well described in a review of Fedchenko et al (17) and they are generally based on two parameters: staining intensity and a percentage of tissue that is stained or staining pattern (20). However manual assignment of scores is based by subjective, purely visual inspection of IHC labeling by an experienced pathologist (20,21) and a non-experienced observer may introduce bias at any stage of evaluation process. Considering limitations linked to the subjectivity of IHC labeling interpretation, sophisticated

automated approaches based on image analysis have been developed (21–27). These methods well replicate manual scoring by pathologists (21) and generally they work with area-related evaluation of an IHC image staining intensity by color deconvolution and isolation of individual stains. One of the disadvantages of automated staining evaluation is that it may not be possible to work on a level of individual cells. Thus, a new approach offered a possibility to distinguish individual cells with hematoxylin nuclear staining, and quantify cellular IHC signals (23), similar to techniques of single cell quantification that are used in flow-cytometry (13,28). In addition, a quantitative IHC can be a reliable alternative to the enzyme-linked immunosorbent assay (29), and it has been shown to be highly comparable with a method of fluorescence in situ hybridization (29).

Despite variety of existing techniques, to the best of our knowledge there is no quantification tool adapted for IHC analysis of osteocytes. Thus, our goal was to create a method dedicated primarily for semi-automatic quantitative assessment of IHC signal in osteocytes, which can be routinely applied in research laboratories without necessity to use uncommon hardware or expensive software.

Image analysis are generally based on quantification of level of fluorescence of entire images (field of interest) implying that an important number of images has to be analyzed for statistical discrimination. In line with quantitative measurements based on flow-cytometry where individual cells are analyzed, we proposed a quantitative histological approach based on a cell by cell quantification in order to significantly increase the number of analyzed events for adequate statistical discrimination. Such local and DAPI-based approach can be particularly useful to highlight alterations of Sclerostin expression in a certain bone region, as for example, in a cycling loading model (15).

In addition, analysis of other biochemical markers of bone turnover, such as osteocalcin, bone-specific alkaline phosphatase, and tartrate-resistant acid phosphatase isoform 5b, whose concentrations are generally measured in serum, might be assessed in local bone environment with respect to different bone envelopes, at least in rodents. We believe our investigation tool might reveal clinically and scientifically relevant information helping interpret obtained data.

Conclusion

We proposed a novel method using well known analytical tools: IHC and ImageJ. Our protocols can be easily used as they do not require sophisticated and expensive imaging hardware or software. This approach is particularly adapted for revelation of subtle physiological regulations of osteocyte protein expression. The local (endosteal/periosteal) and cell by cell measurements increase significantly the power of analysis and we hope that many unexplained or unfound relationships between osteocyte proteins and bone physiology will be revealed with our quantification technique.

References

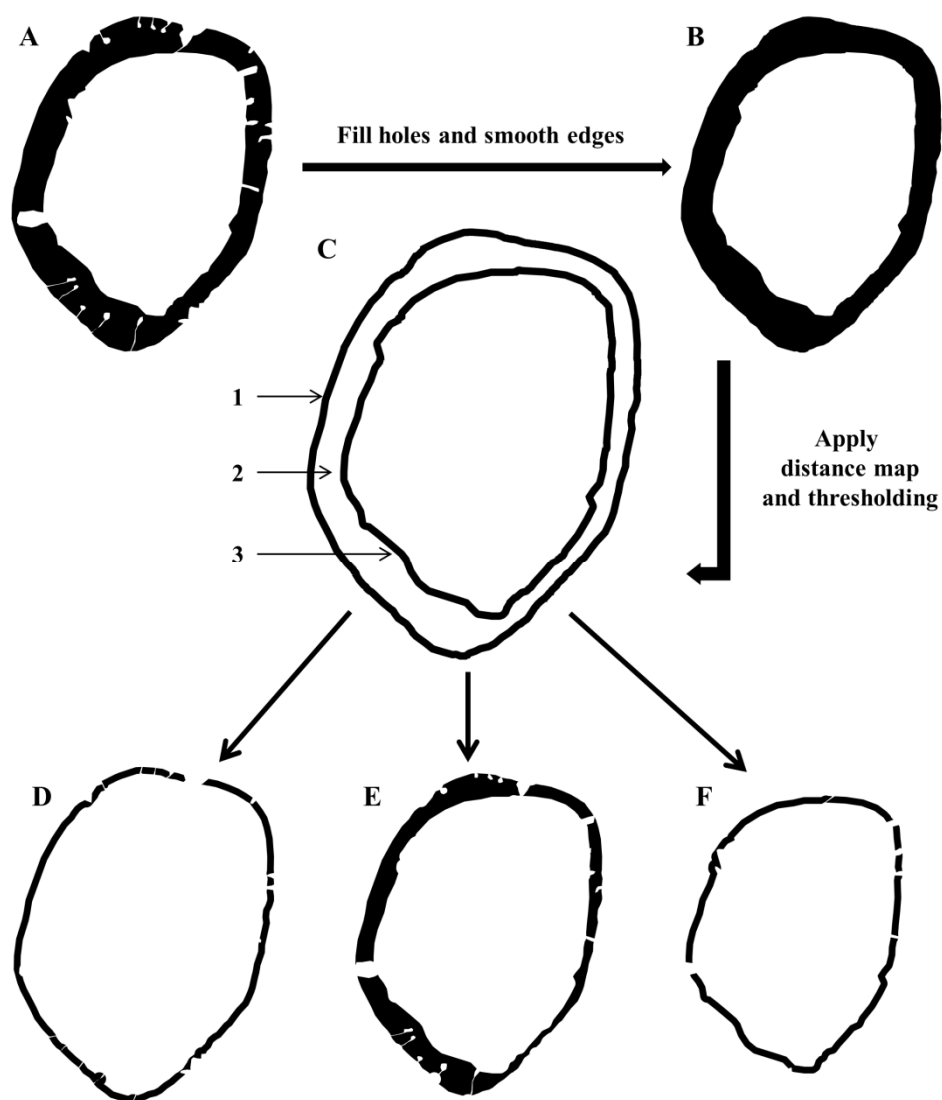
1. Bonewald LF. The amazing osteocyte. *J Bone Miner Res.* 2011 Feb;26(2):229–38.
2. Compton JT, Lee FY. A Review of Osteocyte Function and the Emerging Importance of Sclerostin. *J Bone Jt Surg.* 2014 Oct 1;96(19):1659–68.
3. Martin TJ. Bone biology and anabolic therapies for bone: current status and future prospects. *J Bone Metab.* 2014 Feb;21(1):8–20.
4. Lin C, Jiang X, Dai Z, Guo X, Weng T, Wang J, et al. Sclerostin mediates bone response to mechanical unloading through antagonizing Wnt/beta-catenin signaling. *J Bone Miner Res.* 2009 Oct;24(10):1651–61.
5. Li X, Zhang Y, Kang H, Liu W, Liu P, Zhang J, et al. Sclerostin binds to LRP5/6 and antagonizes canonical Wnt signaling. *J Biol Chem.* 2005 May 20;280(20):19883–7.
6. Feng JQ, Ward LM, Liu S, Lu Y, Xie Y, Yuan B, et al. Loss of DMP1 causes rickets and osteomalacia and identifies a role for osteocytes in mineral metabolism. *Nat Genet.* 2006 Nov;38(11):1310–5.
7. Ling Y, Rios HF, Myers ER, Lu Y, Feng JQ, Boskey AL. DMP1 depletion decreases bone mineralization in vivo: an FTIR imaging analysis. *J Bone Miner Res.* 2005 Dec;20(12):2169–77.
8. Maciejewska I, Qin D, Huang B, Sun Y, Mues G, Svoboda K, et al. Distinct compartmentalization of dentin matrix protein 1 fragments in mineralized tissues and cells. *Cells Tissues Organs.* 2009;189(1-4):186–91.
9. Chappard D, Palle S, Alexandre C, Vico L, Riffat G. Bone embedding in pure methyl methacrylate at low temperature preserves enzyme activities. *Acta Histochem.* 1987;81(2):183–90.

10. Grube D. Constants and variables in immunohistochemistry. *Arch Histol Cytol.* 2004;67(2):115–34.
11. Wittenburg G, Volkel C, Mai R, Lauer G. Immunohistochemical comparison of differentiation markers on paraffin and plastic embedded human bone samples. *J Physiol Pharmacol.* 2009 Dec;60 Suppl 8:43–9.
12. Ecker RC, Rogojanu R, Streit M, Oesterreicher K, Steiner GE. An improved method for discrimination of cell populations in tissue sections using microscopy-based multicolor tissue cytometry. *Cytometry A.* 2006 Mar 1;69A(3):119–23.
13. Gavet O, Pines J. Progressive activation of CyclinB1-Cdk1 coordinates entry to mitosis. *Dev Cell.* 2010 Apr 20;18(4):533–43.
14. Mullender MG, van der Meer DD, Huiskes R, Lips P. Osteocyte density changes in aging and osteoporosis. *Bone.* 1996 Feb;18(2):109–13.
15. Robling AG, Niziolek PJ, Baldrige LA, Condon KW, Allen MR, Alam I, et al. Mechanical stimulation of bone in vivo reduces osteocyte expression of Sost/sclerostin. *J Biol Chem.* 2008 Feb 29;283(9):5866–75.
16. Fedchenko N, Reifenrath J. Different approaches for interpretation and reporting of immunohistochemistry analysis results in the bone tissue – a review. *Diagn Pathol.* 2014 Nov 29;9(1):221.
17. Klopfleisch R. Multiparametric and semiquantitative scoring systems for the evaluation of mouse model histopathology-a systematic review. *BMC Vet Res.* 2013;9:123.
18. Gibson-Corley KN, Olivier AK, Meyerholz DK. Principles for valid histopathologic scoring in research. *Vet Pathol.* 2013 Nov;50(6).
19. Choudhury KR, Yagle KJ, Swanson PE, Krohn KA, Rajendran JG. A Robust Automated Measure of Average Antibody Staining in Immunohistochemistry Images. *J Histochem Cytochem.* 2010 Feb;58(2):95–107.
20. Rizzardì AE, Johnson AT, Vogel RI, Pambuccian SE, Henriksen J, Skubitz AP, et al. Quantitative comparison of immunohistochemical staining measured by digital image analysis versus pathologist visual scoring. *Diagn Pathol.* 2012 Jun 20;7:42.
21. Brey EM, Lalani Z, Johnston C, Wong M, McIntire LV, Duke PJ, et al. Automated Selection of DAB-labeled Tissue for Immunohistochemical Quantification. *J Histochem Cytochem.* 2003 May 1;51(5):575–84.
22. Schlederer M, Mueller KM, Haybaeck J, Heider S, Huttary N, Rosner M, et al. Reliable Quantification of Protein Expression and Cellular Localization in Histological Sections. *PLoS ONE.* 2014 Jul 11;9(7):e100822.

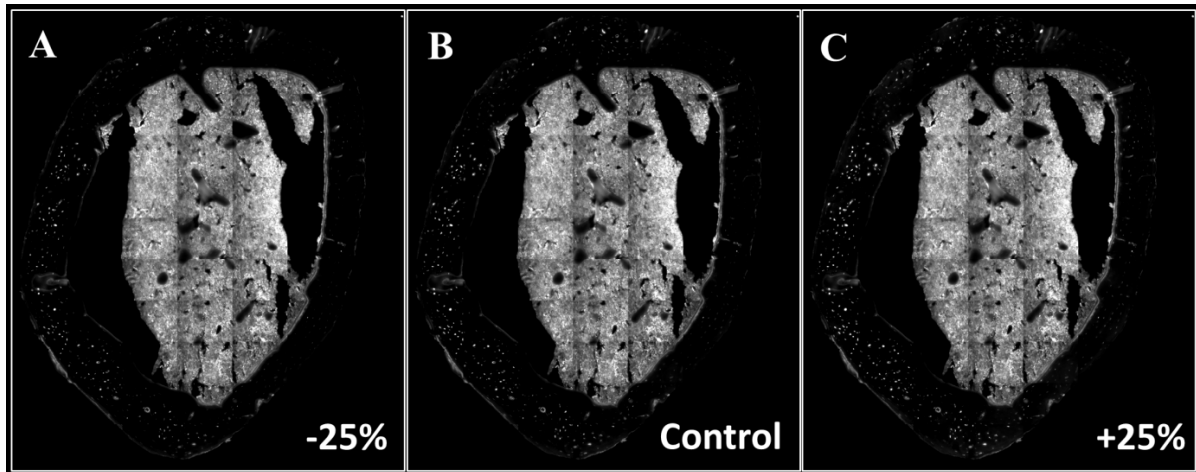
23. Mohammed ZMA, Orange C, McMillan DC, Mallon E, Doughty JC, Edwards J, et al. Comparison of visual and automated assessment of microvessel density and their impact on outcome in primary operable invasive ductal breast cancer. *Hum Pathol*. 2013 Aug;44(8):1688–95.
24. Kraan MC, Haringman JJ, Ahern MJ, Breedveld FC, Smith MD, Tak PP. Quantification of the cell infiltrate in synovial tissue by digital image analysis. *Rheumatol Oxf Engl*. 2000 Jan;39(1):43–9.
25. Ali HR, Irwin M, Morris L, Dawson S-J, Blows FM, Provenzano E, et al. Astronomical algorithms for automated analysis of tissue protein expression in breast cancer. *Br J Cancer*. 2013 Feb 19;108(3):602–12.
26. Gerdes MJ, Sevinsky CJ, Sood A, Adak S, Bello MO, Bordwell A, et al. Highly multiplexed single-cell analysis of formalin-fixed, paraffin-embedded cancer tissue. *Proc Natl Acad Sci*. 2013 Jul 16;110(29):11982–7.
27. Ecker RC, Steiner GE. Microscopy-based multicolor tissue cytometry at the single-cell level. *Cytometry A*. 2004 Jun 1;59A(2):182–90.
28. Lang DS, Heilenkötter U, Schumm W, Behrens O, Simon R, Vollmer E, et al. Optimized immunohistochemistry in combination with image analysis: A reliable alternative to quantitative ELISA determination of uPA and PAI-1 for routine risk group discrimination in breast cancer. *The Breast*. 2013 Oct;22(5):736–43.
29. Staněk L, Rozkoš T, Laco J, Ryška A, Petruželka L, Důra M, et al. Comparison of immunohistochemistry, four in situ hybridization methods and quantitative polymerase chain reaction for the molecular diagnosis of HER2 status in gastric cancer: a study of 55 cases. *Mol Med Rep*. 2014 Nov;10(5):2669–74.

Supplementary materials

Images



Supplementary figure 1. Creation of masks to isolate three anatomical areas of mouse cortical bone. A – mask of cortical bone without vessels and cutting artifacts; B – mask of cortical bone with filled holes, prepared for distance map analysis; C – mask of cortical bone after thresholding, 1 – periosteal, 2 – mid-cortical, 3 – endosteal areas; D – isolated mask of periosteal bone; E – isolated mask of mid-cortical bone; E – isolated mask of endosteal bone.



Supplementary figure 2. Illustration of 25% alteration of fluorescence intensity based on Sclerostin immunolabeling on mouse cortical bone. A – intensity reduced by 25%; B – control image; C – intensity increased by 25%.

Detailed protocol of immunohistochemistry

Mouse bones

Fixation

Mice bones were fixed in 10% Neutral Buffered Formalin for 36 hours at 4°. Proper fixation is crucial for IHC as over or under fixation alters antigens preservation. The time of exposure to Formalin depends on presence of surrounding tissue and sample size. The volume of the fixative used was at least 10 times more than the tissue. After 36 hours samples were rinsed with isotonic solution of NaCl and transferred to the 40% EtOH for at least 12 hours at 4° and then to the 70% EtOH. To get rid of residual Formalin, after 24 hours 70% EtOH should be replaced with the fresh solution. Samples can be safely stored in 70% EtOH at 4°.

Paraffin embedding

Decalcification

Prior to embedding in Paraffin samples were decalcified. Firstly, we rehydrated samples with transferring them to 40% Ethanol for 12h at 4°, then rinsed with isotonic solution and put them in Immunocal decalcifier (Decal Chemical Corp,1440) for 12h at 4°. Time of exposure to Immunocal depends on samples thickness, but 24h at 4° was sufficient for mice femora covered by muscles. The quality of decalcification was verified with μ CT (Viva CT 40; Scanco Medical, Switzerland). Decalcified samples were rinsed with isotonic solution and processed for paraffin embedding.

Embedding

Decalcified samples were placed in embedding cassettes (Simport, M491-6), labeled with solvent-proof tube checker pen and gradually dehydrated with Ethanol (40%, 70%, 90%, 100%) – from 9 to 12h in each solution at 4°, and Butanol, two changes – from 9 to 12h in each solution at 4°. Then samples were transferred to three sequential baths of liquid paraffin (Diawax 56, Diapath, 030980), 3 changes – from 9 to 12h in each at 60° under vacuum (Vacutherm, ThermoScientific) for proper paraffin penetration, and embedded with paraffin embedding station (Leica, EG1150H). Embedded samples were stored at 4°.

Notes: as Butanol is highly toxic it is recommended to perform all necessary manipulation with samples prior to immersing them to Butanol; over incubation in paraffin may result in tissue hardening and brittleness; avoid temperatures over 65° as it may result in antigen epitopes destruction.

Samples cutting and storage

For our purposes we used 5µm-thick sections obtained with microtome (Leica RM2245). We trimmed paraffin blocks to an optimal surface and placed them in the ice-cold demineralized H₂O to cool down. We used blades (Accu-Edge, 4690) and a cutting angle of 3°. Obtained slices were placed in 48° water bath (Leica, HI1210) in order to remove possible wrinkles. Then swimming sections were fished out with charged glass slides (Starfrost, Advanced Adhesive) and dried out on the warming plate at 37° (Leica, HI1220). After complete drying, sections were stored at 4°.

Notes: proper temperature and moisturizing of paraffin blocks are crucial for good tissue preservation, blocks should be cooled down by putting them in an ice-cold water hours before cutting; if quality of sections is getting low, put the block back to ice-cold water for few minutes; make sure that blades are sharp and clean, replace them often to avoid sections' vertical cuts or scratching; incomplete drying might results in sections damage.

Human biopsies

Preparation of Gelatin-coated Slides for Histological Tissue Sections

In order to get satisfactory adherence of MMA sections to glass slides (Superfrost, Thermo Scientific) covered with gelatin. We prepared the gelatin-coating solution by dissolving 4.5 g of gelatin (Sigma, G2500) in 500 mL of demineralized H₂O preheated to 60°. After the gelatin has dissolved, the solution was cooled down to 50° and 0.25 g of chromium potassium sulfate

(Sigma, 243361) was added. Then, solution was cooled down to 35°, and glass slides were immersed into the solution for 1 minute. Then, slides were air dried, immersed for 1 minute in the solution, and incubated at 37° overnight. Dried slides can be stored at room T°.

Samples cutting and storage

MMA blocks were stored at -20°. Prior to cut they were warmed up to ambient T°. For our purposes we used 5µm-thick sections obtained with microtome (Leica SM2500E). We polished MMA blocks to an optimal surface with a polishing station (ESCIL, ESC200GTL, France). In order to obtain sections of non-decalcified tissue with good histological quality we cut at low speed (not faster than 1.5 mm/sec). We used a tungsten carbide-tungsten blade (Microm, F152120, France) and a cutting angle of 0°. Cutting surface was kept wet with 30% Ethanol. Prior to cut a section we put a piece of filtering paper moistened in 30% Ethanol on the cutting surface. Thus, the obtained section stuck to the paper and did not roll or shrink. Next, sections were put in the bath with 30% Ethanol preheated to 40° and then fished out with gelatinized glass slides. Sections were kept wet all the time. To get good adherence of MMA sections to gelatinized slides we put slides on each other (we put non sticky plastic stripes in between slides to make later separation possible), flattened by a tapestry roller and compressed them with a clamp, applying pressure evenly if possible. Sections were kept wet while being compressed. Compressed slides were incubated at 56° for two hours and then at 42° overnight. Afterwards, slides were cooled down to room T° and carefully separated from each other. Obtained samples were stored at 4°.

Notes: caution is required with compression step – too high pressure results in broken slides, too low pressure leads to poor adherence and therefore to risk of uneven staining or samples loss.

General protocol of fluorescent IHC

Deparaffinisation or deplastification

Paraffin sections were pre-warmed at 37° for 30 min, and deparaffinized by incubation in two consecutive baths of Xylene for 5 min each at room temperature. MMA embedded sections were placed at 4° in three consecutive baths of 2-methoxyethylacetate (Sigma, 109886), for 24 hours each.

Rehydration

After removal of paraffin/plastic sections were gradually rehydrated by incubation in baths of 100% Ethanol (two changes), 90%, 70%, and 40% - 5 min in each. Next, sections were washed for 5 min at room T° in a bath of TBS (for 1l of TBS: 100ml of 0.5M Tris, pH = 7.6 (Sigma, 252859), 100ml of 9% NaCl and 800ml of demineralized H₂O) on a shaker (IKA, MTS2); TBS was refreshed after 5min.

Tissue isolation

Resting liquid was carefully wiped out and a circle of hydrophobic pen (Abcam, ab2601) was placed around tissue samples (5-10mm from the tissue's edge).

Decalcification (only for MMA embedded not decalcified samples)

We applied few drops of Immunocal (enough to cover the surface of the sample) for 3 min at room T°. Then, Immunocal was shaken off and the slides were washed in a bath of TBS for 5min at room T° on a shaker.

Cell's permeabilization

Sections were placed in a bath of TTBS (for 1l of TTBS: 1l of TBS and 1ml of Tween-20 (Sigma, p7949)) for 5 min at room T° on a shaker.

Notes: after TTBS step the tissue must never be dry.

Antigen retrieval

Samples were incubated with 5mg/ml solution of Proteinase K (Invitrogen, 100005393) (For 10ml: 6.4ml of demineralized H₂O, 800µl 0.5M Tris pH = 8, 800µl of 0.5M EDTA pH = 8, and 2µl of Proteinase K) for 10 min at 37° in the humid chamber. Then, samples were washed in a bath of TBS for 5 min at room T° on a shaker.

Notes: longer time incubation may lead to tissue damage and high background staining.

Aspecific binding blocking

Samples were incubated with 1% solution of bovine serum albumin (BSA) (Sigma, A4503) in TTBS for 100 min at 4° in the humid chamber. Next, samples were incubates with Protein Block (Abcam, ab64226) for 20 min at room T° in the humid chamber.

Notes: no washing steps between and after blocking solutions.

Primary antibody

Samples were incubated overnight at 4° in the humid chamber with primary antibody solutions (Tab 1). Solution of 1% BSA in TTBS was used as antibody diluent. After incubation samples were washed in TTBS, 2 changes – 5 min at room T° on a shaker.

Table 1. Primary antibodies

Target protein	Species	Primary antibody	Working dilution
Sclerostin	Mouse	Polyclonal, goat, R&D Systems, AF1589	1:300
DMP1	Mouse	Polyclonal, rabbit, Takara, M176	1:500
Periostin	Mouse	Polyclonal, goat, R&D Systems, AF2955	1:400
Sclerostin	Human	Polyclonal, rabbit, Abcam, ab63097	1:200
DMP1	Human	Monoclonal, mouse, Santa Cruz, LFMb-31	1:100

Secondary antibody

Samples were incubated for 45 min at 37° in the humid chamber with secondary antibody solutions (Tab.2). Solution of 1% BSA in TTBS was used as antibody diluent. After incubation samples were washed in TTBS – 5 min at room T° on a shaker.

Table 2. Secondary antibodies

Immunogen	Secondary antibody	Working dilution
Goat	Polyclonal rabbit anti-goat, biotinulated, Dako, E0466	1:600
Rabbit	Polyclonal goat anti-rabbit, biotinulated, Dako, E0432	1:600

Signal amplification

Samples were incubated either with 1:500 Streptavidin-Alexa Fluor (Life technologies, S 11225) solution in TTBS in the humid chamber for 30 min at 37°. After incubations samples were washed in TBS – 5 min at room T° on a shaker.

DAPI staining

Samples were incubated with the DAPI (Santa Cruz, 28718-90-3) solution (1:100 in TBS) for 30 min at 37° in the humid chamber. Then, samples were washed with demineralized water – 5 min at room T° on a shaker.

Mounting

IHC-F requires aqueous mounting medium with fluorescence protective properties. Samples were washed with demineralized H₂O – 5 min at room T° on a shaker, and then mounted with MaxGlow (Maxvision, MG-M).

IHC with the use of specific detection kits

For IHC staining of DMP1 on paraffin-embedded mouse bones and for Sclerostin on MMA embedded human biopsies we used specific PowerFluor detection kits specific for rabbit primary antibodies (MaxFluor 488, Maxvision, PF 21M) and mouse primary antibodies (MaxFluor 594, Maxvision, PF 13S). All steps prior to incubation with secondary antibody were done according to the general protocol. After incubation with primary antibody the subsequent procedures were done according to manufactures protocol. Then, samples were stained with DAPI and mounted as it described above.

Protein expression quantification: ImageJ operations

Protein expression quantification on a mouse cortical bone

Select an IHC labeling image:

Polygon selection, select desired region as one ROI, avoid vessels and cutting/staining artifacts

Edit – Clear outside

Select a DAPI image:

Image – Adjust – Threshold (black and white, dark background), threshold DAPI signal, click apply

Process – Binary – Make binary

Edit – Selection – Restore selection

Process – Binary – Dilate, Process – Binary – Dilate (should be visible expansion of particles)

Edit – Clear outside

Analyze – Set scale – Remove scale, Global

Analyze – Analyze particles, Parameters: Size in pixels 0-4000, Circularity 0-1, Show: nothing, Display results, Clear results, Add to manager.

Select an IHC labeling image:

Select all ROIs from the ROI manager, click on Measure

Results save as Excel table

Osteocyte density analysis

Analyze – Set scale, put appropriate scaling in μm

Select binary DAPI image

Analyze – Analyze particles, Size in μm 0-100, Circularity 0-1, Show: nothing, Summarize; results save as Excel table. Density = Total area in $\mu\text{m}^2/\text{Count}$.

Protein expression quantification on a three different regions of a mouse cortical bone

Select an IHC labeling image:

Polygon selection, select desired region as one ROI, avoid vessels and cutting/staining artifacts

Edit – Clear outside

Select a DAPI image:

Image – Adjust – Threshold (black and white, dark background), threshold DAPI signal, click apply

Process – Binary – Make binary

Edit – Selection – Restore selection

Process – Binary – Dilate, Process – Binary – Dilate (should be visible expansion of particles)

Edit – Clear outside

Analyze – Set scale – Remove scale, Global

Select an IHC labeling image:

Edit – Selection – Restore selection

Edit – Selection – Create mask, save as a Total Cortical Bone mask

Fill empty spaces with a Flood Fill tool and connect separated parts of the mask with a Paintbrush tool, save as a Corrected Total Cortical Bone mask

Select Total Cortical Bone mask:

Process – Binary – Distance map

Image – Adjust – Threshold (black and white, dark background) and set it to 1 and to a position according to the desired endosteal and periosteal regions thickness, click apply (we used 1 and 200). Save as a Periosteal and Endosteal Bone mask.

Select Total Cortical Bone mask:

Process – Image calculator, Image 1: Total Cortical Bone mask, subtract, Image 2: Periosteal and Endosteal Bone mask, save as a Mid-cortical Bone mask

Select Total Cortical Bone mask:

Process – Image calculator, Image 1: Total Cortical Bone mask, subtract, Image 2: Mid-cortical Bone mask, save as a Periosteal and Endosteal Bone mask corrected.

Select Periosteal and Endosteal Bone mask corrected:

Flood Fill tool (white) apply on Endosteal bone area, result save as a Periosteal Bone mask

Select Periosteal and Endosteal Bone mask corrected:

Flood Fill tool (white) apply on Periosteal bone area, result save as a Endosteal Bone mask

At the end there are three working masks: Periosteal Bone mask, Mid-cortical Bone mask, and Endosteal Bone mask.

Area selection for analysis:

Select desired mask and Edit – Selection – Create selection

Select binary DAPI image, Edit – Selection – Restore selection

Analyze – Set scale – Remove scale, Global

Analyze – Analyze particles, Parameters: Size in pixels 0-4000, Circularity 0-1, Show: nothing, Display results, Clear results, Add to manager

Select an IHC labeling image:

Select all ROIs from the ROI manager, click on Measure

Results save as Excel table

Repeat for other bone areas

Analysis of osteocyte proteins expression within osteocyte regions of influence

Select an IHC labeling image:

Polygon selection, select desired region as one ROI, avoid vessels and cutting/staining artifacts

Edit – Clear outside

Select a DAPI image:

Image – Adjust – Threshold (black and white, dark background), threshold DAPI signal, click apply

Process – Binary – Make binary

Edit – Selection – Restore selection

Process – Binary – Dilate, Process – Binary – Dilate (should be visible expansion of particles)

Edit – Clear outside

Analyze – Set scale – Remove scale, Global

Analyze – Analyze particles, Parameters: Size in pixels 0-4000, Circularity 0-1, Show: masks. Save mask as a DAPI Total Cortical Bone mask.

Select a DAPI Total Cortical Bone mask:

Process – Binary – Voronoi

Image – Adjust – Threshold (black and white, dark background), threshold to 0 and 0, save as Voronoi mask

Select appropriate selection either from total cortical bone or from one of the anatomical regions (see **Protein expression quantification on a three different regions of a mouse cortical bone**)

Select Voronoi mask:

Edit – Selection – Restore selection

Analyze – Analyze particles, Parameters: Size in pixels 0, Circularity 0-1, Show: nothing, Display results, Clear results, Add to manager

Select an IHC labeling image:

Select all ROIs from the ROI manager, click on Measure

Results save as Excel table

Analysis of osteocyte proteins expression for human biopsies

Open IHC labeling image and its corresponding brightfield and DAPI channels

Overlay IHC labeling, DAPI and Brightfield images for detection of osteocytes:

Image – Color – Merge channels

Use paint brush 50 pixels black for manual pointing on osteocytes:

Paintbrush tool – options

Select desired region as one ROI, avoid vessels and cutting/staining artifacts:

Polygon selection, then Edit – Clear outside

Analyze – Set scale – Remove scale, Global

For Sclerostin analysis:

Select image with pointed osteocytes

Image – Adjust – Threshold (black and white, dark background), threshold to 0 and 0

Process – Binary – Voronoi

Image – Adjust – Threshold (black and white, dark background), threshold to 0 and 0, save as Voronoi mask

Select Voronoi mask image:

Edit – Selection – Restore selection

Analyze – Analyze particles, Parameters: Size in pixels 0, Circularity 0-1, Show: nothing,

Display results, Clear results, Add to manager

Select IHC image:

Select all ROIs from the ROI manager, click on Measure

Results save as Excel table

For DMP1 analysis:

Select image with pointed osteocytes

Image – Adjust – Threshold (black and white, dark background), threshold to 0 and 0

Process – Binary – make binary

Process – Binary – Options – Iterations 80

Edit – Selection – Restore selection

Process – Binary – Dilate

Process – Binary – Watershed

Analyze – Analyze particles, Parameters: Size in pixels 0-4000, Circularity 0-1, Show: nothing, Display results, Clear results, Add to manager

Select IHC image:

Select all ROIs from the ROI manager, click on Measure

Results save as Excel table

Autofluorescence: a useful feature for lacunae-canalicular morphology assessment?

While working with fluorescence IHC we have always noticed a non-specific autofluorescence of bone marrow cells, vessels, erythrocytes, osteocytes, canaliculi, and collagen. When IHC labeling is proper there is not difficulty to distinguish much brighter specific signal from autofluorescence and generally, reduction of UV lamp power or exposure time allows us to get rid of it. However, for non-experienced used a risk of IHC results misinterpretation/miscalculation might be high.

When we were using a powerful laser of a confocal microscope, we observed that autofluorescence might have a useful quality: a tool for assessment of lacunar-canalicular network morphology. We found irradiation with a laser at a wavelength of 273nm led to bright non-specific emission with highest intensity in green spectrum (Fig. 23 – 26). Importantly, such detailed images were obtained without any particular treatment of bone sections: only deparaffinization in Xylene, rehydration and mounting in Vectashield (Vector lab., H-1000).

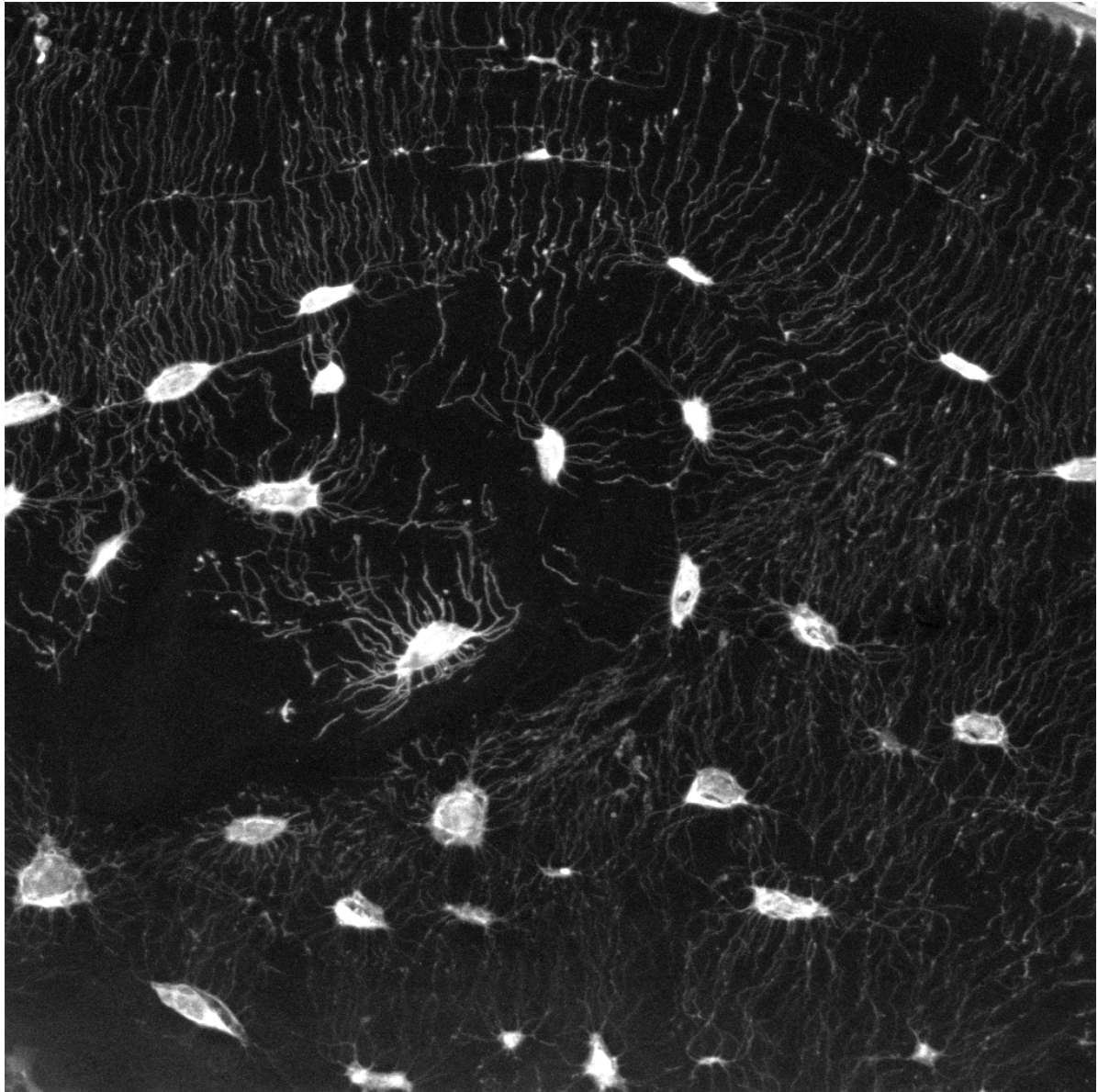


Figure 23. Confocal imaging of autofluorescence of lacunar-canalicular network from a paraffin embedded mouse femoral cortex, x960, 5 μ m thickness, laser 421nm.

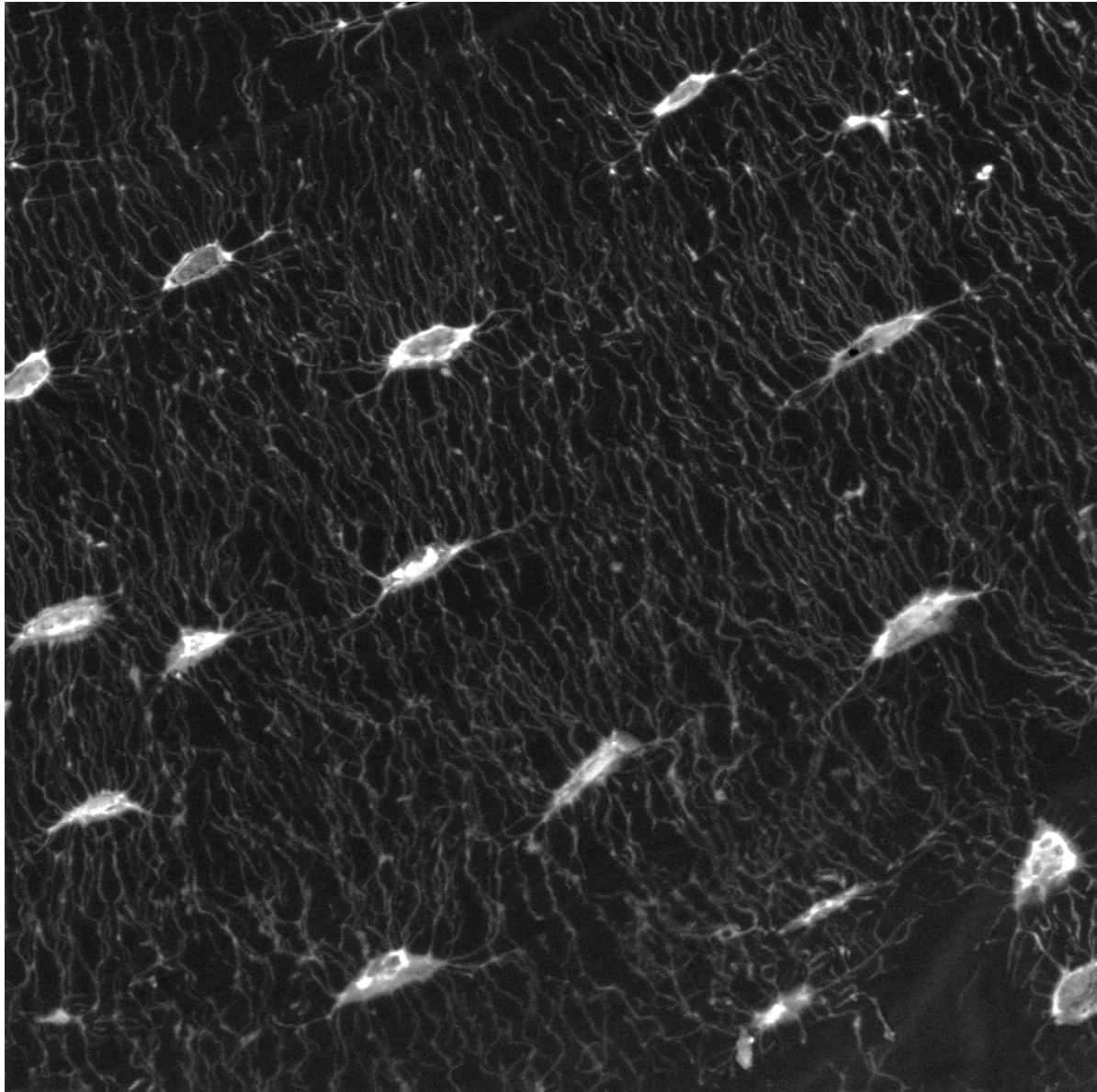


Figure 24. Confocal imaging of autofluorescence of lacunar-canalicular network from a paraffin embedded mouse femoral cortex, x960, 5 μ m thickness, laser 421nm.

The concern we had was whether 100% of canalicular-lacunar network has such high autofluorescence. To answer this question, two consecutive bone sections have to be compared: non-treated and immersed in fluorescent dye solution. However, we believe that even in the present status, our findings allow us to detect pathology- or age-related alterations of lacunar-canalicular network in a very easy manner.

Closer view revealed complex network, which ensure close contact of osteocytes and blood vessels (Fig. 25 and 26) and further emphasize systemic role of osteocytes.

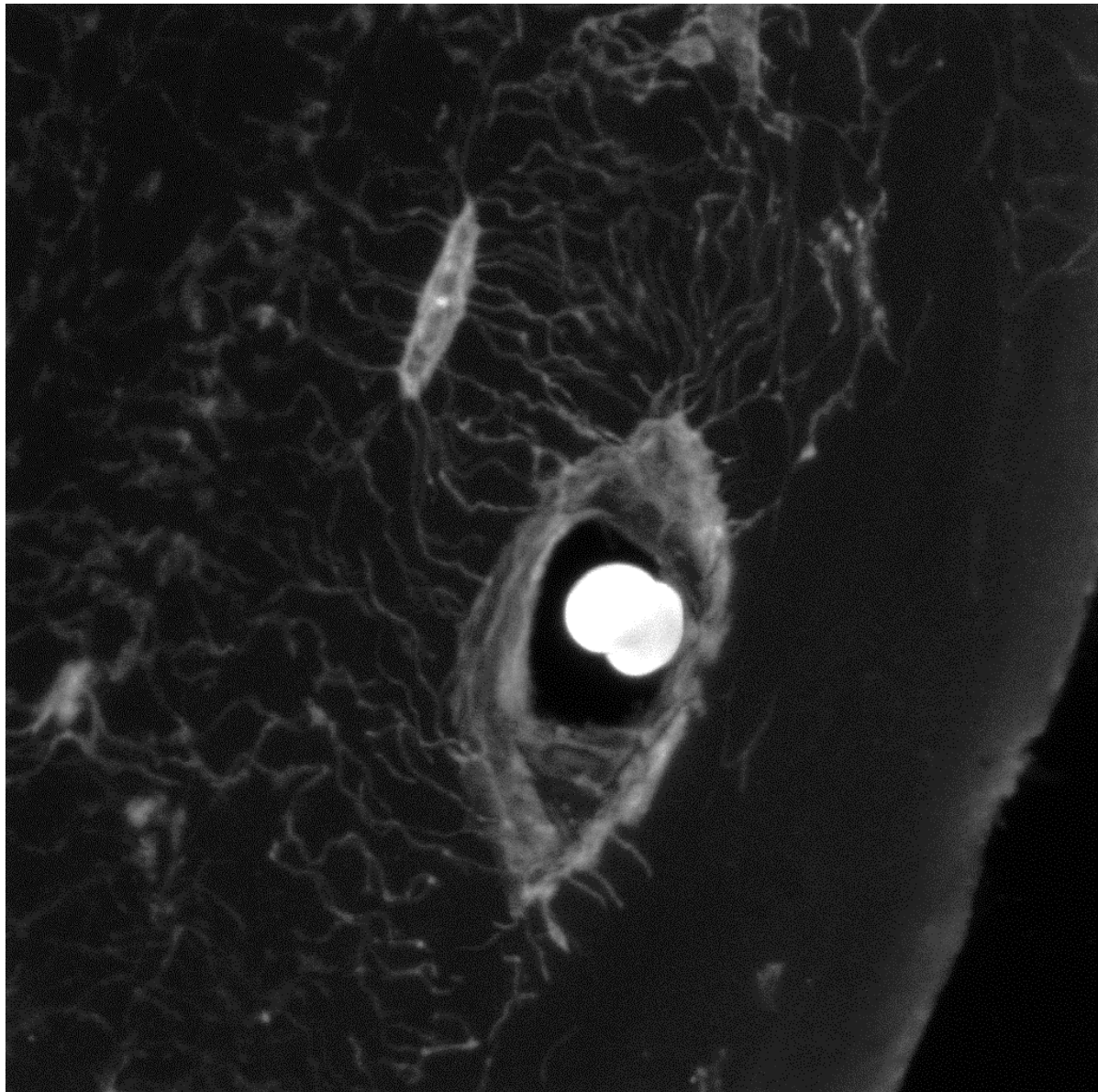


Figure 25. Confocal imaging of autofluorescence of lacunar-canalicular network and a vessel with two erythrocytes inside (brightest objects) from a paraffin embedded mouse femoral cortex, x2400, 5 μ m thickness, excitation laser 273nm, and emission 488nm.

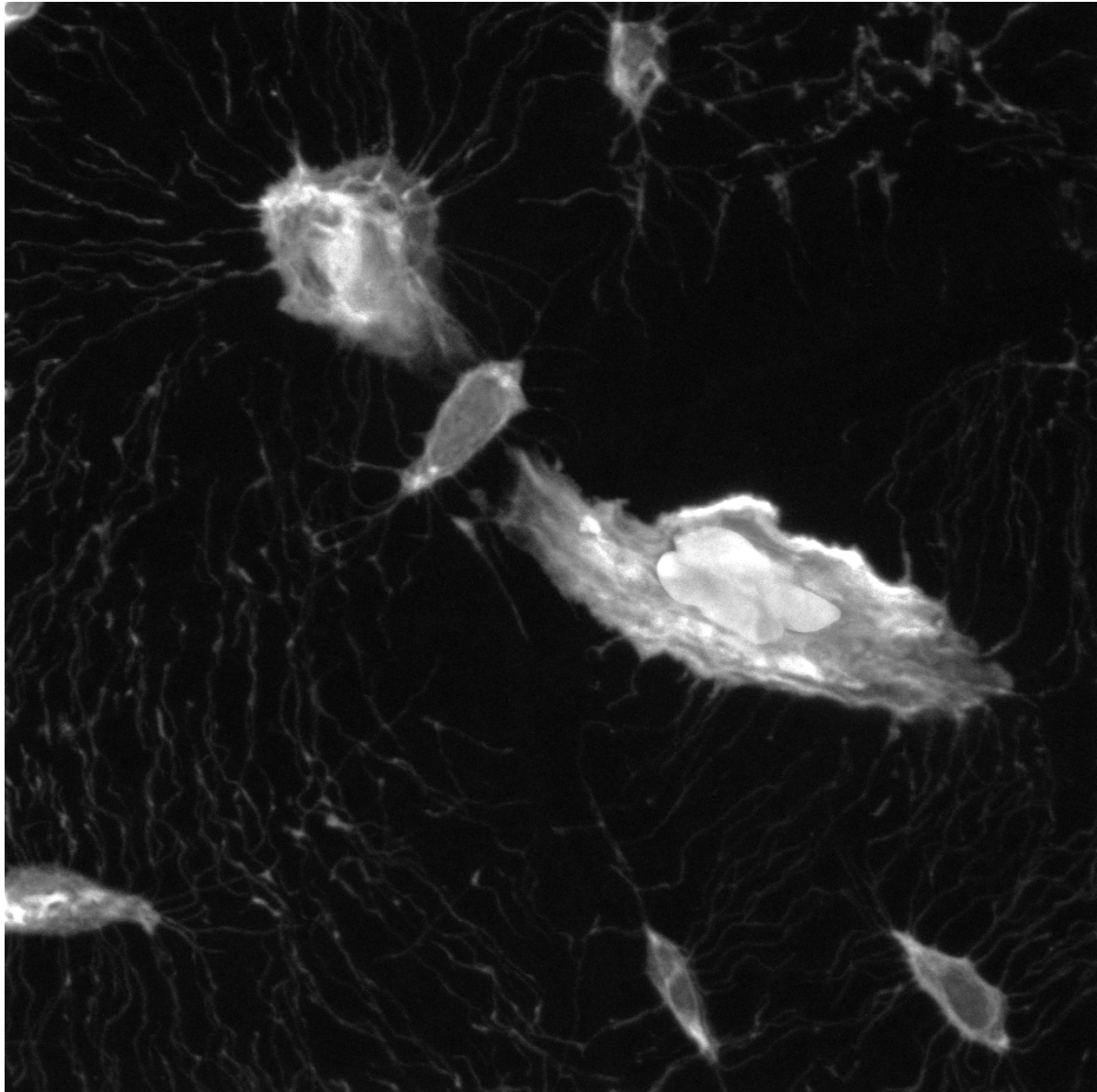


Figure 26. Confocal imaging of autofluorescence of lacunar-canalicular network and two vessels from a paraffin embedded mouse femoral cortex; a bigger vessels contains erythrocytes inside; x1800, 5 μ m thickness, excitation laser 273nm, and emission 488nm.

Impressively, such rich of data pictures were obtained from only 5 μ m-thick sections, and we were surprised that we have never revealed canalicular system so well with IHC staining, even with largely distributed proteins as DMP1. The possible explanation is discussed in the following chapter.

3D assessment of osteocyte proteins

Traditional 2D IHC has significant limitations in relation to assessment of lacunae canalicular network morphology due to its spatial complexity, and assessment of proteins distribution in this network. However, from our point of view the biggest problem here is a limited

infiltration of bone tissue by antibodies during IHC procedures. Thus, when we combined DMP1 IHC labeling with non-specific autofluorescence we observed that most of the lacunar-canalicular network remained unstained (Fig. 27). Only osteocyte lacunae were well labeled as they were probably open during a cutting by microtome. In contrast, canalicular network remains difficult to penetrate using traditional IHC approach. This issue might be partly solved by increasing incubation times with antibodies; however it increases a risk of non-specific labeling and background staining.

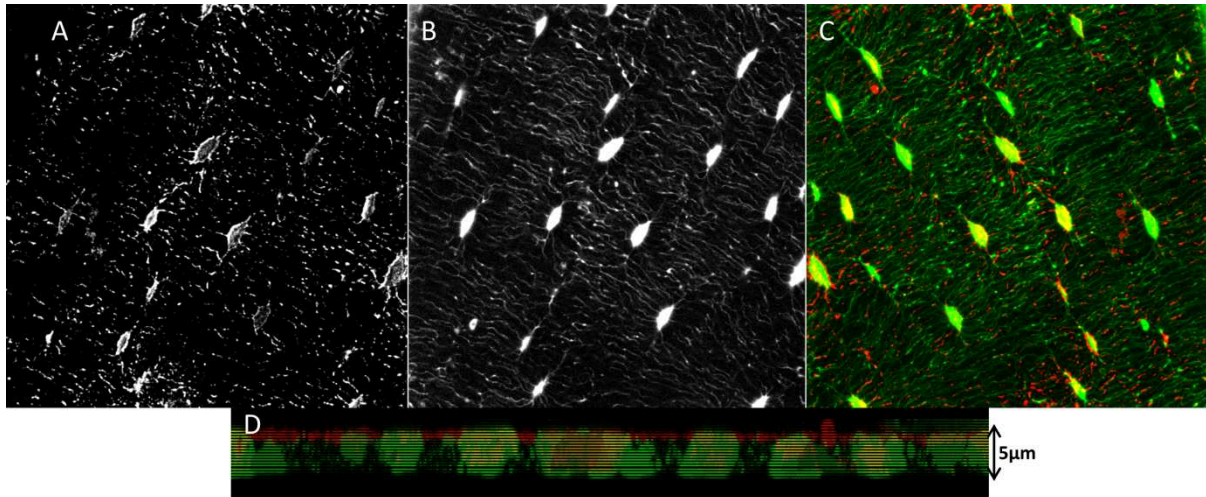


Figure 27. Confocal imaging of DMP1 labeling (A, in white color) and autofluorescence (B, in white color) of lacunar-canalicular network from the same region of mouse femoral cortex. On a merged image (C) DMP1 is in red and non-specific fluorescence is in green. On a Z (vertical) image (D) it is obvious that DMP1 (in red) penetrated solely an upper layer of canalicular network and went through some lacunae (in red/yellow) on 5µm-thick section. It could explain disrupted pattern of canalicular staining on the image A.

Inspired by methods of highly specific 3D IHC that are used in neuroscience [87], we developed a new technique of 3D IHC on mice cortical bones. It allowed us to visualize a distribution of Sclerostin among osteocytes and blood vessels (Fig. 28, Supplementary video 1). One of the major advantages of this technique is that there is no need for expensive and sophisticated hardware and software; any step of 3D IHC protocol can be done in almost every laboratory. Without the help of confocal microscopy and powerful computers we managed to obtain 3D pictures 45 µm section of cortical bone from z-stack of about 100 images with x630 magnification (Supplementary video 2) on AxioObserver Z1 microscope (Zeiss, Darmstad, Germany). Five micrometers is the most commonly used thickness level for IHC on paraffin embedded samples. Visualization of even 5 µm depth z-stack of images provides much more information about protein distribution than classical IHC. So far we have designed a reproducible protocol for Sclerostin detection in 3D (Supplementary

materials). We clearly visualized that Sclerostin positive canaliculi are connected to blood vessels in the mouse cortical bone. It was possible to track in 3D particular canaliculi from osteocytes to vessels. We believe, that such technique would allow us to better understand a role of osteocytes in bone physiology and give us insights on bone remodeling regulations.

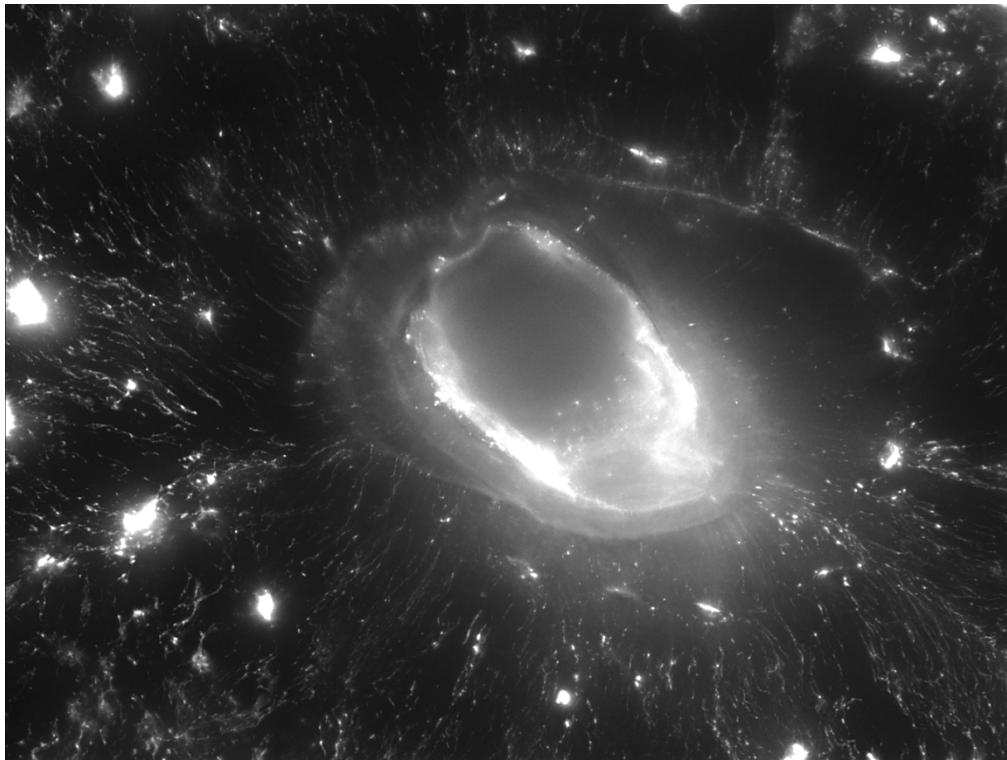


Figure 28. Fluorescent immunohistochemistry of Sclerostin on 10µm thick section of mouse femoral cortex. Lacunar-canalicular network and blood vessel. Oil immersed objective, x1000. Osteocytes are saturated in order to see better the canalicular network. Bright points on vessel wall are places of canaliculae insertions, we assumed that Sclerostin can accumulate there.

To summarize, our findings allow researchers to perform reliable single or double IHC labeling of osteocyte proteins on paraffin or MMA embedded murine or human bone samples. We developed a sensitive and reproducible protocol of IHC data semi-automatic quantification, adapted for proteins with lacunae, matrix or canalicular localization.

Also, we have demonstrated existing limitations of IHC for detection of canalicular network features and we offered a solution (3D IHC), which allowed us to dramatically increase amount of obtained data. Further steps would be to adapt 3D IHC protocols for other osteocyte proteins and to visualize bigger bone samples to obtain 3D map of proteins co-localizations.

Conclusion and perspectives

The main focus of the research project was to further study fundamental mechanisms underlying bone adaptation to gravity-induced mechanical loading and to assess effects of two different hypergravity models on skeleton of young healthy mice. Same duration of the experiments and the use of animals of the same type and age allowed us to make comparisons between different skeleton adaptations to continuous hypergravity generated by centrifugation and to intermittent one generated by WBV.

We observed that centrifugation reduced resorption and increased formation in trabecular bone, whereas WBV did not uncoupled resorption and formation activities and stimulated both of them simultaneously. Centrifugation resulted in reorganized trabecular microarchitecture in femur and vertebra but had no effect on cortical bone mass-structural parameters. In contrast, WBV stimulated cortical bone geometrical expansion in 3-week experiment and increased cortical mineral density in 9 weeks. Both hypergravity models resulted in lower Sclerostin and higher DMP1 expressions in femoral cortex. Also, both models resulted in higher number of blood vessels in femoral metaphysis, however only centrifugation increased vessels volume.

These findings let us assume that a combination of two hypergravity models might be beneficial for both bone compartments and the next challenge is to design a study combining these mechanical stimulations. Also, it is important to test same experimental conditions in older animals to differentiate effects of skeletal growth and adaptation, and to verify bone protective abilities of centrifugation or WBV with osteopenic models.

Concerning practical implication of centrifugation as countermeasures for human spaceflights, there is much remaining to be studied. First promising results of “gravitational therapy” application for human bones were reported by Kotelnikov et al. [88]. Authors demonstrated that 15 min exposure to 1.5-3g was beneficial for bone fractures healing. We believe that findings from such studies can be used for the future research projects aimed to determine an optimal g level, frequency, and time of exposure to hypergravity. Another aspect, which might be important for development of countermeasures against spaceflight related bone loss, is effects of hypergravity on recovery processes after exposure to microgravity.

In relation to technical objects of the research project, we successfully developed a method of quantitative IHC, which allowed us to detect and verify statistically even modest alterations of osteocyte protein expressions in our experiments. We believe that IHC results should always be quantitatively analyzed and we provide a tool for both mice and human bone samples embedded in paraffin or MMA.

Our experience showed that reproducibility of IHC labeling and subsequent quantification are very demanding to initial histological quality of bone samples and to strict following of the staining procedures, therefore we provided detailed protocols for tissue processing and labeling.

Traditional IHC on bone sections has significant limitations due to limited antibodies penetration. As it has been demonstrated, recommended procedures results in 2-3 μ m penetration of canaliculae and only cellular bodies becomes fully labeled. Presumably, it is only relevant for a dense cortical bone and for small in diameter canaliculae. We obtained promising results using the Clarity technique [87], initially developed for IHC on thick brain slices (≥ 1 mm thickness) but optimized for our needs. Definitely, this IHC protocol reveals much more details compare to classical IHC on paraffin sections and our protocol can be even further improved as recently many articles have been published providing improvements to the original Clarity protocol [89,90] or offering new ones [91]. We believe that our IHC quantification technique might be adapted to measurements of protein expression in 3D on thick bone sections however it would require more powerful imaging stations.

References

- [1] Martin TJ. Bone biology and anabolic therapies for bone: current status and future prospects. *J Bone Metab* 2014;21:8–20. doi:10.11005/jbm.2014.21.1.8.
- [2] Sims NA, Gooi JH. Bone remodeling: Multiple cellular interactions required for coupling of bone formation and resorption. *Semin Cell Dev Biol* 2008;19:444–51. doi:10.1016/j.semcdb.2008.07.016.
- [3] Martin T, Gooi JH, Sims NA. Molecular mechanisms in coupling of bone formation to resorption. *Crit Rev Eukaryot Gene Expr* 2009;19:73–88.
- [4] Horwood NJ. Immune cells and bone: coupling goes both ways. *Immunol Invest* 2013;42:532–43. doi:10.3109/08820139.2013.822762.
- [5] Bonewald LF. The amazing osteocyte. *J Bone Miner Res* 2011;26:229–38. doi:10.1002/jbmr.320.
- [6] Lerner UH. Osteoblasts, Osteoclasts, and Osteocytes: Unveiling Their Intimate-Associated Responses to Applied Orthodontic Forces. *Semin Orthod* 2012;18:237–48. doi:10.1053/j.sodo.2012.06.002.
- [7] Samee N, Geoffroy V, Marty C, Schiltz C, Vieux-Rochas M, Levi G, et al. *Dlx5*, a Positive Regulator of Osteoblastogenesis, is Essential for Osteoblast-Osteoclast Coupling. *Am J Pathol* 2008;173:773–80. doi:10.2353/ajpath.2008.080243.
- [8] Nakashima T, Hayashi M, Fukunaga T, Kurata K, Oh-hora M, Feng JQ, et al. Evidence for osteocyte regulation of bone homeostasis through RANKL expression. *Nat Med* 2011;17:1231–4. doi:10.1038/nm.2452.
- [9] Crockett JC, Rogers MJ, Coxon FP, Hocking LJ, Helfrich MH. Bone remodelling at a glance. *J Cell Sci* 2011;124:991–8. doi:10.1242/jcs.063032.
- [10] Andersen TL, Hauge EM, Rolighed L, Bollerslev J, Kjærsgaard-Andersen P, Delaisse J-M. Correlation between Absence of Bone Remodeling Compartment Canopies, Reversal Phase Arrest, and Deficient Bone Formation in Post-Menopausal Osteoporosis. *Am J Pathol* 2014;184:1142–51. doi:10.1016/j.ajpath.2013.12.005.
- [11] Sims NA, Martin TJ. Coupling signals between the osteoclast and osteoblast: how are messages transmitted between these temporary visitors to the bone surface? *Bone Res* 2015;6:41. doi:10.3389/fendo.2015.00041.
- [12] Eriksen EF, Melsen F, Mosekilde L. Reconstruction of the resorptive site in iliac trabecular bone: a kinetic model for bone resorption in 20 normal individuals. *Metab Bone Dis* 1984;5:235–42.

- [13] Vignery A, Baron R. Dynamic histomorphometry of alveolar bone remodeling in the adult rat. *Anat Rec* 1980;196:191–200. doi:10.1002/ar.1091960210.
- [14] Delaisse J-M. The reversal phase of the bone-remodeling cycle: cellular prerequisites for coupling resorption and formation. *BoneKEy Rep* 2014;3:561. doi:10.1038/bonekey.2014.56.
- [15] Tran Van P, Vignery A, Baron R. An electron-microscopic study of the bone-remodeling sequence in the rat. *Cell Tissue Res* 1982;225:283–92.
- [16] Buenzli PR, Sims NA. Quantifying the osteocyte network in the human skeleton. *Bone* 2015;75:144–50. doi:10.1016/j.bone.2015.02.016.
- [17] Franz-Odenaal TA, Hall BK, Witten PE. Buried alive: how osteoblasts become osteocytes. *Dev Dyn* 2006;235:176–90. doi:10.1002/dvdy.20603.
- [18] Dallas SL, Prideaux M, Bonewald LF. The Osteocyte: An Endocrine Cell ... and More. *Endocr Rev* 2013;34:658–90. doi:10.1210/er.2012-1026.
- [19] van Bezooijen RL, Roelen BAJ, Visser A, van der Wee-Pals L, Wilt E de, Karperien M, et al. Sclerostin Is an Osteocyte-expressed Negative Regulator of Bone Formation, But Not a Classical BMP Antagonist. *J Exp Med* 2004;199:805–14. doi:10.1084/jem.20031454.
- [20] Brott BK, Sokol SY. Regulation of Wnt/LRP signaling by distinct domains of Dickkopf proteins. *Mol Cell Biol* 2002;22:6100–10.
- [21] Li X, Liu P, Liu W, Maye P, Zhang J, Zhang Y, et al. Dkk2 has a role in terminal osteoblast differentiation and mineralized matrix formation. *Nat Genet* 2005;37:945–52. doi:10.1038/ng1614.
- [22] Feng JQ, Ward LM, Liu S, Lu Y, Xie Y, Yuan B, et al. Loss of DMP1 causes rickets and osteomalacia and identifies a role for osteocytes in mineral metabolism. *Nat Genet* 2006;38:1310–5. doi:10.1038/ng1905.
- [23] Wijenayaka AR, Kogawa M, Lim HP, Bonewald LF, Findlay DM, Atkins GJ. Sclerostin Stimulates Osteocyte Support of Osteoclast Activity by a RANKL-Dependent Pathway. *PLoS ONE* 2011;6:e25900. doi:10.1371/journal.pone.0025900.
- [24] Xiong J, Onal M, Jilka RL, Weinstein RS, Manolagas SC, O'Brien CA. Matrix-embedded cells control osteoclast formation. *Nat Med* 2011;17:1235–41. doi:10.1038/nm.2448.
- [25] Burr DB, Robling AG, Turner CH. Effects of biomechanical stress on bones in animals. *Bone* 2002;30:781–6.
- [26] Tatsumi S, Ishii K, Amizuka N, Li M, Kobayashi T, Kohno K, et al. Targeted ablation of osteocytes induces osteoporosis with defective mechanotransduction. *Cell Metab* 2007;5:464–75. doi:10.1016/j.cmet.2007.05.001.

- [27] Jacobs CR, Temiyasathit S, Castillo AB. Osteocyte Mechanobiology and Pericellular Mechanics. *Annu Rev Biomed Eng* 2010;12:369–400. doi:10.1146/annurev-bioeng-070909-105302.
- [28] Burra S, Nicoletta DP, Francis WL, Freitas CJ, Mueschke NJ, Poole K, et al. Dendritic processes of osteocytes are mechanotransducers that induce the opening of hemichannels. *Proc Natl Acad Sci U S A* 2010;107:13648–53. doi:10.1073/pnas.1009382107.
- [29] Batra N, Burra S, Siller-Jackson AJ, Gu S, Xia X, Weber GF, et al. Mechanical stress-activated integrin $\alpha 5\beta 1$ induces opening of connexin 43 hemichannels. *Proc Natl Acad Sci U S A* 2012;109:3359–64. doi:10.1073/pnas.1115967109.
- [30] Bonewald LF, Johnson ML. Osteocytes, Mechanosensing and Wnt Signaling. *Bone* 2008;42:606–15. doi:10.1016/j.bone.2007.12.224.
- [31] Balemans W, Ebeling M, Patel N, Van Hul E, Olson P, Dioszegi M, et al. Increased bone density in sclerosteosis is due to the deficiency of a novel secreted protein (SOST). *Hum Mol Genet* 2001;10:537–43.
- [32] Brunkow ME, Gardner JC, Van Ness J, Paepfer BW, Kovacevich BR, Proll S, et al. Bone dysplasia sclerosteosis results from loss of the SOST gene product, a novel cysteine knot-containing protein. *Am J Hum Genet* 2001;68:577–89.
- [33] Baron R, Rawadi G. Targeting the Wnt/beta-catenin pathway to regulate bone formation in the adult skeleton. *Endocrinology* 2007;148:2635–43. doi:10.1210/en.2007-0270.
- [34] Sawakami K, Robling AG, Ai M, Pitner ND, Liu D, Warden SJ, et al. The Wnt co-receptor LRP5 is essential for skeletal mechanotransduction but not for the anabolic bone response to parathyroid hormone treatment. *J Biol Chem* 2006;281:23698–711. doi:10.1074/jbc.M601000200.
- [35] Robinson JA, Chatterjee-Kishore M, Yaworsky PJ, Cullen DM, Zhao W, Li C, et al. Wnt/beta-catenin signaling is a normal physiological response to mechanical loading in bone. *J Biol Chem* 2006;281:31720–8. doi:10.1074/jbc.M602308200.
- [36] Komiya Y, Habas R. Wnt signal transduction pathways. *Organogenesis* 2008;4:68–75.
- [37] Robling AG, Niziolek PJ, Baldrige LA, Condon KW, Allen MR, Alam I, et al. Mechanical stimulation of bone in vivo reduces osteocyte expression of Sost/sclerostin. *J Biol Chem* 2008;283:5866–75. doi:10.1074/jbc.M705092200.
- [38] Tu X, Rhee Y, Condon KW, Bivi N, Allen MR, Dwyer D, et al. Sost downregulation and local Wnt signaling are required for the osteogenic response to mechanical loading. *Bone* 2012;50:209–17. doi:10.1016/j.bone.2011.10.025.
- [39] Spatz JM, Fields EE, Yu EW, Divieti Pajevic P, Bouxsein ML, Sibonga JD, et al. Serum sclerostin increases in healthy adult men during bed rest. *J Clin Endocrinol Metab*

2012;97:E1736–40. doi:10.1210/jc.2012-1579.

- [40] Morse LR, Sudhakar S, Danilack V, Tun C, Lazzari A, Gagnon DR, et al. Association between sclerostin and bone density in chronic spinal cord injury. *J Bone Miner Res* 2012;27:352–9. doi:10.1002/jbmr.546.
- [41] Compton JT, Lee FY. A Review of Osteocyte Function and the Emerging Importance of Sclerostin. *J Bone Jt Surg* 2014;96:1659–68. doi:10.2106/JBJS.M.01096.
- [42] Toyosawa S, Shintani S, Fujiwara T, Ooshima T, Sato A, Ijuhin N, et al. Dentin matrix protein 1 is predominantly expressed in chicken and rat osteocytes but not in osteoblasts. *J Bone Miner Res* 2001;16:2017–26. doi:10.1359/jbmr.2001.16.11.2017.
- [43] Feng JQ, Huang H, Lu Y, Ye L, Xie Y, Tsutsui TW, et al. The Dentin matrix protein 1 (Dmp1) is specifically expressed in mineralized, but not soft, tissues during development. *J Dent Res* 2003;82:776–80.
- [44] Zhang R, Lu Y, Ye L, Yuan B, Yu S, Qin C, et al. Unique roles of phosphorus in endochondral bone formation and osteocyte maturation. *J Bone Miner Res* 2011;26:1047–56. doi:10.1002/jbmr.294.
- [45] Gluhak-Heinrich J, Ye L, Bonewald LF, Feng JQ, MacDougall M, Harris SE, et al. Mechanical Loading Stimulates Dentin Matrix Protein 1 (DMP1) Expression in Osteocytes In Vivo. *J Bone Miner Res* 2003;18:807–17. doi:10.1359/jbmr.2003.18.5.807.
- [46] Harris SE, Gluhak-Heinrich J, Harris MA, Yang W, Bonewald LF, Riha D, et al. DMP1 and MEPE expression are elevated in osteocytes after mechanical loading in vivo: theoretical role in controlling mineral quality in the perilacunar matrix. *J Musculoskelet Neuronal Interact* 2007;7:313–5.
- [47] White RJ, Averner M. Humans in space. *Nature* 2001;409:1115–8. doi:10.1038/35059243.
- [48] Williams D, Kuipers A, Mukai C, Thirsk R. Acclimation during space flight: effects on human physiology. *CMAJ* 2009;180:1317–23. doi:10.1503/cmaj.090628.
- [49] Adams GR, Caiozzo VJ, Baldwin KM. Skeletal muscle unweighting: spaceflight and ground-based models. *J Appl Physiol Bethesda Md* 1985 2003;95:2185–201. doi:10.1152/jappphysiol.00346.2003.
- [50] Sides MB, Vernikos J, Convertino VA, Stepanek J, Tripp LD, Draeger J, et al. The Bellagio Report: Cardiovascular risks of spaceflight: implications for the future of space travel. *Aviat Space Environ Med* 2005;76:877–95.
- [51] Yates BJ, Kerman IA. Post-spaceflight orthostatic intolerance: possible relationship to microgravity-induced plasticity in the vestibular system. *Brain Res* 1998;28:73–82.
- [52] Vico L, Collet P, Guignandon A, Lafage-Proust M-H, Thomas T, Rehalia M, et al. Effects of long-term microgravity exposure on cancellous and cortical weight-bearing bones of cosmonauts. *The Lancet* 2000;355:1607–11. doi:10.1016/S0140-

6736(00)02217-0.

- [53] Mack PB, Lacuance PA, Vose GP, Vogt FB. Bone demineralization of foot and hand of gemini-titan iv, v and vii astronaut during orbital flight. *Am J Roentgenol* 1967;100:503–11. doi:10.2214/ajr.100.3.503.
- [54] LeBlanc A, Shackelford L, Schneider V. Future human bone research in space. *Bone* 1998;22:113S – 116S.
- [55] LeBlanc A, Schneider V, Shackelford L, West S, Oganov V, Bakulin A, et al. Bone mineral and lean tissue loss after long duration space flight. *J Musculoskelet Neuronal Interact* 2000;1:157–60.
- [56] Lang T, LeBlanc A, Evans H, Lu Y, Genant H, Yu A. Cortical and trabecular bone mineral loss from the spine and hip in long-duration spaceflight. *J Bone Miner* 2004;19:1006–12. doi:10.1359/JBMR.040307.
- [57] Sibonga JD, Evans HJ, Sung HG, Spector ER, Lang TF, Oganov VS, et al. Recovery of spaceflight-induced bone loss: bone mineral density after long-duration missions as fitted with an exponential function. *Bone* 2007;41:973–8. doi:10.1016/j.bone.2007.08.022.
- [58] Davis BL, Cavanagh PR, Sommer HJ, Wu G. Ground reaction forces during locomotion in simulated microgravity. *Aviat Space Environ Med* 1996;67:235–42.
- [59] McCrory JL, Derr J, Cavanagh PR. Locomotion in simulated zero gravity: ground reaction forces. *Aviat Space Environ Med* 2004;75:203–10.
- [60] Smith SM, Zwart SR, Heer M, Lee SMC, Baecker N, Meuche S, et al. WISE-2005: Supine treadmill exercise within lower body negative pressure and flywheel resistive exercise as a countermeasure to bed rest-induced bone loss in women during 60-day simulated microgravity. *Bone* 2008;42:572–81. doi:10.1016/j.bone.2007.11.015.
- [61] Kohrt WM, Bloomfield SA, Little KD, Nelson ME, Yingling VR. Physical activity and bone health. *Med Sci Sports Exerc* 2004;36:1985–96. doi:10.1249/01.MSS.0000142662.21767.58.
- [62] Smith SM, Heer MA, Shackelford LC, Sibonga JD, Ploutz-Snyder L, Zwart SR. Benefits for bone from resistance exercise and nutrition in long-duration spaceflight: Evidence from biochemistry and densitometry. *J Bone Miner Res* 2012;27:1896–906. doi:10.1002/jbmr.1647.
- [63] Clément G, Pavy-Le Traon A. Centrifugation as a countermeasure during actual and simulated microgravity: a review. *Eur J Appl Physiol* 2004;92:235–48. doi:10.1007/s00421-004-1118-1.
- [64] Caiozzo VJ, Haddad F, Lee S, Baker M, Paloski W, Baldwin KM. Artificial gravity as a countermeasure to microgravity: a pilot study examining the effects on knee extensor and plantar flexor muscle groups. *J Appl Physiol* 2009;107:39–46.

doi:10.1152/jappphysiol.91130.2008.

- [65] Wade CE. Responses across the gravity continuum: hypergravity to microgravity. *Adv Space Biol Med* 2005;10:225–45.
- [66] Jaekel E, Amtmann E, Oyama J. Effect of chronic centrifugation on bone density of the rat. *Anat Embryol* 1977;151:223–32.
- [67] Smith SD. Effects of long-term rotation and hypergravity on developing rat femurs. *Aviat Space Environ Med* 1975;46:248–53.
- [68] Pace N, Smith AH, Rahlmann DF. Skeletal mass change as a function of gravitational loading. *The Physiologist* 1985;28:S17–20.
- [69] Wunder CC, Cook KM, Watkins SR, Moressi WJ. Femur-bending properties as influenced by gravity: V. Strength vs. calcium and gravity in rats exposed for 2 weeks. *Aviat Space Environ Med* 1987;58:977–82.
- [70] Fosse G, Gat H, Holmbakken N, Kvinnsland S. Bone atrophy and hypergravity in mice. *Growth* 1974;38:329–42.
- [71] Keil LC, Evans JW. Bone growth and composition in weanling and mature rats exposed to chronic centrifugation. *The Physiologist* 1979;22:S53–4.
- [72] Heinonen A, Sievänen H, Kannus P, Oja P, Vuori I. Effects of unilateral strength training and detraining on bone mineral mass and estimated mechanical characteristics of the upper limb bones in young women. *J Bone Miner Res* 1996;11:490–501. doi:10.1002/jbmr.5650110410.
- [73] Lanyon LE, Rubin CT. Static vs dynamic loads as an influence on bone remodelling. *J Biomech* 1984;17:897–905.
- [74] Qin YX, Rubin CT, McLeod KJ. Nonlinear dependence of loading intensity and cycle number in the maintenance of bone mass and morphology. *J Orthop Res* 1998;16:482–9. doi:10.1002/jor.1100160414.
- [75] Ozcivici E, Luu YK, Adler B, Qin Y-X, Rubin J, Judex S, et al. Mechanical signals as anabolic agents in bone. *Nat Rev Rheumatol* 2010;6:50–9. doi:10.1038/nrrheum.2009.239.
- [76] Rubin C, Turner AS, Bain S, Mallinckrodt C, McLeod K. Anabolism. Low mechanical signals strengthen long bones. *Nature* 2001;412:603–4. doi:10.1038/35088122.
- [77] Prisby RD, Lafage-Proust M-H, Malaval L, Belli A, Vico L. Effects of whole body vibration on the skeleton and other organ systems in man and animal models: What we know and what we need to know. *Ageing Res Rev* 2008;7:319–29. doi:10.1016/j.arr.2008.07.004.

- [78] Sen B, Xie Z, Case N, Styner M, Rubin CT, Rubin J. Mechanical signal influence on mesenchymal stem cell fate is enhanced by incorporation of refractory periods into the loading regimen. *J Biomech* 2011;44:593–9. doi:10.1016/j.jbiomech.2010.11.022.
- [79] Brouwers JEM, van Rietbergen B, Ito K, Huiskes R. Effects of vibration treatment on tibial bone of ovariectomized rats analyzed by in vivo micro-CT. *J Orthop Res* 2010;28:62–9. doi:10.1002/jor.20951.
- [80] van der Jagt OP, van der Linden JC, Waarsing JH, Verhaar JAN, Weinans H. Low-magnitude whole body vibration does not affect bone mass but does affect weight in ovariectomized rats. *J Bone Miner Metab* 2012;30:40–6. doi:10.1007/s00774-011-0293-5.
- [81] Slatkowska L, Alibhai SMH, Beyene J, Hu H, Demaras A, Cheung AM. Effect of 12 months of whole-body vibration therapy on bone density and structure in postmenopausal women: a randomized trial. *Ann Intern Med* 2011;155:668–79, W205. doi:10.7326/0003-4819-155-10-201111150-00005.
- [82] Flieger J, Karachalios T, Khaldi L, Raptou P, Lyritis G. Mechanical stimulation in the form of vibration prevents postmenopausal bone loss in ovariectomized rats. *Calcif Tissue Int* 1998;63:510–4.
- [83] Rubinacci A, Marenzana M, Cavani F, Colasante F, Villa I, Willnecker J, et al. Ovariectomy sensitizes rat cortical bone to whole-body vibration. *Calcif Tissue Int* 2008;82:316–26. doi:10.1007/s00223-008-9115-8.
- [84] Bojados M, Jamon M. The long-term consequences of the exposure to increasing gravity levels on the muscular, vestibular and cognitive functions in adult mice. *Behav Brain Res* 2014;264:64–73. doi:10.1016/j.bbr.2014.01.018.
- [85] Guéguinou N, Bojados M, Jamon M, Derradji H, Baatout S, Tschirhart E, et al. Stress response and humoral immune system alterations related to chronic hypergravity in mice. *Psychoneuroendocrinology* 2012;37:137–47. doi:10.1016/j.psyneuen.2011.05.015.
- [86] Pasqualini M, Lavet C, Elbadaoui M, Vanden-Bossche A, Laroche N, Gnyubkin V, et al. Skeletal site-specific effects of whole body vibration in mature rats: from deleterious to beneficial frequency-dependent effects. *Bone* 2013;55:69–77. doi:10.1016/j.bone.2013.03.013.
- [87] Chung K, Wallace J, Kim S-Y, Kalyanasundaram S, Andalman AS, Davidson TJ, et al. Structural and molecular interrogation of intact biological systems. *Nature* 2013;497:332–7. doi:10.1038/nature12107.
- [88] Kotelnikov G.P. SAG. Influence of gravitational therapy on reparative osteogenesis in patients with osteomyelitis of lower extremities. *Saratov J Med Sci Res* 2010; 6: 695-700.
- [89] Tomer R, Ye L, Hsueh B, Deisseroth K. Advanced CLARITY for rapid and high-resolution imaging of intact tissues. *Nat Protoc* 2014;9:1682–97. doi:10.1038/nprot.2014.123.

- [90] Epp JR, Niibori Y, Hsiang H-L (Liz), Mercaldo V, Deisseroth K, Josselyn SA, et al. Optimization of CLARITY for Clearing Whole-Brain and Other Intact Organs. *Eneuro* 2015;2:ENEURO.0022–15.2015. doi:10.1523/ENEURO.0022-15.2015.
- [91] Single-Cell Phenotyping within Transparent Intact Tissue through Whole-Body Clearing: *Cell* n.d. [http://www.cell.com/abstract/S0092-8674\(14\)00931-3](http://www.cell.com/abstract/S0092-8674(14)00931-3) (accessed July 7, 2015).

Annexes

Technical data

Fluorescent immunohistochemistry protocol for double staining: 3 days sequential protocol

See General protocol of fluorescent IHC from the “Osteocyte protein expression in mouse and human biopsies: optimized methods for detection and quantification” chapter.

Second protein detection

After the incubation with Streptavidin-Alexa Fluor (Life technologies, S 11225) solution samples were washed with TBS – 10 min at room T° on a shaker, then proceeded for the blocking step, and incubated overnight with the second primary antibody at 4° as it was described in the general protocol. After, samples were washed with TBS – 10 min at room T° on a shaker. The subsequent procedures were done according to manufactures protocol of the PowerFluor 488 immunofluorescence rabbit detection kit (Maxvision, PF-21M) or the PowerFluor 594 immunofluorescence mouse detection kit (Maxvision, PF 13S). Samples were stained with Dapi as it described above, and mounted with MaxGlow.

Immunohistochemistry protocol for the enzymatic detection

See General protocol of fluorescent IHC from the “Osteocyte protein expression in mouse and human biopsies: optimized methods for detection and quantification” chapter.

Steps specific for enzymatic detection:

Endogenous peroxidases blocking

After rehydration step, sections were incubated for 30 min at room T° in a bath of peroxidase blocking solution (for 100ml: 60ml of TBS, 40ml of Methanol, and 3.3ml of 30% H₂O₂), protected from light. After, the sections were washed in a bath of TBS for 5 min at room T° on a shaker.

Signal amplification

Samples were incubated either with 1:200 Streptavidin HRP conjugated (Dako,P0397) in BSA/TTBS in the humid chamber for 30 min at 37°. After incubations samples were washed in TBS – 5 min at room T° on a shaker.

Detection

Samples were incubated with NovaRed peroxidase substrate solution (Vector, SK-4800), prepared according to manufactures protocol for 5 min at room T°. After 5 min samples were rinsed, and then washed with demineralized H₂O – 5 min at room T° on a shaker.

Notes: in each particular case optimal duration of staining development, and therefore staining intensity, can be controlled visually with light microscope.

Counter staining

Samples were counterstained with Hematoxylin (1/4 in H₂O) for 30 sec at room T° and then washed with H₂O, 5 changes – 2 min each at room T° on a shaker.

Mounting

NovaRed detection requires organic mounting medium. Thus, samples were gradually dehydrated with 40% Ethanol, 70%, 90%, 100% (two changes), and Xylene (three changes) – 30 sec in each. After removal of residual Xylene, sections were permanently mounted with VectaMount (Vector, Y1016).

Immunohistochemistry protocol for the enzymatic detection: double staining, 3 days sequential protocol

General protocol of IHC was used with some adjustments:

Signal amplification: first protein

Samples were incubated for 30 min at room T° in the humid chamber with ready-to-use Streptavidin Alkaline Phosphatase conjugated solution (Abcam, ab 64268). After incubations samples were washed in TBS – 5 min at room T° on a shaker.

Detection: first protein

Samples were incubated with Vector Blue alkaline phosphatase substrate solution (Vector, SK-4800), prepared according to manufactures protocol for 5 min at room T°. One drop of Levamisole solution (Vector, SP-5000) was added to the substrate buffer to block endogenous alkaline phosphatase. After 4 min of incubation samples were rinsed and then washed with TBS – 10 min at room T° on a shaker.

Notes: in each particular case optimal duration of staining development, and therefore staining intensity, can be controlled visually with light microscope.

Detection: second protein

After the first protein detection samples were processed for the blocking step, and incubated overnight with the second primary antibody at 4° as it was described in the general protocol. After, samples were washed with TBS – 10 min at room T° on a shaker. The subsequent procedures were done according to manufactures protocol of the Expose rabbit-specific HRP/AEC detection kit (Abcam, ab94361). Samples were counterstained with Hematoxylin as it described above, and mounted with aqueous mounting medium (Abcam, ab 128982).

Notes: no TTBS was used at these steps to protect the first staining from possible washing out.

Protocol of 3D immunohistochemistry adapted from Clarity technique

Preparation of Hydrogel solution for intracardiac perfusion:

For 200ml:

- Acrylamide 30% (AppliChem A3651) 26.65ml
- Bis Acrylamide 2% (AppliChem A3657) 5ml
- Persulfate Ammonium (Bio-Rad 161-0700) dissolved 0.1g in 1ml dH₂O and take 0.25ml.

- N,N,N',N'-Tetramethylethylenediamine TEMED (VWR, 95029-576) 0.025ml
- 10x PBS (Sigma P3813-10PAK) 20ml
- dH₂O 66.15ml
- 10% NBF 80ml

Keep at 4°

Intracardiac perfusion:

First, perfuse with 20ml 1x PBS

Then perfuse with 40ml ice-cold hydrogel solution

Quickly harvest samples and put them at 4° for 3 days. Slightly shake tubes with samples twice a day to avoid polymerization around samples.

Expose to vacuum every day for 25-30 min on ice.

Embedding:

After 3 days add 0.1ml Persulfate Ammonium (Bio-Rad 161-0700) and 0.01 TEMED and keep in vacuum at room t° until polymerization. Then put at 37° for 3h for complete polymerization.

Cutting:

Cut 50-100µm thick transversal section of cortical bone.

Decalcification:

Gently remove gel around samples, and put in Immunocal solution for 24h at 4°, shake samples twice a day.

Cleaning solution preparation:

For 100ml (Enough for rinsing and filling one large Petri Dish)

Sodium Dodecyl Sulfate 4g for 4%

dH₂O 50ml

Boric Acid 1.24g for 200mM

NaOH 1N to pH 8.5

dH₂O to 100ml

Can be stored at 4°, white precipitation is normal and dissolves at room t°.

Samples cleaning:

Put samples in a large Petri Dish, fill with cleaning solution and leave on shaker at 38° for 4 weeks. Change the solution once a week.

After cleaning, wash samples with TPBS (0.1% Tween 20 in PBS) for 3 days. Change TPBS every day.

Cleaned samples can be stored at 4°.

Immunolabeling:

Put samples in 1.5ml Eppendorf tube in 1ry a/b solution (Goat anti mouse, R&D Systems, AF1589), dilution 1/200 in BSA/TPBS for 1 day at 37° on the shaker.

Wash in TPBS for 1 day at 37° on the shaker.

Put samples in 1.5ml Eppendorf tube in 2ry a/b solution (Rabbit-a-Goat IgG, Dako, E0466), dilution 1/600 in BSA/TPBS for 1 day at 37° on the shaker.

Wash in TPBS for 1 day at 37° on the shaker.

Put in Streptavidin-Alexa Fluor (Life technologies, S 11225), 1/400 overnight at room t° on the shaker. Avoid light!

Wash in PBS for 5 hours at 37° on the shaker. Avoid light!

Put in 1/100 DAPI solution for 1 hour at 37° on the shaker. Avoid light!

Imaging:

Avoid light! Put stained bone samples in 70% solution of polypropylene glycol in water for 2 hours prior to imaging. Samples may become opaque after 24 hours, thus imaging must be done rapidly.

Supplementary videos

Video 1. 3D reconstruction of a Z-stack of images of mouse femoral cortex immunolabeled for Sclerostin; Lacunar-canalicular network and blood vessel; oil immersed objective; x1000; 10µm thickness. Deconvoluted video.

Video 2. Video of a Z-stack of raw images stack of mouse femoral cortex immunolabeled for Sclerostin; Lacunar-canalicular network and bifurcating blood vessel; oil immersed objective; x630; 45µm thickness. Non-deconvoluted video. Focus starts from the tissue surface and follows a blood vessel (in the middle) which bifurcates. Step between images is 0.1µm. Many connections of Sclerostin positive canaliculae with the blood vessel are observable. Gray background is due to collagen autofluorescence.

Papers published/submitted

Paper #1: “Effects of chronic hypergravity: from adaptive to deleterious responses in growing mouse skeleton” – submitted to the Journal of Applied Physiology, in the process of 3rd revision.

Paper #2: “High-acceleration Whole Body Vibration stimulates cortical bone accrual and increases bone mineral content in growing mice” – submitted to the Journal of Biomechanics, in the process of 1st revision.

Paper #3: “Osteocyte protein expression in mouse and human biopsies: optimized methods for detection and quantification” – is going to be submitted to the BoneKEy Reports.

Author’s CV

Formation

King's College London, GB

Oct 2010 – Oct 2011

Master Science: **Physiologie spatiale et santé**

- Bourse “Innovation”
- Etudes terminées avec la plus haute qualification et avec mention

Modules du Programme:

- Physiologie cardiovasculaire et respiratoire depuis le repos jusqu’à l’exercice exhaustif
- Physiologie humaine aérospatiale
- Projet de librairie personnelle de la physiologie spatiale et sante
- Physiologie des muscles et exercice
- Projet de recherche personnelle de la physiologie spatiale et santé
- Physiologie spatiale et santé:
 - Les effets physiologiques de l’environnement spatial sur les humains et les méthodes employées pour les atténuer
 - L’influence de l’environnement spatial sur le comportement et la performance de l’humain
 - Les méthodes d’expérimentation appropriées pour investiguer les effets physiologiques de l’environnement spatial, calibrage, acquisition des données et analyse des résultats avec les méthodes statistiques appropriées

Saint-Pétersbourg Académie de la chimie et la pharmacie, Russie *Sep 1998 - Juin 2004*

Master Science: **Pharmacie**

- Etude financée par une bourse

- Validation avec la plus haute qualification des modules suivants: pathophysiologie, chimie analytique, chimie biologique, pharmacologie, pharmacologie clinique, chimie organique et autre

La formation a donné l'expérience dans:

- Travail dans le milieu de laboratoire, préparation des réactifs, synthèse de la produits chimiques, travail avec produits toxiques et concentrés
- Analyses qualitatives et quantitatives par des méthodes chimiques et physicochimiques, comme le titrage, chromatographie gazeuse, chromatographie sur couche mince, spectrophotométrie, photolorimétrie et spectroscopie
- Approche multidisciplinaire d'étude du corps humain d'un point de vue biochimique, physiologique et pharmacologique

Expérience professionnelle

Laboratoire de Biologie du Tissu Osseux, INSERM U1059, *Oct 2011 – Sep 2015*

Université Jean Monnet, France

En collaboration avec **Leiden University Medical Centre,** Hollande

Doctorant en Biologie "Les effets de l'hypergravité sur le squelette des souris"

But: Compréhension des mécanismes de réaction du tissu osseux à la micro et hypergravité, pour le développement des contremesures efficaces contre la perte osseuse pendant les vols spatiaux

- Recherche sur l'impact de l'hypergravité continue (21 jours de centrifugation à 2G et 3G) et intermittente (vibration du corps entier) sur le tissu osseux
- Mission BION-M1 eu 2013 pour étudier les mécanismes de réponse des os à la microgravité

State Mariinski Hôpital, Département de Traumatologie et d'Orthopédie

Volontaire, *Juin 2009 – Juin 2010*

- Aide et assistance aux infirmières avec leurs patients
- Présence aux opérations de chirurgie d'ostéosynthèse et aux réunions sur les cas cliniques

3M, Département dentaire

Représentant médical senior, *Aout 2009 – Juin 2010*

- Conseils aux dentistes sur l'utilisation des produits 3M

Medtronic, Département d'Arythmie

Manager de développement, *Mai 2007 – Juin 2009*

- Formation et conseils aux cardiologues sur les méthodes d'utilisation des générateurs d'impulsion et des défibrillateurs implantables

F. Hoffmann la Roche, Département de Transplantologie and Virologie

Key account manager, *Mai 2006 – Mai 2007*

- Conseils aux transplantologues et oncologues sur les nouvelles méthodes de traitement développés par la compagnie

Abbott Lab

Représentant médical, *Sep 2004 – Mai 2006*

- Conseils aux médecins généralistes et gastroentérologues sur les nouvelles méthodes de traitement développés par la compagnie

Compétences techniques

- Techniques de coloration pour l'évaluation histologiques des échantillons d'os
- Analyses quantitative de l'activité des cellules osseuses
- Analyse des paramètres de la masse structurelle avec μ CT
- Analyse de la vascularisation des os
- Immunohistochimie qualitative et quantitative
- Analyse RT qPCR

Affiliations Professionnelles

- Membre de l'Association Biomédicale Spatiale de GB
- Membre de l'American Society for Bone and Mineral Research

Récompenses

- Young researcher award, "The life in space for life on Earth" ISGP symposium, Aberdeen, 18-22 Juin 2012

Publications

- Skeletal site-specific effects of whole body vibration in mature rats: from deleterious to beneficial frequency-dependent effects. Pasqualini M et al, Bone, 55(1):69-77,2013.

- Structure of the cortical cytoskeleton in fibres of postural muscles and cardiomyocytes of mice after 30-day 2g-centrifugation. Ogneva I.V., Gnyubkin V. et al, Journal of Applied Physiology, Dec 24:jap.00812.2014
- Book chapter Hindlimb unloading, Casting in Generate On Earth An Extra-Terrestrial Environment, River Publisher. Is currently pending publishing (http://www.riverpublishers.com/view_details.php?book_id=288).

Book chapter “Animals: Unloading, casting”

Animals: Unloading, Casting

Vasily Gnyubkin and Laurence Vico

INSERM U1059, LBTO, Faculty of Medicine, University of Lyon,
Saint-Etienne, France

12.1 Introduction

The aim of this section is to provide description of techniques of on-ground microgravity simulation based on animal models such as hindlimb unloading, casting, and denervation. It is well known that exposure to microgravity leads to notable restrictions in general movement and mechanical loading in astronauts. Conditions of spaceflight together with spacecraft environment, confinement, altered diet and altered ambient atmosphere, and relatively high radiation result in significant alterations in normal physiological processes. Existing countermeasures, based on physical exercises, are not able to completely substitute normal Earth gravity loading. It is undoubtedly true that the development of new countermeasures is a crucial step on a way to the long-term space missions. One of the problems with spaceflight experiments is that opportunities to carry them out are expensive and rare. That is where animal ground-based models come into play. With ground-based models, there are no limitations related to number of animals. What is also important is that there is no ideal imitation of all conditions of long-term spaceflight. Even techniques such as head-down-tilt bed-rest studies and water immersion which are generally accepted as the gold standard imitate only some of the spaceflight conditions. At the same time, parabolic flights and drop towers provide weightlessness, but only for very short periods of time. In the past, varieties of mammalian species, including monkeys, dogs, and rabbits, were used for research purposes. Nowadays, rodents have become one of the most used animals in all areas of scientific studies. There are many reasons in favor of using them instead of primates or rabbits: mice and rats grow fast and reproduce quickly, and it is easy to house and maintain them. Also, with rats and especially mice, it is possible to conduct uniform studies with genetically identical animals. As it is easier for the mice to be genetically modified, it is also easier to breed either transgenic or knockout animals.

In order to develop an acceptable ground-based model for the simulation and study of spaceflight aspects, NASA-Ames Research Center has formulated the following requirements: experimental animals should demonstrate physiological response similar to that during spaceflight; the model should provide thoraco-cephalic fluid shift; the model should unload limbs without motion restriction or paralysis, and provide ability to recover; and the model should not be stressful for animals. Such technique would be valuable for predicting the effects of spaceflight, studying possible mechanisms of these effects, and developing countermeasures [1].

Nowadays, different immobilization techniques are widely used for the simulation of mechanical unloading. Immobilization itself can be combined with dietary or pharmaceutical intervention. Generally, methods can be merged into two groups: conservative (bandaging, casting, hindlimb unloading, and confinement) and surgical (nerve resection, denervation with botulin toxin, spinal cord resection, and tendon resection). Immobilization provided by casting, denervation, and tendon resection is widely used for the quick development of disuse osteopenia or muscle atrophy. Therefore, these models are useful for studying different countermeasures against bone or muscle loss. However, this approach has serious limitations: surgical intervention or casting does not mimic effects of spaceflight on cardiovascular system, nervous system, and immune system. In addition, with the existing surgical models, recovery from disuse is impossible or difficult. Such surgical models may also result in inflammation, altered trophic, perfusion, and innervation of immobilized limb [2]. Among microgravity simulation models, hindlimb unloading fits most of the NASA requirements. It induces muscle atrophy and alterations in bone structure similar to physiological consequences observed in humans after spaceflight or bed rest. Other physiological changes similar to spaceflight such as synaptic plasticity changes [3] and immune system suppression have also been reported in this model [4]. In cardiovascular functions, rodent headdown-tilt simulates cephalic fluid redistribution and hypovolemia. It also leads to vessel's structural and functional adaptations and alters baroreflex function [5]. Putting all these factors together, it is clear why the use of tail traction in the hindlimb unloading model has become the technique of choice for studying spaceflight-like changes in rats and mice.

12.2 Hindlimb Unloading Methodology

Emily R. Morey-Holton has done significant work on the development and standardization of hindlimb unloading. The review of technical aspects of the method produced in 2002 has been widely used as a base for microgravity simulation studies [2]. Here we provide the description of the method based on this review. Before the experiment, animals are

acclimated to their cages for at least two days prior to the hindlimb unloading. First, a strip of traction tape, pre-attached to the plastic tab, is attached to the pre-cleaned tail just above the hair line. Then, the traction tape is fixed by two strips of filament tape placed around the base of the tail and on about half-way up the traction tape. To protect the traction tape, gauze bandage can be wrapped around the tail. The gauze bandage should not cover the whole tail, because the tail plays an important role in thermoregulation. Daily health checks confirmed that the exposed tip of the tail remained pink, indicating adequate blood flow [6]. The animal is then attached to the top of the cage. Such way of harnessing aims to distribute the load along the length of the tail and avoid excessive tension on a small area. The body of the animal makes about a 30° angle with the floor of a cage, and thus the animal does not touch the grid floor with its back feet (Figure 12.1).

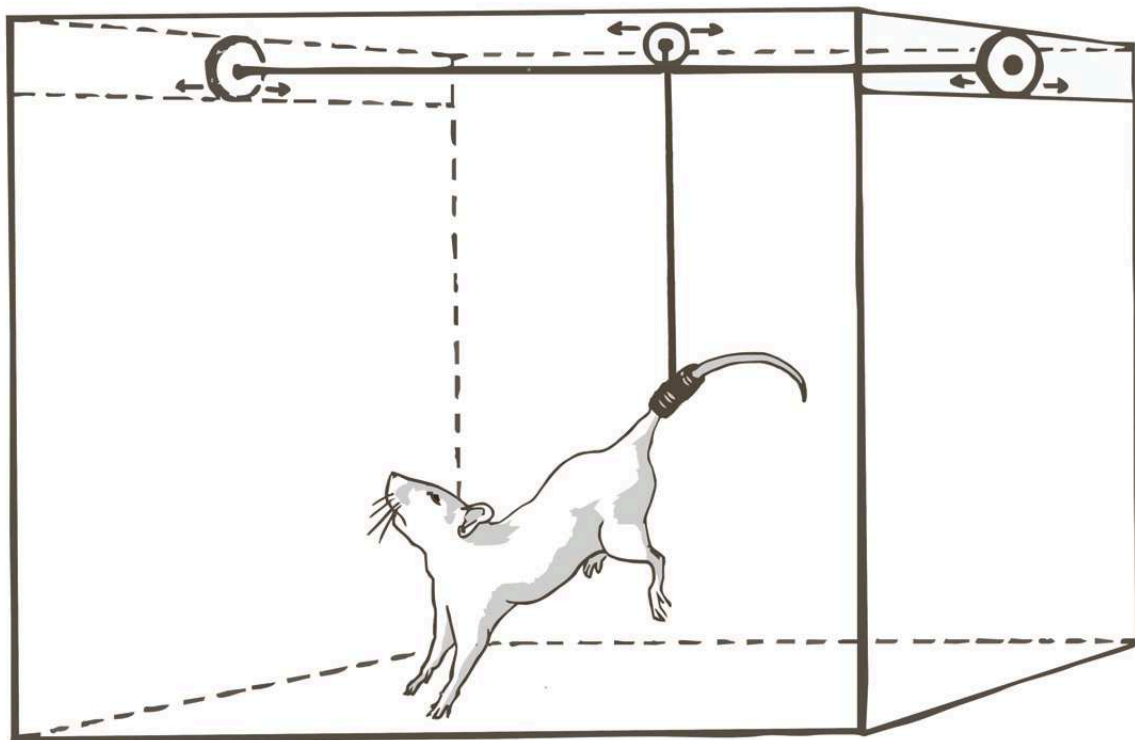


Figure 12.1 Hindlimb unloading model.

At this position, 50% of rat's body weight applies to its forelimbs. A 30° angle of unloading is recommended because it provides normal weight bearing on the forelimbs, unloads the lumbar vertebrae but not the cervical vertebrae, and induces a cephalic fluid shift [2]. The angle and height of the animals are checked, and then adjusted if necessary, on a daily basis. In order to use the system on animals with different behavioral pattern and smaller size of the body, such as mice, some adjustments to the hindlimb unloading system are needed. These include the use of smaller cages, and inclusion of a device to prevent mice from climbing the harness and chewing it. As the mice are generally weaker than rats and have smaller body

weight in relation to the total weight of the unloading system, they find it difficult to freely move around the cage and have access to food and water. Therefore, a significant adjustment to the friction is needed between the roller and the wire. There are some disadvantages of the method: tail examination can be difficult due to the size of gauze bandage; animals can chew the traction tape and release themselves; and tail can undergo inflammation or necrosis [7]. Therefore, in the literature, several modified techniques are suggested to harness fixation based on minimally invasive surgery. As one of the methods, the authors have made a harness for hindlimb unloading by inserting a surgical steel wire through intervertebral disc space of the tail. After that, the wire was ring shaped and used for suspension. Detailed step-by-step video description is publicly available on the Internet [7]. Similar method was proposed for long-term studies on adult rats. Continuous hindlimb unloading for longer than 3 weeks can be complicated in rats with high body weight (350 g or more). Animals come down from suspension because of sloughing of tail skin. Even very short periods of reloading induce changes in muscle physiology. Therefore, frequent release of animals from suspension apparatus can compromise a study [8]. In such case, after passing a steel cable through rat's tail skin and wrapping it loosely with gauze, authors used a 5-ml syringe cut in half longitudinally together with orthopedic casting to provide strong structural integrity. This was performed to ensure that the tail remained in a straight line with respect to the body once the animal was hindlimb suspended [8].

These methods are principally close to the "classical" tail suspension. Interestingly, there is a new method that uses a different unloading model. Partial weight suspension was described in Erica B. Wagner's paper in 2010 [9]. The main difference is that this system allows the distribution of gravitation loading among hindlimbs and forelimbs in a desired proportion between 10 and 80% of total weight bearing, with an accuracy of $\pm 5\%$.

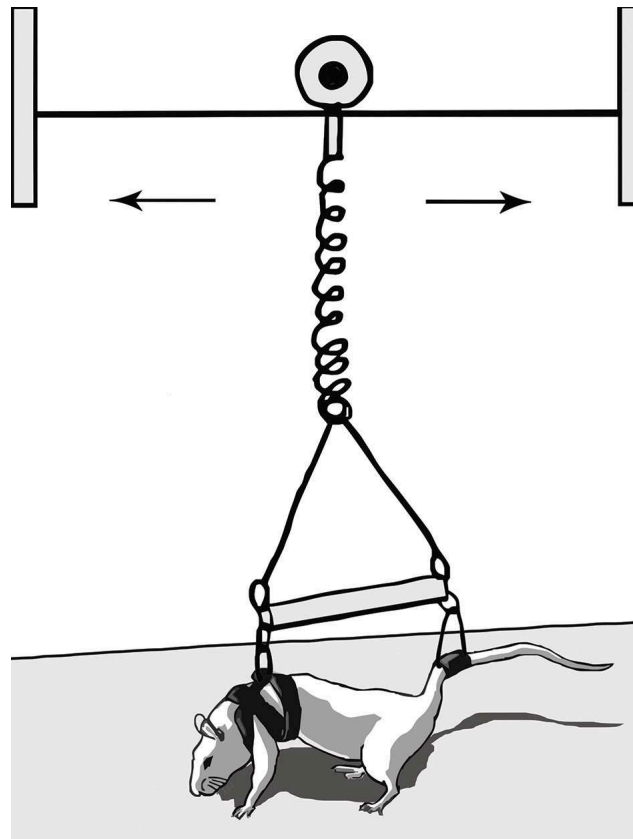


Figure 12.2 Partial weight suspension model.

With such a technique, animals have linear freedom of motions; feeding and cleaning are easy; and animals can be exposed to quadrupedal unloading for at least three weeks Figure 12.2. Also, this system allows for a full recovery of animals after an experiment [9]. To fix an animal in the desired position, two harnesses are used. One is a ring of bandage put around the tail's base. The second one is a flexible, breathable "jacket" secured around the chest cage. The tail's and the chest's harnesses are connected to adjustable chains and hollow metal rod. With this model, researchers performed a fascinating study where they imitated gravitational conditions of Mars planet [9]. Possible disadvantages of this model of microgravity simulation include an absence of head-down-tilt and physiological changes related to it.

12.3 Recommendations for Conducting Hindlimb

Unloading Study

While conducting the research on animal models, it is important to remember that any interference of normal life activity is a stress for animals. Hindlimb unloading, restraint stress, and social isolation cause significant perturbations in blood pressure, heart rate levels, [5] and plasma corticosterone level [10]. Therefore, it is recommended to use minimal restraints and avoid unnecessary manipulations during preparatory period and period of tail

suspension. Physiological and environmental parameters, including body weight, room temperature, and angle of unloading, should be monitored on a daily basis [11]. Animals from a control group should be kept in identical cages. Behavioral or physiological modifications produced by environmental variables can cause false results or give wrong hypothesis [11]. Another important factor related to control group is feeding. Unloaded animals lose weight during the experiment despite easy access to food and water because of the alterations in energy balance. The difference in weight between experimental and control groups, both fed ad libitum, can be from 5 to 20% in adult rats [2]. Hence, it is recommended to either feed control group with average amount of food consumed by suspended group or reduce caloric intake for control group. However, the latter can result in physiological and behavioral alterations [2]. Although some authors argue that forelimbs can be used as an internal control [2], we would advise considering possible systemic effects of hindlimb unloading and being careful when applying it. It is also relevant to other immobilization techniques where one of the limbs remains “unaffected” and could be used as an internal control.

12.4 Casting, Bandaging, and Denervation

Different surgical techniques such as nerve or tendon ectomies have been used in the past for the reproduction of microgravity effects by induction of localized extremities disuse. For instance, commonly used sciatic neurectomy is a visually confirmed resection of 3–4 mm of sciatic nerve that leads to efficient denervation of all regions of the hindlimb [12]. These techniques lead to not only irreversible immobilization and significant bone loss and muscle atrophy but also multiple side effects. Non-invasive methods such as casting, bandaging, and injection of *Clostridium botulinum* toxin have become more popular in the recent years.

Clostridium botulinum toxin type A is a bacterial metalloprotease causing muscle paralysis and therefore limb disuse by the inhibition of neurotransmitter release. The injection is done into the posterior lower limb musculature. The major advantage of this technique compared to neurectomy is non-invasiveness and possibility of complete recovery within several months [13].

Bandaging and casting are methods of immobilization based on fixation of extremities in constant position by applying either elastic tape (bandaging) or hard orthopedic plaster (casting). During bandaging procedure, a hindlimb of anesthetized animal is immobilized against the abdomen with few layers of elastic bandages. Ankle joints and the knee are placed in extension, and the hip joint is placed in flexion [14]. The immobilized limb should not touch the floor of the cage during animal’s movement. The gravitational loading, normally

distributed between both hindlimbs, rests on the free limb. Animals are free to move and can easily reach food and water. The bandage should be examined daily and replaced twice a week [14]. Casting is very similar to bandaging but it allows fixing animal's extremities in desirable positions with precise adjustment of joint angles and muscling straitening. This feature of casting techniques allows to get either plantarflexion or dorsiflexion cast immobilization. Dorsiflexion of the ankle joint at an angle of 35° by casting of a limb was used by Nemirovskaya [15] in her study of adaptation mechanisms to microgravity in combination with tail suspension model. Casting can be not only unilateral but also bilateral. This model was recommended as a reliable cast immobilization particularly for mice because small size of animals is a technical challenge [16]. Casting is performed on anesthetized animals. The cast covers both hindlimbs and the caudal fourth of the body. A thin layer of padding is recommended to be placed underneath the cast to prevent abrasions. To minimize freedom of movement of limbs, slight pressure should be applied when wrapping the casting tape. To resist the cast against chewing on, fiberglass material can be applied over the cast. The animals can move using their forelimbs to reach food and water. The mice should be monitored daily for abrasions, chewed plaster, venous occlusion, and problems with ambulation [16].

12.5 Conclusions

Nowadays, hindlimb unloading is the only technique which imitates more physiological alterations relevant to spaceflight than any other on-ground model. Social isolation is not a common case for experiments conducted in space but it is a significant source of stress for animals subjected to unloading. This aspect should be taken into account when comparing results from spaceflights to results from on-ground models. Future development of hindlimb unloading could help tackle this issue.

References

- [1] Morey-Holton, Emily R. and Ruth K. Globus. "Hindlimb Unloading of Growing Rats: A Model for Predicting Skeletal Changes During Space Flight." *Bone* 22, no. 5 (1998): 83–88.
- [2] Morey-Holton, Emily R. and Ruth K. Globus. "Hindlimb Unloading Rodent Model: Technical Aspects." *Journal of Applied Physiology* 92, no. 4 (2002): 1367–1377.
- [3] Dupont, Erwan, Laurence Stevens, Laetitia Cochon, Maurice Falempin, Bruno Bastide, and Marie-Helene Canu. "ERK is Involved in the Reorganization of Somatosensory Cortical Maps in Adult Rats Submitted to Hindlimb Unloading." *PLoS ONE* 6, no. 3 (2011): e17564.

- [4] Aviles, Hernan, Tesfaye Belay, Monique Vance and Gerald Sonnenfeld. "Effects of Space Flight Conditions on the Function of the Immune System and Catecholamine Production Simulated in a Rodent Model of Hindlimb Unloading." *Neuroimmunomodulation* 12 (2005): 173–181.
- [5] Tsvirkun, Darya, Jennifer Bourreau, Aurélie Mieuset, Florian Garo, Olga Vinogradova, Irina Larina, Nastassia Navasiolava, Guillemette Gauquelin-Koch, Claude Gharib and Marc-Antoine Custaud. "Contribution of Social Isolation, Restraint, and Hindlimb Unloading to Changes in Hemodynamic Parameters and Motion Activity in Rats." *PLoS ONE* 7, no. 7 (2012): e39923.
- [6] Riley, Danny A., Glenn R. Slocum, James L. Bain, Frank R. Sedlak and James W. Mellender. "Rat Hindlimb Unloading: Soleus Histochemistry, Ultrastructure, and Electromyography." *Journal of Applied Physiology* 69 (1990): 58–66.
- [7] Ferreira, Andries J., Jacqueline M. Crissey and Marybeth Brown. "An Alternant Method to the Traditional Nasa Hindlimb Unloading Model in Mice." *Journal of Visualized Experiments* no. 49 (2011): e2467.
- [8] Knox, Micheal, James D. Fluckey, Patrick Bennett, Charlotte A. Peterson and Esther E. Dupont-Versteegden. "Hindlimb Unloading in Adult Rats Using an Alternative Tail Harness Design." *Aviation, Space, and Environmental Medicine* 75, no. 8 (2004): 692–696.
- [9] Wagner, Erika B., Nicholas P. Granzella, Hiroaki Saito, Dava J. Newman, Laurence R. Young and Mary L. Boussein. "Partial Weight Suspension: A Novel Murine Model for Investigating Adaptation to Reduced Musculoskeletal Loading." *Journal of Applied Physiology* 109, no. 2 (2010): 350–357.
- [10] Halloran, Bernard P., Daniel D. Bikle, Charlotte M. Cone, Emily Morey-Holton. "Glucocorticoids and Inhibition of Bone Formation Induced by Skeletal Unloading." *American Journal of Physiology Endocrinology and Metabolism* 255 (1988): 875–879.
- [11] Blottner, Dieter, Najet Serradj, Michele Salanova, Chadi Touma, Rupert Palme, Mitchell Silva, Jean Marie Aerts, Daniel Berckmans, Laurence Vico, Yi Liu, Alessandra Giuliani, Franco Rustichelli, Ranieri Cancedda and Marc Jamon. "Morphological, Physiological and Behavioural Evaluation of a 'Mice in Space' Housing System." *Journal of Comparative Physiology* 179, no. 4 (2009): 519–533.
- [12] Kodama, Yoshiaki, Peter Dimai, John E. Wergedal, Matilda Sheng, Rashmi Malpe, Stepan Kutilek, Wesley Beamer, Leah R. Donahue, Clifford J. Rosen, David J. Baylink and John R. Farley. "Cortical Tibial Bone Volume in Two Strains of Mice: Effects of Sciatic

Neurectomy and Genetic Regulation of Bone Response to Mechanical Loading.” *Bone* 25, no. 2 (1999): 183–190.

[13] Manske, Sarah L., Steven K. Boyd and Ronald F. Zernicke. “Muscle and Bone Follow Similar Temporal Patterns of Recovery from Muscle-Induced Disuse Due to Botulinum Toxin Injection. *Bone* 1, no. 46 (2010): 24–31.

[14] Ma, Yanfei, Webster S.S. Jee, Zhongzhi Yuan., Wei Wei, Hongka Chen, Sunwah Pun, Haohai Liang and Chaohua Lin. “Parathyroid Hormone and Mechanical Usage have a Synergistic Effect in Rat Tibial Diaphyseal Cortical Bone.” *Journal of Bone and Mineral Research* 14 (1999):439–448.

[15] Nemirovskaya, Tatiana L., Boris S. Shenkman, Anna Muchina, Yaroslav Volodkovich, Maria Sayapina, Olesya Larina and Elena Bratcseva. “Role of Afferent Control in Maintaining Structural and Metabolic Characteristics of Stretched Soleus in Rats Exposed to Hindlimb Suspension.” *Journal of Gravitational Physiology* 9, no. 1 (2002): 121–122.

[16] Frimel, Tiffany N., Kapadia Fatema, Gabriel S. Gaidosh, Ye Li, Glenn A. Walter and Krista Vandenborne. “A Model of Muscle Atrophy Using Cast Immobilization in Mice.” *Muscle Nerve* 32 (2005): 672–674.